Advanced Control of Active Distribution Networks Integrating Dispersed Energy Storage Systems

THÈSE N^O 7070 (2016)

PRÉSENTÉE LE 11 NOVEMBRE 2016
À LA FACULTÉ DES SCIENCES ET TECHNIQUES DE L'INGÉNIEUR
GROUPE DE SCIENTIFIQUES STI
PROGRAMME DOCTORAL EN ENERGIE

ÉCOLE POLYTECHNIQUE FÉDÉRALE DE LAUSANNE

POUR L'OBTENTION DU GRADE DE DOCTEUR ÈS SCIENCES

PAR

Maryam BAHRAMIPANAH

acceptée sur proposition du jury:

Dr J. Van Herle, président du jury
Dr S.-R. Cherkaoui, Prof. M. Paolone, directeurs de thèse
Prof. C. A. Nucci, rapporteur
Dr A. oudalov, rapporteur
Prof. D. Dujic, rapporteur

EPFL

ÉCOLE POLYTECHNIQUE
FÉDÉRALE DE LAUSANNE

Suisse
2016

To Fatemeh & Ata, my beloved parents,

For their unconditional love and support.

To Zagros, my lovely husband,

For his unending love and sacrifices.

To Mohsen, my dear brother,

Who always besides me.

To you, as a reader….

Acknowledgements

This work would not have been completed without the help and support of many kind people around me, to only some of whom it is possible to give particular mention here.

First and foremost, I would like to express my deepest gratitude to my thesis directors, Dr. Rachid Cherkaoui and Prof. Mario Paolone for giving me the opportunity to pursue my PhD thesis under their supervision. *Rachid*, *Mario*, your deep knowledge, kindness, invaluable guidance, and unwavering support made my PhD period a wonderful experience. You were giving me the liberty to take decisions during my research project while guiding me into right directions. You were way more than simple supervisors, and I am extremely blessed to work with you during the past few years.

I would also like to express my gratitude to the jury members, Prof. Carlo Alberto Nucci, Dr. Alexandre Oudalov, Prof. Drazen Dujic, and Prof. Jan Van Herle for their encouraging and insightful comments.

My sincere thanks goes to, Prof. Farhad Rachidi-Haeri for his generosity and friendship. *Farhad*, it was a great honor for me to be with you in the same building, ELL offices of EPFL. You are the main source of the friendly atmosphere in our building. Your generosity, friendship, humanity and responsible feeling for everyone, bring this point in my mind that the world would be definitely a better place to live if we had more people such as you.

I would also like to thank Dr. Dimitri Torregrossa. *Dimitri*, it was very pleasant to work with you during last four years. Thanks for all your help and support.

of the research project entitled "Advanced control of distribution networks with the integration of dispersed energy storage systems".

I am deeply grateful to Mrs. Andrée Moinat and Mrs. Sophie Flynn secretaries of the Laboratory, for all their constant availability, sympathy, and kindness. *Andrée*, *Sophie*, merci beaucoup.

My time at EPFL was made enjoyable by an amicable environment in the laboratory. Tremendous thanks to all the members of ELL building for the friendly atmosphere and the priceless moments (listed without order): Dr. Alexander Smorgonskiy, Dr. Gaspar Lugrin, Jean-Michel Buemi, Dr. Carlos Alberto Romero, Emil Namor, Dr. Lazar Bizumic, Dr. Fabrizio Sossan, Georgios Sarantakos, Andreas Kettner, Asia Codino, Enrica Scolari, Zhaoyang Wang, Asja Derviskadic, Dr. Felix Vega, Dr. Nicolas Mora, Lorenzo Reyes, Dr. Paolo Romano, Dr. Stela Sarri, Dr. Konstantina Christakou, Marco Pignati, Lorenzo Zanni, Dr. Daniele Colangelo, and Sylvain Robert. My special thanks goes to my Iranian friends in ELL: Dr. Reza Razzaghi, Dr. Mostafa Nick, Mohammad Azadifar, Dr. Mokhtar Bozorg, Dr. Omid Alizadeh Mousavi, Dr. Ali Ahmadi-Khatir, and Hossein Mahmoudimanesh,

During my stay in Lausanne, I was fortunate to meet wonderful people with whom I have shared incredible moments. In particular, many thanks goes to Bita, Mohssen, Laili, Elahe, Mahbubeh, Samira, Milan, Naghmeh, Maryam, Parisa, Volker, Majid, Arezu, Elham, Mina, Sina, Masoumeh, Hamed, Mahdad and Amin.

I would like also to thank my best friend, Sara. *Sara*, thanks for being awesome, and for always making me feel happy. You mean the world to me.

Last but not least, my deepest and forever thanks go to my beloved family. To my only brother, Mohsen, for being an important part of my life. *Mohsen*, since early childhood until now, we have gone together in the road of life. Thanks for being next to me. To my lovely parents, Fatemeh and Ata, for their dedication and many years of support, for their endless love and infinite patience and compassion. *Maman*, *Baba*, the reason that I am in this point, the reason that you are now having this thesis in your hands and reading these lines, is all you. Thanks.

And most of all, I wish to express my heartfelt thanks to my beloved husband, *Zagros*, for his love and his patience. *Zagros*, thanks for standing by my side and supporting me. We prove that true love knows no distance.

Lausanne, June 06, 2016

Maryam Bahramipanah

Abstract

Due to the increased penetration of Distributed Generations (DGs) in distribution networks, the system control and operation may become quite different from the case of traditional distribution network. Most DGs can only provide intermittent power to the Active Distribution Networks (ADNs) due to the intermittent nature of the resources such as wind and sun. Moreover, ADN utilities usually do not own DGs, and have difficulty in controlling directly DGs outputs power. The main problem related to the considerable connection of DGs is represented by the quality-of-service of ADNs usually associated to node voltage quality and line congestion mitigation.

Within the above context, the motivating factors for this thesis are supported by the issues related to optimal operation and control of ADNs integrating stochastic and non-stochastic DGs. One of the most promising near-term solution is offered by using distributed Energy Storage Systems (ESSs) which can perform their full role to guarantee a more flexible network. Indeed, the availability of ESSs allows, in principle, to: (i) actively control the power flows into the grid, (ii) indirectly control the voltage profiles along the network feeders and (iii) locally balance the hour/daily and weekly load variations.

In this thesis, ESSs are assumed to be the only controllable devices in ADNs. As a result, DGs can be indirectly controlled by means of ESSs.

First, this manuscript presents control-oriented model for electrochemical ESSs. In this respect, the accurate estimation of ESS behavior is utmost important. A generic charge representative model for any electrochemical ESSs is proposed. Moreover, an improvement of the most common electric equivalent circuit models for the two selected ESSs with different characteristics (namely double layer supercapacitors with high power/low energy densities and electrochemical batteries with low power/high energy densities) is provided for the development of specific control schemes. They are based on the modeling of redistribution of charges that

characterizes the dynamic behaviors of the two devices during long time charging/discharging and relaxation phases.

Second, this manuscript presents advanced control/scheduling algorithm for ADNs. The operation and control of ADNs can be achieved either centrally or in a decentralized way. Due to the large changes in distribution system structure and operation, the question arises whether the centralized management approach is still the most appropriate. The amount of information to be centrally treated would considerably grow due to the number of generation equipment's inserted into the grid and the stochastic operation nature of some of them. In fact, a large amount of data would need to be collected, treated simultaneously and provided quickly for further processes. This consideration introduces the idea that some ADN operation problems, such as voltage control or line congestion mitigation, can be solved in a distributed manner which would help to relieve the information processing burden and to enhance the system security while preventing unwanted event from propagating through the grid. Therefore, the decentralized schemes are considered subdividing the network into quasi-autonomous areas. To this end, given a set of ESSs optimally located in a balanced and radial ADN, this thesis proposes a network partitioning strategy for the optimal voltage control of ADNs. Thus, the network is decomposed into several areas; each under the control of one ESS which has maximum influence on its corresponding area. Based on this clustering, decentralized scheduling strategies and real-time decentralized control algorithms for the clustered ADNs are proposed. The proposed zonal control capability focuses on voltage control and line congestion management. In both proposed decentralized scheduling and real-time control algorithms the communication among different areas is defined using the concept of Multi-Agent Systems (MAS). The agents are defined as entities that are rational, autonomous, reactive, proactive (taking initiatives in pursuing of their goals), flexible, robust to failures and capable to interact with other agents. All the interactions between agents are implemented by mean of message exchanges.

The performance of the proposed models/methodologies and their implementation is assessed through case studies in order to quantify the benefits that can be derived from.

Résumé

En raison de la pénétration grandissante de la production décentralisée (DG) dans les réseaux de distribution, le contrôle et le fonctionnement de ces systèmes est devenue significativement différent comparés au cas des réseaux de distribution traditionnels. La plupart des DG ne peuvent fournir que de l'énergie intermittente aux réseaux de distribution actifs (ADN) en raison de la nature intermittente des ressources telles que le vent et le soleil. De plus, les ADN en général ne sont pas propriétaires des DG, et les opérateurs ont des difficultés à contrôler directement ces DG. Le principal problème inhérent à l'intégration importante des DG est représenté par la qualité du service associée à la tension aux nœuds et à la charge des lignes.

Dans le contexte de cette thèse, les facteurs de motivation sont liés à l'exploitation et le contrôle de réseau de distribution intégrant des DG stochastiques et non-stochastiques. Une solution est proposée en utilisant des systèmes distribués de stockage d'énergie (ESS) pouvant garantir un contrôle plus flexible du réseau. En effet, la présence de ESSs permet, en principe, de: (i) contrôler activement les flux de courant dans le réseau, (ii) contrôler les profils de tension le long des feeders et (iii) compenser localement les variations de charge horaire ou journalière.

Dans cette thèse, les éléments ESSs sont supposés être les seuls dispositifs contrôlables dans les ADNs. Par conséquent, on considère que les DG sont contrôlés indirectement par l'intermédiaire de ces éléments.

Tout d'abord, ce manuscrit présente un modèle dédié pour le contrôle d'éléments électrochimiques ESS. A cet égard, l'évaluation précise du comportement des ces éléments est très important. A ce sujet, un modèle générique pour la représentation des charges pour tout ESS électrochimique est proposé. En outre, les modèles de circuit électrique les plus couramment utilisés pour le contrôle ont été améliorés. Ces modèles concernent les supercapacités double couche et les batteries au Lithium. L'amélioration repose essentiellement sur la modélisation de la redistribution des

charges qui caractérise le comportement dynamique de ces 2 types d'éléments pendant la charge/décharge à long terme et les phases de relaxation.

Par la suite, ce manuscrit présente deux algorithmes pour le contrôle planifié des ADNs. Ce contrôle peut être effectué de manière centralisée ou de manière décentralisée. En raison des grandes modifications dans la structure et l'exploitation des systèmes de distribution, la question se pose de savoir si l'approche de gestion centralisée est toujours la plus appropriée. En effet, La quantité d'informations à traiter de manière centrale tend à augmenter considérablement en raison du nombre d'équipements de production insérés dans le réseau et la nature stochastique du fonctionnement de certains d'entre eux. En fait, une grande quantité de données devrait être collectées, traitées simultanément et fournies rapidement à d'autres processus. Cette considération introduit l'idée que certains problèmes de fonctionnement, tels que le contrôle de la tension et/ou de la congestion des lignes, peuvent être résolus d'une manière distribuée contribuant ainsi à alléger la charge de traitement de l'information et améliorer la sécurité du système en empêchant la propagation de perturbations indésirables dans le réseau. Par conséquent, le régime décentralisé suggère de subdiviser le réseau en des zones quasi autonomes. À cette fin, étant donné un ensemble de ESSs optimalement installés dans un réseau, cette thèse propose une stratégie de partitionnement du réseau pour le contrôle de la tension optimale des réseaux. Ainsi, le réseau est décomposé en plusieurs zones ; chacune sous le contrôle d'un ESS ayant une influence maximale sur la zone correspondante. Sur la base de cette classification, des stratégies de contrôle pour l'exploitation planifié (2 variantes) et l'exploitation en temps réel (1 variante) selon une approche décentralisée sont proposées. Le contrôle de zone proposée se concentre sur celui de la tension et de la gestion de la congestion des lignes. Pour ces trois variantes, la communication entre les différentes zones est définie en utilisant le concept de systèmes multi-agents (MAS). Les agents sont définis comme des entités qui sont rationnels, autonomes, réactifs, proactifs (prendre des initiatives en poursuivant leurs objectifs), flexibles et robustes aux pannes et capables d'interagir avec d'autres agents. Toutes les interactions entre les agents s'effectuent au moyen d'échange de messages.

La performance des modèles / méthodologies proposés et de leur application est évaluée à l'aide d'études de cas afin de quantifier les avantages qui peuvent en être tirés.

Mots clefs : réseaux de distribution actifs, effet de redistribution de charge, contrôle décentralisé, supercapacité à double couche, systèmes de stockage d'énergie, gestion de la congestion des lignes, batteries au Lithium, système multi-agents, partitionnement du réseau, contrôle de la tension aux nœuds, état de charge.

Contents

List of Figures

List of Tables

List of Acronyms

ADN	**A**ctive **D**istribution **N**etwork
Ah	**A**mpere-**h**ours
ALC	**A**rea **L**ocal **V**oltage **C**ontrol
ANN	**A**rtificial **N**eural **N**etwork
ARAC	**A**rea **R**eference **A**ngle **C**orrection
BA	**B**ESS **A**gent
BESS	**B**attery **E**nergy **S**torage **S**ystem
CA	**C**oordination **A**gent
CBB	**C**ommon **B**oundary **B**us
CDF	**C**umulative **D**istribution **F**unction
CR Model	**C**harge **R**epresentative **M**odel
Crate	discharge **C**urrent **rate**
DG	**D**istributed **G**eneration
DLC	**D**ecentralized **L**ocal **C**ontrol
DLF	**D**istributed **L**oad **F**low
DLSC	**D**ouble **L**ayer **S**uper**C**apacitor
DNO	**D**istribution **N**etwork **O**perator

EA	ESS Agent
E&C	Exchange and update of CBBs information & Convergence condition check
EIS	Electrochemical Impedance Spectroscopy
ESS	Energy Storage System
ETTC model	Enhanced Two Time Constant model
FACTS	Flexible Alternating Current Transmission System
FIPA	Foundation for Intelligent Physical Agents
IE cost	Imported/Exported energy costs
IID	Independent and Identically Distributed
KiBaM	Kinetic Battery Model
LTO	Lithium-Titanate battery cell
MAS	Multi-Agent System
MBC	Model-Based Control
MCS	Monte Carlo Simulation
OLTC	On-Load Tap Changer
OPF	Optimal Power Flow
PDF	Probability Distribution Functions
PLF	Probabilistic Load Flow
PL&C	Power Limits & Cost profile
PVs	Photovoltaic panels
QoS	Quality-of-Service
RMSE	Root-Mean-Square Error
SoC	State-of-Charge
SoE	State-of-Energy

TEMP	**T**hévenin **E**quivalent **M**odel **P**arameters
TTC model	**T**wo **T**ime **C**onstant **model**
VIF	**V**oltage **I**nfluence **F**actor
VR	**V**oltage **R**egulator
VSC	**V**oltage **S**ensitivity **C**oefficients

Nomenclature

t	Time index
t_0	Initial time
Δt	Time-step
i,j,g,u,r,s,b	Index of nodes
d	A given day
N	Number of network nodes
N^*	Number of the internal nodes in an area
B	Number of ESS units located in ADNs
Γ	A given network operating state
k	Number of areas
n	Level number of an area
τ	Time constant
γ	Status of EAs
C_{rated}	Rated capacity of ESS
E_{nom}	Rated energy of ESS
$CBB^{A_{h \cdot g}}$	CBB of both areas A_h and A_g
V_{dc}	DC terminal voltage of ESS

V_{oc}	Open circuit voltage of ESS
V_{dc}^{F}	DC final voltage of ESS
V_{dc}^{m}	DC measured terminal voltage of ESS
$\left|\overline{V}\right|$	Node voltage magnitude
δ	Node voltage angle
V_{ref}	Voltage reference value
$\overline{V}^{init}$	initial value of node voltage
$\Delta\left|\overline{V}\right|$	Voltage variation provided by ESS
$V_{BESS}^{dc,min}, V_{BESS}^{dc,max}$	Minimum, maximum DC voltage value of ESS
I_{dc}	DC current of ESS
$I_{BESS}^{dc,min}, I_{BESS}^{dc,max}$	Minimum, maximum DC current value of ESS
I_{sr}	Line current between node r and s
I_{sr}^{max}	Ampacity of line sr
$\Delta\left|\overline{I_{sr}}(t)\right|$	Current variation provided by ESS
I_{CH}, I_{RED}	Virtual current sources during charge/discharge, resting for DLSC
I_{vir}	Virtual current generator for BESS
$I_{\Delta t}(t)$	Average charge/discharge current
P	Active power
P_{BESS}^{dc}	DC active power of BESS
Q	Reactive power
R	Resistance

C	Capacitance
Z	Impedance
E_m	Electromotive force of the BESS
SoE_{ref}	SoE reference value
SoE_{min}, SoE_{max}	Minimum, maximum of SoE
$\left[VSC^P\right]_{B\times N}, \left[VSC^Q\right]_{B\times N}$	Voltage sensitivity coefficient matrices for active/reactive powers variations
$\left[VIF^P\right]_{B\times N}, \left[VIF^Q\right]_{B\times N}$	Voltage influence factor matrices for active/reactive powers variations
Λ^P, Λ^Q	Power sensitivity coefficients with respect to both P/Q
Π^P, Π^Q	Current sensitivity coefficients with respect to both P/Q
$\overline{Y}$	Network admittance matrix
$\left\|\overline{Y}\right\|$	magnitude of the admittance matrix
θ	phase of the admittance matrix
$\alpha\left(I_{dc}(t)\right)$	ESS charge/discharge efficiency coefficient
$C\left(I_{dc}\right)$	ESS capacity for current discharge rate I_{dc}
Q_{in}, Q_{out}	Charges stored/ extracted in/from the ESS
Q_R	Redistribution charge
Q_{oc}	Available charge
ΔQ	Extracted charge
ΔQ_{RED}	Amount of charge to be redistributed
$\left[\alpha\right]_{B\times N}, \left[\beta\right]_{B\times N}$	Weighted coefficients accounting for resistance and reactance electric distance
$\beta_i, \lambda, a, b, c$	Weighting the terms of the objective function

η_i	Coefficients for share of each time constant
P_{conv}^{loss}	Power losses of the converter
Ψ	Efficiency of the converter
S_r	Rated power of the converter
$\overline{Z}_{thev}$	Thévenin impedance seen from CBBs
$\overline{V}_{thev}$	Thévenin voltage seen from CBBs
S_s	Losses plus supply-demand power mismatches
$\overline{S}_{CBB}$	Equivalent apparent power flowing through CBB

1   Introduction

1.1   Motivation of the Thesis

In traditional power systems, energy was transported through the transmission system to the distribution system and then delivered to the consumers. This structure is extremely unidirectional and hierarchical. In the last decades, the connection of Distributed Generations (DGs) in distribution networks increased exponentially. As a result, it gives rise to the need for a bidirectional supply/demand system. Comparing with conventional bulk generations, DGs are smaller scale and located closer to the loads. Thus, they can supply power to loads without needing a transmission network. Therefore, it significantly decreases power losses, voltage drops and grid investment costs [1]. However, the massive connection of DGs triggers different operation challenges in Active Distribution Networks (ADNs)[1], and creates a variety of well-documented impacts of voltage rise, particularly in rural networks [2]. Most DGs can only provide intermittent power to the ADN due to the intermittent nature of the resources such as wind and sun [3]. Thus, there is no direct control over them (e.g., [4], [5]). Moreover, ADN utilities usually do not own DGs, and have difficulty in controlling DGs output powers. Therefore, with an increasing level of DGs penetration, the control and operation of ADN may become quite different from the case of traditional power systems. In general, the main

---

[1] According to definition set by CIGRE WG C6.11 [169], "Active distribution networks (ADNs) have systems in place to control a combination of distributed energy resources (DERs), defined as generators, loads and storage. Distribution system operators (DSOs) have the possibility of managing the electricity flows using a flexible network topology. DERs take some degree of responsibility for system support, which will depend on a suitable regulatory environment and connection agreement".

obstacle related to the considerable connection of DGs is represented by the quality-of-service (QoS) of ADNs usually associated to node voltage quality ([6]) and line congestion mitigation [7].

The issue of voltage regulation in ADNs is evoking more interest than traditional distribution networks due to the potential of distributed energy resources to contribute in voltage regulation [8]. Any fluctuation in real power brings about a proportional fluctuation of voltage. This is particularly evident in cases of weak networks where the line resistances are high relatively to their reactances. Voltage regulation is a procedure to keep voltages in an ADN within normal limits, which is usually ±5% of the rated voltage.

The increased penetration of DGs may also cause line congestion, which may severely degrade network performances [7].

In what follows the existing solutions to the problems of voltage control and line congestion management are clustered in terms of controlled resources. In particular, we refer to the control of: DG units, network reconfiguration and primary substation transformers on-load tap-changers.

Through the collection of voltage measurements from predefined points, it is possible to define sub-optimal control strategies, usually relying on droop controls applied to reactive power injections, deployed in DG Voltage Regulators (VRs) (e.g., [9],[10]). However, such regulation mechanism may no longer be suitable in view of the following reasons:

(i)   In networks characterized by high R/X ratios of longitudinal line impedances, the reactive power compensation relying on those DGs' inverters could not be sufficient to achieve satisfying voltage control.

(ii)   DG might be automatically disconnected by their protections when voltage fluctuations are more than ±10% [11]. This exacerbate further voltage fluctuations which may trigger other DGs disconnections and cascading voltage fluctuations.

(iii) The control actions of the VRs are sub-optimal since the knowledge of the system state is unknown to the control mechanism.

(iv)   VR's estimations of node voltages will certainly be disturbed by the operations from uncontrolled DGs leading consequently to incorrect VR's operations. Therefore, it becomes hard for VRs to use the local measurement to estimate the voltage drop along the feeders. Farag et. al. [8] studied the impacts of DGs on conventional voltage regulation schemes, and claimed that applying conventional utility voltage regulation control methods in ADNs is infeasible.

Concerning the deployment of the control strategies involving DG power output regulation, it is worth observing that DGs can be controlled in different ways (e.g., [12], [13], [14]). However, the optimal coordination of hundreds of inverters might require a complex telecommunication infrastructure leading to high investments. In addition, the active power control by DGs might be not permitted due to the existing grid code for prosumers.

Another solutions proposed to handle voltage control and line congestion management is the reconfiguration of the grid [15]. However, the aforementioned approaches, together with the traditional grid reinforcement one, are expensive since they require the installation of additional hardware represented by cables/overhead lines and/or breakers.

Another solution is to use on-load-tap-changing (OLTC) substation transformer to keep the voltage on the feeder within the normal operational limits. Determining proper control settings for OLTC becomes quite challenging when there are multiple DGs on a feeder (e.g., [16] [17], [18]). Also, these devices do not provide fast enough voltage regulation and do not affect the line congestion. Also, OLTC-based voltage control is sub-optimal since do not allow for a flexible control in the different network buses. Furthermore, the number of allowed OLTC switching operations is limited involving consequent maintenance cost considerations for DNOs.

Within the above context, the motivating factors for this thesis are supported by the issues related with optimal operation and control of ADNs integrating stochastic and non-stochastic DGs.

1.2 Objectives and Contributions of the Thesis

In order to maintain the quality of service of ADNs with high penetration of DGs, an alternative solution is offered in this thesis by using distributed ESSs which can perform their full role to guarantee a more flexible network. This is one of the most promising near-term solutions allowing postponing into infrastructure investments. As a result, DGs can be indirectly controlled by means of ESSs. Indeed, the availability of ESSs allows, in principle, to: (i) actively control the power flows into the grid, (ii) indirectly control the voltage profiles along the network feeders and (iii) locally balance the hour/daily and weekly load variations. In fact, energy storage can be seen not only as an energy buffer, but also as real-time reservoirs that can react to power imbalances of the grid [19].

In this respect, in this thesis, ESSs are supposed as a good solution for optimal operation and control of ADNs. Line congestion mitigation, voltage support and, eventually, spinning reserve management can be achieved through ESSs. ESSs are assumed to be the only controllable devices of ADN regulators. Thus, the aim is to

control the node voltages and line congestion management with a limited number of ESSs. Therefore, the main contributions of this thesis are listed hereafter.

1) Proposition of a generic charge representative model for any electrochemical ESSs. This model accounts for a stable and accurate state-of-charge estimation framework.

2) Improvement of the most common electric equivalent circuit models for two ESS devices; namely double-layer supercapacitors with high power/low energy densities and electrochemical lithium-based batteries with low power/high energy densities, suitable for the development of specific control schemes.

3) Proposition of a network partitioning strategy for the optimal voltage control of ADNs by means of ESSs.

4) Proposition of two decentralized operational scheduling algorithms relying, respectively, on the Thévenin equivalents and a recursive approach in clustered ADNs.

5) Proposition of a real-time adaptive model-based decentralized voltage control and line congestion management algorithm for the clustered ADNs relying on an accurate dynamic model of Battery Energy Storage Systems (BESSs) capable to account for their DC active power limits.

It is worth underlining that proper siting and sizing of storage units is out of the scope of this work, and they are considered as an input element of the problem.

1.3 Thesis Structure

The structure of the thesis dissertation is as follows.

Chapter 2 – Part I. presents first an overview of the three main phenomena taking place inside of any electrochemical ESSs. Then, a novel and efficient ESS generic charge representative model is presented.

Chapter 2 – Part II. presents a brief history of different dynamic model of double layer supercapacitors with high power density which fit the applications into ADNs. Then, a detailed dynamic models is proposed to enhance the dynamic behavior by representing the so-called charge redistribution phenomenon that characterizes the dynamic of the storage system voltage during long time charging/discharging and relaxation phases. Also, making reference to experimental tests carried out on a 325F supercapacitor in DESL-EPFL Smart Grid Laboratory, the optimal parameters

assessment of the relevant model is discussed and, then, the improvement of the model behavior with a minimal computational overhead is demonstrated.

Chapter 2 – Part III. presents first an overview of the existing dynamic model of Lithium-based batteries which are one of the ESS technologies matching the requirement of ADNs. Their mains advantages are the relative high value of energy density and long life duration as well as, in certain cases, limited environmental impact. Then, a detailed dynamic model is proposed accounting for redistribution of charge effects. For this purpose, the optimal parameters assessment of the relevant model is performed, then, the improvement of the model behavior is shown making reference to a Lithium-Titanate battery in DESL-EPFL Smart Grid Laboratory.

Chapter 3 – Part I. presents first the downsides of centralized control paradigm for ADNs. It is shown that a possible solution is to move from the centralized operation paradigm to the decentralized one subdividing the network into quasi-autonomous entities defined as areas. To this end, a network partitioning strategy for the optimal control of ADNs is proposed. Voltage sensitivity concept is used in order to linearize the problem.

Chapter 3 – Part II. presents first different power scheduling methods existing in the literature. Then, two decentralized operational scheduling algorithms are proposed relying, respectively, on Thévenin equivalents and a recursive approaches. The communication among different areas is defined using the concept of multi-Agent Systems (MAS). The effectiveness of the proposed zonal scheduling methods is assessed and compared with the equivalent centralized scheme using test cases composed of the IEEE 13 and IEEE 123 nodes distribution test feeders.

Chapter 3 – Part II. presents first a brief history of different voltage and power flow control techniques. Then, a novel real-time decentralized control algorithm for the clustered ADNs using only distributed BESSs is proposed. In particular, we propose a zonal control strategy targeting voltage support and line congestion management. The proposed zonal control relies on an accurate dynamic model of BESSs capable to account for their DC active power limits. The effectiveness of the proposed zonal scheduling methods is assessed using test cases composed of the IEEE 13 nodes test feeders.

Chapter 4 summarizes the main contributions of this research and provides an outlook on potential future works.

2 Control-Oriented Model of Electrochemical Energy Storage Systems

Summary

This chapter focuses mainly on the modeling of electrochemical energy storage systems. These energy storage technologies play a key role especially in mobility and power distribution network applications in view of their relative high value of energy/power densities, long life duration and, in certain case, a limited environmental impact. Two energy storage systems characterized by opposite characteristics are selected for this purpose; namely double layer supercapacitors with high power/low energy densities and electrochemical batteries with low power/high energy densities. In this respect, an improvement of the most common electric equivalent circuit models for the two devices is provided for the development of specific control schemes. It is based on the modeling of redistribution of charges that characterizes their dynamic behaviors of the two devices. The redistribution of charge consists three effects, namely rate capacity effect, recovery effect, and hysteresis effect.

This chapter includes three parts. Part I presents a generic charge representative model for energy storage systems. Part II and part III illustrate a detailed dynamic models for supercapacitors and batteries respectively.

Introduction

Within the context of power systems, the typical use of ESSs refers to ancillary services like: peak shaving, voltage control, line congestion management and frequency support. Each of the above-listed applications is characterized by charge/discharge cycles that could range from fraction of a seconds (typically in high-power applications) to hours or even days (in high-energy applications). In this respect, the availability of accurate ESSs model capable to accurately predict the dynamic behavior accounting for the internal effect of redistribution of charge is a key aspect for the definition of model-based controls in power grid applications.

In general, in the field of system identification, there are three types of models; namely white-box model (purely physics-based), black-box model (purely empirical data driven) and gray-box model (combination of physics and data driven).

White-box model is based on the chemical reactions taking place inside the electrochemical ESSs. It uses detailed physics based equations to model and predict the behavior of ESS devices such as state of charge and energy, dynamic voltage behavior and etc. Due to the detailed dynamic equations, this model can capture all the dynamic of the ESSs. However, in many cases, it is time consuming to develop/solve due to the complex nature of the systems and processes.

Black box model is a purely data driven model. Usually statistical methods are used to build mathematical models of ESSs from measured data and capture the correlation between the state of dynamic systems and operation data. Thus, it includes the optimal design of experiments for efficiently generating informative data to fit the models. This model needs on-site measurements over a certain period of time to train the models able to predict the state of the device. It is widely applied in order to reduce computation cost. However, since this model cannot capture all dynamics of the ESSs, it may result in unfeasible operating points.

Gray-box model is a hybrid model using simplified physical descriptions to simulate the behavior of ESS. Thus, the requirement of training datasets, and calculation time are reduced compared to white- and black-box models. Model parameters are identified based on the operation data using parameter identification methods. In this respect, optimal parameters are determined in order to minimize the errors between model prediction and real measurements.

ESSs cover a wide spectrum of applications into electrical networks ranging from: support to fast power quality a-periodic disturbances to daily/weekly energy balance. Therefore, the usual way to categorize ESSs is to classify them as a function of their specific energy and power densities and, also, as a function of their dynamic behavior. In particular, high-power applications refer to the compensation of instantaneous unbalances caused, for instance, by fluctuations of renewable

generation (e.g. wind gusts) or short circuits (e.g. enhancement of ride-through capability of DG), whilst high-energy applications refer to the time-shifting of energy production/consumption due to slow variations in renewables generation. Therefore, we have selected in this thesis, on purpose, two energy storage devices characterized by opposite characteristics; namely Double Layer Supercapacitors (DLSCs) with high power and low energy densities and electrochemical batteries with low power and high energy densities. In this chapter, detailed different dynamic models existing in the literature for these devices are presented and an enhanced model is proposed for each of them. It is capable to capture all dynamics as well as the effect of the redistribution of charge.

The structure of this chapter is organized as follows: in part I first the effect of charge redistribution taking place in electrochemical ESSs are presented and then a generic ESS charge representative model is proposed considering for those effects. In part 2.3 detailed dynamic models for supercapacitors and batteries are presented. It is shown that the proposed models can capture the dynamics of the devices.

Part I. Generic ESS Charge Representative Model

2.1.1 Charge Redistribution Effect

A schematic illustration of typical circuit of electrochemical ESS is shown in Figure 2-1.
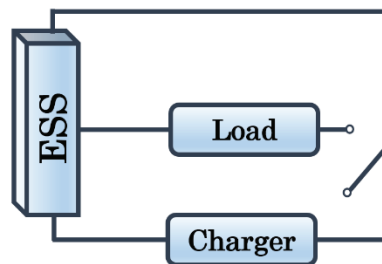
Figure 2-1 Schematic illustration of typical circuit of ESS

When an ESS is connected to an external source (charger), the infinite charges are stored in the electrolyte. When the ESS is connected to an external load, the stored charge is released and the current is generated through the external circuit. In general, it can be assumed that several layers of charges are formed in the electrolyte due to the potential difference across the ESS's terminal. These layers can be modeled as two main wells [20] named as available well and storage well. This schematic is shown in Figure 2-2.

In particular, the charges are directly delivered/supplied through the available well to/from load/power supply. The storage well delivers/supplies charges only to the available well. The rate of charge flow between the two wells is represented by k, and the difference in the charge heights of the two wells is shown by h_1 and h_2. This model can be equivalent to the electrical circuit shown in Figure 2-3, where c_1 and c_2 model the capacity of the available and storage wells that are connected through R which models k.
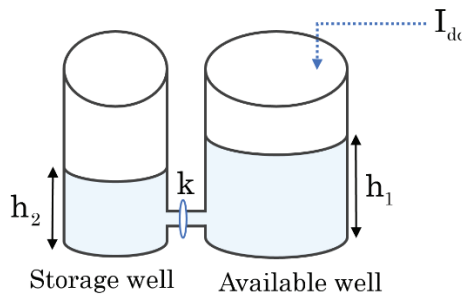
Figure 2-2 Generic ESS charge representative model
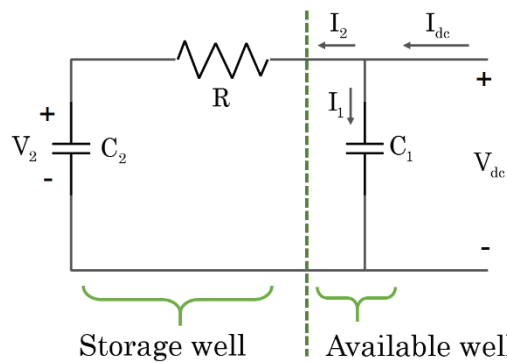
Figure 2-3 Equivalent circuit of charge representative model

The charge exchanged between these two layers is the major responsible of the ESS nonlinear behavior, and results in three main effects; namely, rate capacity effect, recovery effect and hysteresis effect.

1) *Rate capacity effect*

It is known that by increasing the load current, the capacity of ESSs is fading. In other words, less charge can be drawn from ESSs when the discharged current is increased. This effect is called rate capacity. When the discharge current is

increased, the charges in the storage well do not have enough time to become accessible to the available well. Thus, the ESS capacity will decrease.

2) Recovery effect

This effect takes place when the ESS is disconnected from load/charger (resting phase). If the ESS is disconnected from the load, the charges in the storage well become available, which leads to an increase of the ESS terminal voltage. On the contrary, if the ESS is disconnected from the source, the accumulated charges in the available well will go to the storage well; which leads to a decrease of the ESS terminal voltage. These phenomena are called recovery effect.

3) Hysteresis effect

The ESS cell equilibrium voltage depends on its charge and discharge history, and it exhibits hysteresis. The hysteresis is generated due to the thermodynamic entropic effects, mechanical stress and concentration and activation polarization. It causes the discharging voltage curve to stay below the charging voltage curve for the same state of charge.

2.1.2 Charge Representative Model (CR model)

Accounting for the three described effects taking place in any electrochemical ESSs, a general model can be developed regardless the different characteristics of the considered ESSs. This general model is called "*Charge Representative (CR) model*". CR model is represented by State-of-Charge (SoC) indicator. In this respect, ESS is modeled as an ideal reservoir of charge. SoC is used to indicate the available amount of charge that can be extracted from the system at a given discharge current rate (Crate). It is defined in per unit (0 = full-discharged; 1= full-charged).

ESS behavior depends on its utilization conditions like current profile, and ambient temperature. Therefore, to ensure a reliable system, precise estimation of SoC plays a significant role in developing of an intelligent ESS management system for real-time applications. Estimating the value of SoC of an ESS represents a challenging task, since neither the remaining capacity nor the SoC can be directly measured. Several SoC estimation methods have been developed based on different techniques (e.g., [21], [22], [23], [24]). Each method has its own advantages and disadvantages. These methods can be mainly classified into two groups: (1) direct measurement-based estimation and (2) model-based estimation. The former method directly uses the measurements from ESSs to calculate the SoC. The latter method utilized the ESS model to estimate the SoC. It benefits from accurate modelling of the ESS behavior in all the operating conditions. In what follows, we describe each of the two groups and their different techniques.

1) *Direct measurement-based SoC estimation*

a) Coulomb (Ampere-hours (Ah)) counting algorithm (e.g., [25], [26], [27], [28] [29], [30])

The most common technique for determining the SoC is Ah counting technique. This method can easily be implemented by integrating the output current of the ESSs over the time. This approach seems to be the most attractive for online SoC estimation, since it is simple to implement with a low computational effort. However, it is very sensitive to measurement errors, particularly those caused by the current sensor. In addition, this algorithm requires to be correctly initialized with the initial SoC value, which may not be available. Also, it can easily become flawed because the efficiency and initial capacity of the ESSs vary with respect to time and temperature, meaning that a large error may eventually occur. The shortcomings of this method is often corrected by its combination with the other methods.

b) Open circuit voltage algorithm (e.g., [31], [32], [33], [34], [35], [36], [37])

Another simple way to estimate the SoC is to make use of the relationship between SoC and open circuit voltage (V_{oc}). V_{oc} gives an indication of the available charge. This method can be easily implemented. However, measuring V_{oc} requires the ESS being in steady state condition that is reached only after a long time with no load current. Thus, this approach is unsuitable for real-time SoC estimation, when the ESS is continuously charged or discharged at high currents.

c) Algorithm using Electrochemical Impedance Spectroscopy (EIS) (e.g., [38], [39], [40], [41], [42])

The electrochemical impedance of ESSs characterizes their dynamic behaviors. The measured values of the impedance depend greatly on the measurement method and they are sensitive to measurement conditions. Furthermore, the type of relationship between this impedance and the SoC is not generic for all ESS technologies. Also, this method requires additional specialized hardware to excite the dynamics of the ESSs. Due to hardware complexity and high cost, it is difficult to implement the algorithm in real-time contexts.

2) *Model-based SoC estimation or machine learning methods*

a) Artificial Neural Networks (ANN) (e.g., [43], [44], [45], [46], [47])

The ANN methods can be quite accurate with sufficient offline data. However, the computational effort is particularly high and their performance highly depends on the quantity and quality of the data set. A large amount of offline tests is necessary to obtain a good model. However, it can be very time-consuming.

b) Fuzzy logic (e.g., [48])

Fuzzy logic method is used to estimate SoC by using the training datasets obtained through impedance spectroscopy or coulomb counting techniques. Thus, the fuzzy logic approach includes the disadvantages of these two techniques.

c) Model-based filtering methods (e.g., [31], [49], [50], [51], [52], [53], [54], [55], [56], [57], [58], [59], [60], [61], [62], [63], [64], [65], [66], [67], [68], [69])

Many optimum state estimation approaches have been investigated for the model based filtering method, such as sliding mode observer, and Kalman filter. The estimated values of the system are compared with the observed ESS behavior. It has high estimation accuracy and state error correction capability. However, the implementation of this method for real-time applications is computationally intensive and can take a long time to converge.

2.1.2.1 SoC Estimation Proposed Algorithm

Among all different SoC estimation methods, Ah counting algorithm is the best one suitable for real-time applications, due to its low computation burden and simple implementation. Belvedere et al. [29] in 2012 presented an estimation algorithm using Ah technique using (2.1).

$$SoC\left(t\right) = \frac{C\left(t_0\right) + \int_{t_0}^{t} \alpha\left(I_{dc}\left(t\right)\right) I_{dc}\left(t\right) dt}{C\left(I_{dc}\left(t\right)\right)} \tag{2.1}$$

Where $C\left(t_0\right)$ is the battery capacity at the initial time t_0. $I_{dc}\left(t\right)$ is the instantaneous value of ESS current. The current is assumed to be positive during charging phase and negative during discharging phases. $\alpha\left(I_{dc}\left(t\right)\right)$ is the ESS charge/discharge efficiency coefficient. $C\left(I_{dc}\left(t\right)\right)$ is the storage capacity for current discharge rate $I_{dc}\left(t\right)$ at constant electrolyte temperature. It is computed by knowing the array of values $C(I^*) = \left\{C(I_0^*), ..., C(I_k^*), ..., C(I_n^*)\right\}$ that defines the ESS capacities at various constant discharge rates I_k^*. These data are typically provided by the cell manufacturer or they can be experimentally inferred. In this work, the temperature is assumed to be constant. It is worth to mention that here only the main concept is reported and we suggest the readers to read [29] for further details. $\alpha\left(I_{dc}\left(t\right)\right)$ is assumed equal to one for the sake of simplicity in [29]. (2.1) can be written in discrete time format as (2.2) for the specific time window $\begin{bmatrix} t_0 & t \end{bmatrix}$ with time-step Δt.

$$SoC(t) = SoC(t - \Delta t) + \frac{\alpha(I_{\Delta t}) \cdot I_{\Delta t}(t) \cdot \Delta t}{C(I_{\Delta t}(t))} \tag{2.2}$$

It is assumed that $SoC(t_0)$ has been already estimated. If $I_{\Delta t} \in \begin{bmatrix} I_k^* & I_{k+1}^* \end{bmatrix}$, where I_k^* indicates various constant Crates used to define the array $C(I^*)$, then

$$C(I_{\Delta t}) = \frac{C(I_k^*) + C(I_{k+1}^*)}{2} \tag{2.3}$$

$I_{\Delta t}(t)$ is the average charge/discharge current within the time window.

$$I_{\Delta t} = \frac{I_{dc}(t - \Delta t) + I_{dc}(t)}{2} \tag{2.4}$$

It is obvious that the rate capacity effect is accounted by $C(I_{\Delta t})$. However, the two recovery and hysteresis effects are not considered in this method. They have a notable effect on SoC estimation accuracy, and it is therefore important that the model should incorporate these phenomena.

In this thesis, a novel SoC estimation method accounting for all charge redistribution effects is proposed based on the method presented [29]. For this purpose, the following experimental tests are performed making reference to a Lithium-Titanate cell (LTO) characterized by a 30 Ah rated capacity and a nominal cell voltage of 2.3V.

- Test I. finding $C(I^*)$ array

Step 1: Start the test from fully-charged battery[1].

Step 2: The battery cell is discharged with Crate[2] corresponding to I_k^* until reaching the minimum voltage.

Step 3: The computed extracted charge during discharging phase is considered as the capacity for I_k^*.

---

[1] The battery is fully-charged when the maximum voltage is reached. Then it is continued to be charged in constant voltage mode until the minimum current is reached (3A).
[2] Crate is a measure of the rate at which an ESS is discharged relative to its maximum capacity. 1Crate is the discharge current equal to the nominal one.

Step 4: Steps 1-3 are repeated for different Crate values.

Therefore, $C(I^*) = \{C(I_0^*), ..., C(I_k^*), ..., C(I_n^*)\}$ is obtained.

- Test II. Find $V_{oc} - \boldsymbol{SoC}$ curve

The initial voltage is used to estimate the initial SoC. For this purpose, the voltage range is divided to n intervals $\{V_{dc,1}^F, V_{dc,2}^F, ..., V_{dc,n}^F\}$. The following test has been carried out.

Step 1: Start the test from fully-charged battery.

Step 2: Discharge the battery with 1Crate until reaching $V_{dc,i}^F$.

Step 3: The battery rests for 30 minutes.

Step 4: V_{oc} is measured which is related to the corresponding SoC.

Step 5: Steps 1-4 are repeated for i= {1, 2, ..., n}.

In order to account for hysteresis and recovery effect, $\alpha(I_{\Delta t})$ in (2.2) should be computed. For this purpose, the following test is carried out to consider for hysteresis effect.

- Test III. Find $\alpha(I_{\Delta t})$ to account for hysteresis effect (for charging and discharging phases).

Step 1: Start the test from fully-discharged battery.

Step 2: The battery is charged with iCrate where i={1, 2, ..., n} until reaching the maximum voltage. The charges stored in the battery is then computed (Q_{in}).

Step 3: The battery is discharged with iCrate until minimum voltage is reached. The charges extracted is computed (Q_{out}).

Step 4: α is computed for iCrate as follow

$$\alpha(iCrate) = \frac{Q_{out}(iCrate)}{Q_{in}(iCrate)} \qquad (2.5)$$

Step 5: Steps 1-4 are repeated for different Crate (different i). So, the $(\alpha - I)$ curve is obtained. This curve is shown in Figure 2-4.

Step 6: If $I_{\Delta t}$ is between two discretized values, the associated $\alpha\left(I_{\Delta t}\right)$ can be inferred by a linear interpolation between these two values.
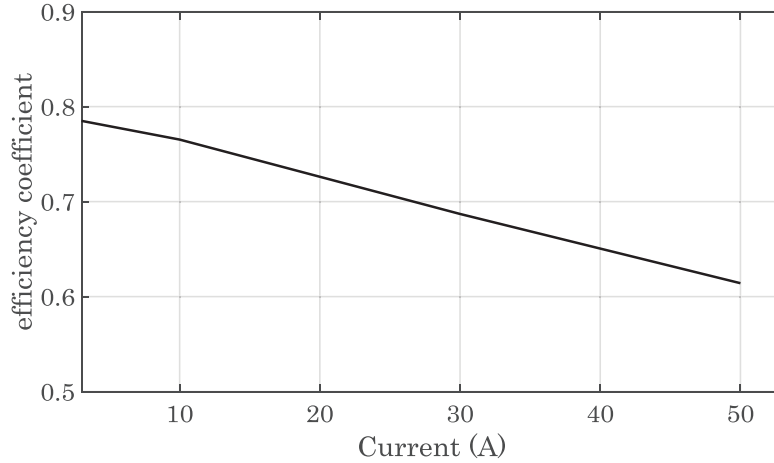
Figure 2-4 Efficiency coefficient versus Crates

As known, the recovery effect is taking place in the resting phase with I_{dc} equal to zero. Thus the SoC remains constant using (2.2). In other words, it cannot account for the exchanged charges between the two wells in the resting phases (recovery effect). In order to account for this effect in the proposed SoC estimation method, the amount of charge in the available well should be compute. In this respect, from Figure 2-3 we can see that if $I_{dc} = 0$ then $I_{rest} = I_1 = -I_2$. SoC accounts for the charge changes related to $I_1\left(\Delta Q_1\right)$. This charge can be computed by

$$\Delta Q_1 = c_1 \cdot \Delta V_1 = c_1 \cdot \Delta V_{dc} = c_1 \cdot \left(V_{dc}\left(t\right) - V_{dc}\left(t_0\right)\right) \tag{2.6}$$

c_1 is the capacity of the available well which is dependent on the ESSs technologies. Moreover, since there is no external current flow, $C\left(I_{\Delta t}\right)$ is equal to the nominal capacity of the ESS (C_{rated}). As a result, SoC is computed using (2.7) for the resting phase when $I_{dc} = 0$.

$$SoC\left(t\right) = SoC\left(t_0\right) + \frac{c_1 \cdot \left(V_{dc}\left(t\right) - V_{dc}\left(t_0\right)\right)}{C_{rated}} \tag{2.7}$$

2.1.2.2 Experimental Validation

a) Case of Lithium-Titanate battery

In order to validate the proposed SoC method, two sets of tests have been carried out for charge and discharge cases.

- ▪ <u>Test IV</u>. Validation for charging phases

Step 1: The fully-discharged battery is charged with 1Crate until reaching fully-charge condition.

Step 2: The battery rests for 30 minutes.

Step 3: The battery is charged again (with 1Crate).

Step 4: Steps 2-3 are repeated until the battery cannot accept any charge (the current goes to zero).

SoC is computed with the algorithm proposed in [29] (Belvedere method with $\alpha = 1$) and the proposed method. The voltage, current and SoC profiles are shown in Figure 2-5.

As it is seen from the current profile, after resting, the battery starts again to receive charge but with lower current value.
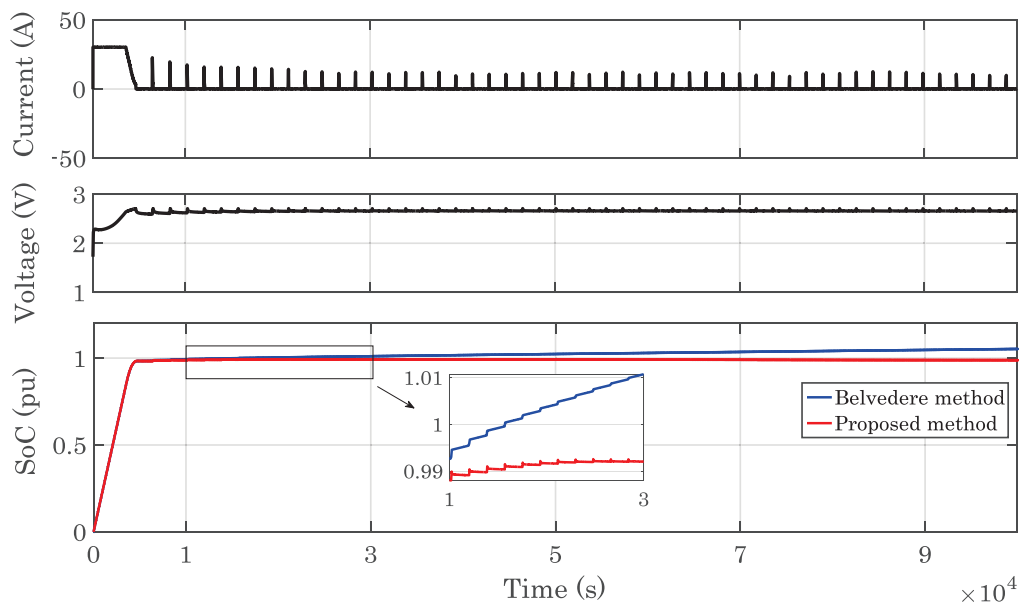
Figure 2-5 Charge test for SoC validation for battery

The charges go to the storage well in the resting phase. Indeed, SoC is the indicator for the charges in the available well. For this reason, the SoC in resting phase is

decreased. As it is seen in Figure 2-5, after t=15710s the SoC is higher than 1 with Belvedere method; which is the major drawback of this method. It is seen that the proposed method can precisely capture the charge redistribution effects and it estimates the SoC with a very high accuracy.

- Test V. Validation for discharging phases

Step 1: The fully-charged battery is discharged with 1Crate until reaching the minimum voltage.

Step 2: The battery rests for 30 minutes. This time lets the stored charges move from the storage well to the available well.

Step 3: The battery is discharged again with 1Crate until reaching the minimum voltage.

Step 4: Steps 2-3 are repeated until the battery delivers no charge.

SoC is computed with both Belvedere and proposed methods. The results are shown in Figure 2-6.

The charges move to the available well from the storage well in the resting phase; which leads in an increase of SoC. It is seen that the SoC computed by Belvedere method is lower than zero after t=7820s. Also, we can see that the SoC remains constant at zero current with this method. These problems arise because the SoC estimation method using (2.1) cannot account for the recovery and hysteresis effects. However, the proposed method can estimate the SoC accurately.

b) *Case of double-Layer supercapacitor*

Test IV and test V are performed using a 360F double-layer supercapacitor, 2.7V from Nesscap [70]. The results for charging and discharging are shown in Figure 2-7 and Figure 2-8.
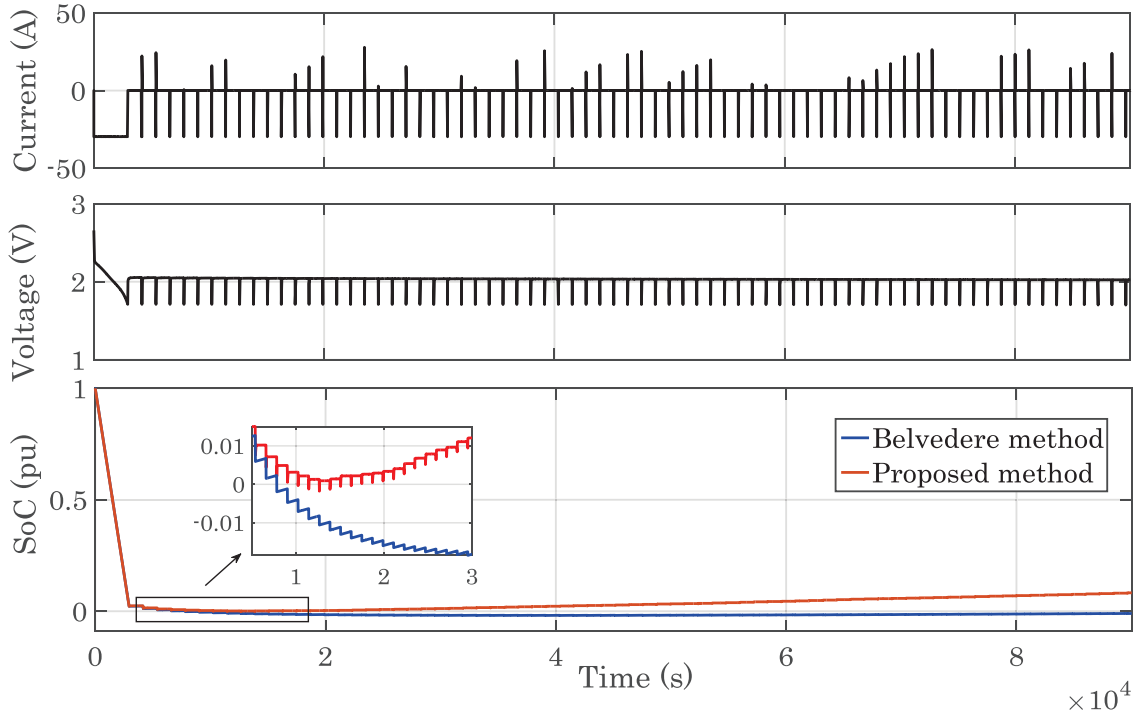
Figure 2-6 Discharge test for SoC validation for battery
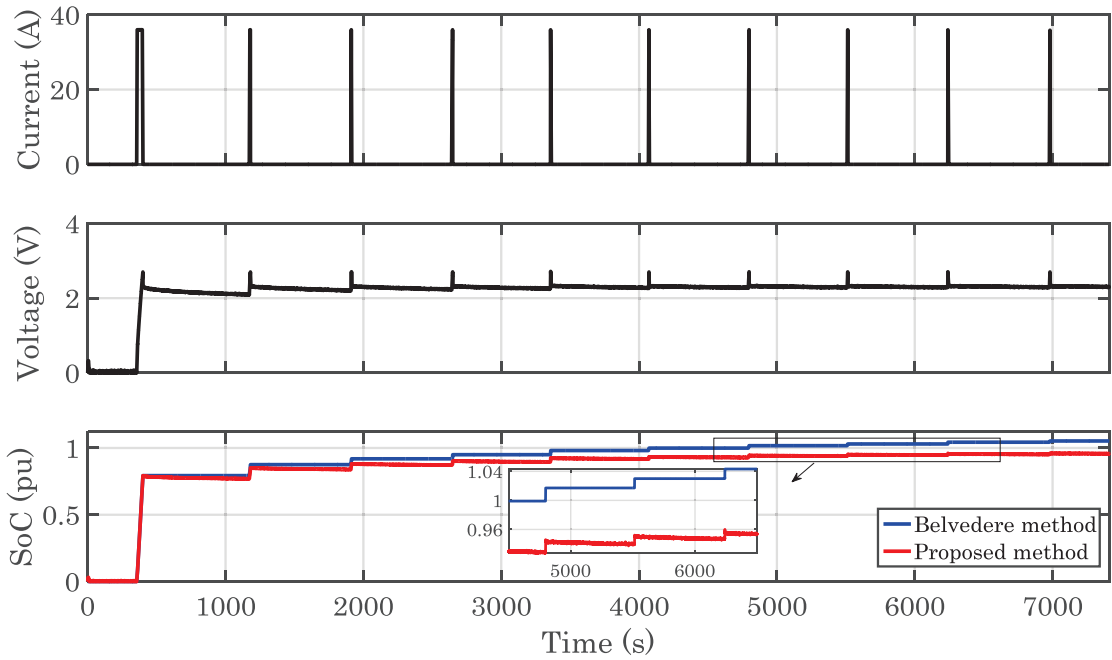
Figure 2-7 Charge test for SoC validation for supercapacitor
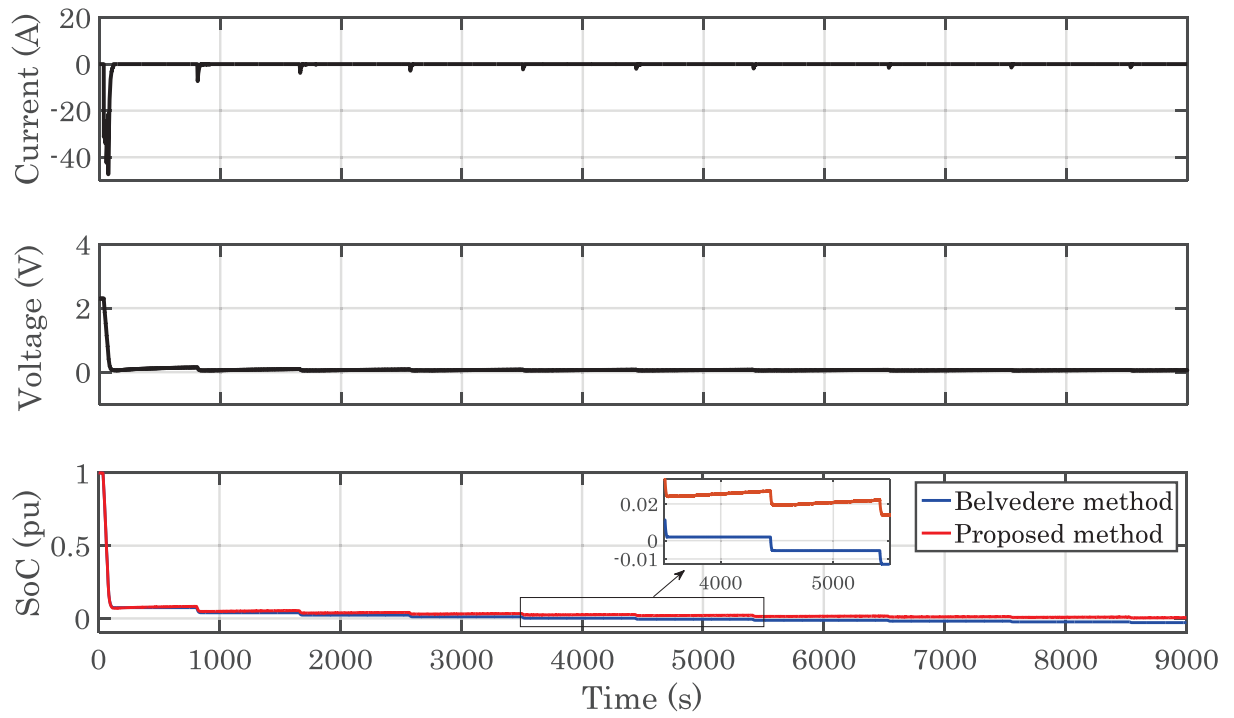
Figure 2-8 Discharge test for SoC validation for supercapacitor

Part II. Detailed Dynamic Modelling of Double Layer Supercapacitor

Double-layer Supercapacitors (DLSC), also called ultracapacitors, are characterized by high power density, short charging time, and long life duration. The basic principle of DLSC lies in capacitive properties of the interface between electrode and liquid ionic electrolyte. These properties were discovered by Helmholtz in 1853. Under the electrostatic influence of the applied voltage, positive and negative ionic charges within the electrolyte are accumulated at the surface of the solid electrode and formed electrical double layer which store the electric charge as shown in Figure 2-9. The thickness of this electric double-layer is limited to some nanometers depending on the concentration of the electrolyte and on the size of the ions. As a result, two properties are obtained for DLSC: First, huge capacitance can be obtained by using electrode materials with high specific surface areas [71]. Second, rated voltage is limited to some volts (by elementary cell), depending on the solvent and mainly due to the presence of impurities. As a result, the stored energy in DLSC depends on not only the specific surface area of electrode materials, but also the active materials in electrolyte.
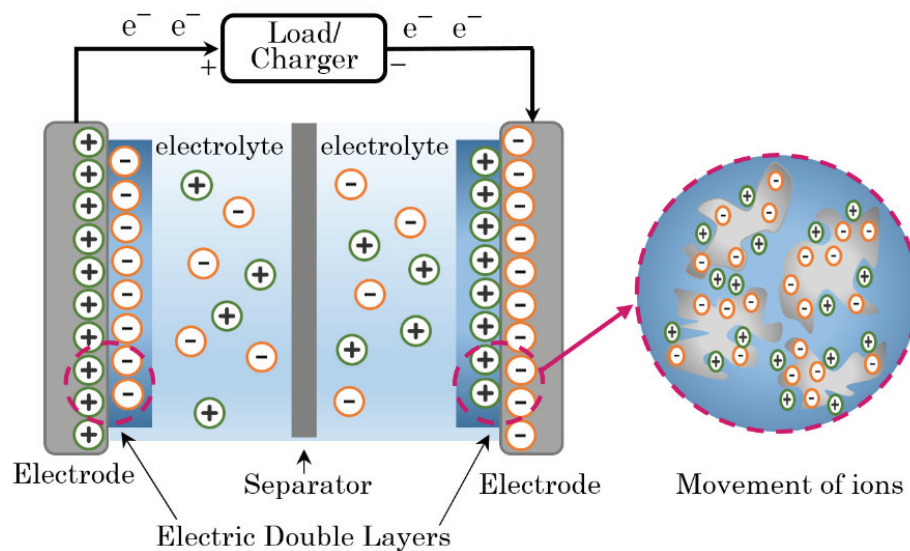
Figure 2-9 Structure of supercapacitor

2.2.1 Charge Redistribution Effects

De Levie [72] showed that the time constant for charging and discharging of DLSC is not the same, due to the heterogeneity characteristics of carbon pores of the electrode (shown in Figure 2-9). It can be considered that a pore consists of macro-, meso-, micro- parts depends on the depth of the pores. Thus, the outer part of the pores (macro-) gets charged/discharged more quickly than the inner ones (meso- and micro- respectively).

The effect of redistribution of charge in charging/discharging and relaxation phases are described below making reference to experimental tests carried out in DESL-EPFL Smart Grid Laboratory. The setup is shown in Figure 2-10.

Figure 2-10 DLSC experimental test setup

a) Experimental setup:

A DLSC 325F, 2.7V supercapacitor from Nesscap [70] is used for all experimental tests discussed in this thesis for DLSC. The DLSC voltage and current have been directly measured without any signal conditioning by using the following National Instruments A/D conversion cards: (i) C-series 9215 ±10 V, 16-bits voltage digitizer operating at the maximum sampling frequency of 100 kHz, (ii) C-series 9227 ±5 A, 24-bits current digitizer operating at the maximum sampling frequency of 50 kHz. All the experimental tests have been carried out into a dedicated climatic chamber at a constant temperature of 25 °C.

b) Effect of redistribution of charge in charging/discharging phases

In order to show this effect, a new fully-discharged DLSC is charged with 2A to reach its nominal voltage (2.7V). Then, it is discharged to reach 50mV. This charging/discharging procedure is repeated for 7 times. Figure 2-11 shows the time evolution of the charging voltage across the targeted DLSC. It is shown that reaching

an identical final voltage (starting from the same initial voltage), the more DLSC is cycled, the less time is needed.
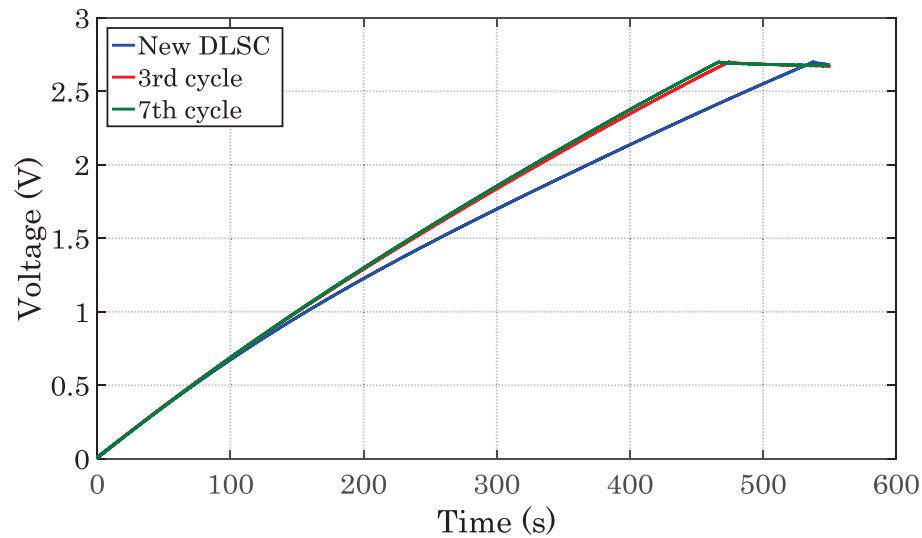
Figure 2-11 Time evolution of DLSC charging voltage with different number of cycles

This behavior also can be seen for discharging phases. The physical explanation of this behavior is based on redistribution of charge in the electrodes' pores. When a DLSC gets exposed to a current, the charges will first allocate in the macro-pores, then meso- and micro-pores respectively. The deeper the charge goes in a pore, the harder it extracts. As a consequence, there is always an amount of charges that remains stored inside the DLSC. This amount of remaining charge which cannot be easily extracted is called "redistribution charge" (Q_R). As seen, the presence of Q_R participates actively to the subsequent charging phases and reduces considerably the charging time needed to reach a certain voltage value in comparison with the time needed when the targeted DLSC was without any residual charge (new one). It is worth observing that after 7 cycles, there is no decreasing in charging time, since the meso- and micro- pores are saturated (for the targeted DLSC this happens after 7 complete cycles), and the Q_R reaches its maximum value. An illustration of the described process for 2 cycle of charging-discharging is shown in Figure 2-12 for a pore. The charge redistribution phenomenon is the process of homogenization of the charges in the pores of the DLSC electrode surfaces.

(a)

(b)   (c)

(d)   (e)
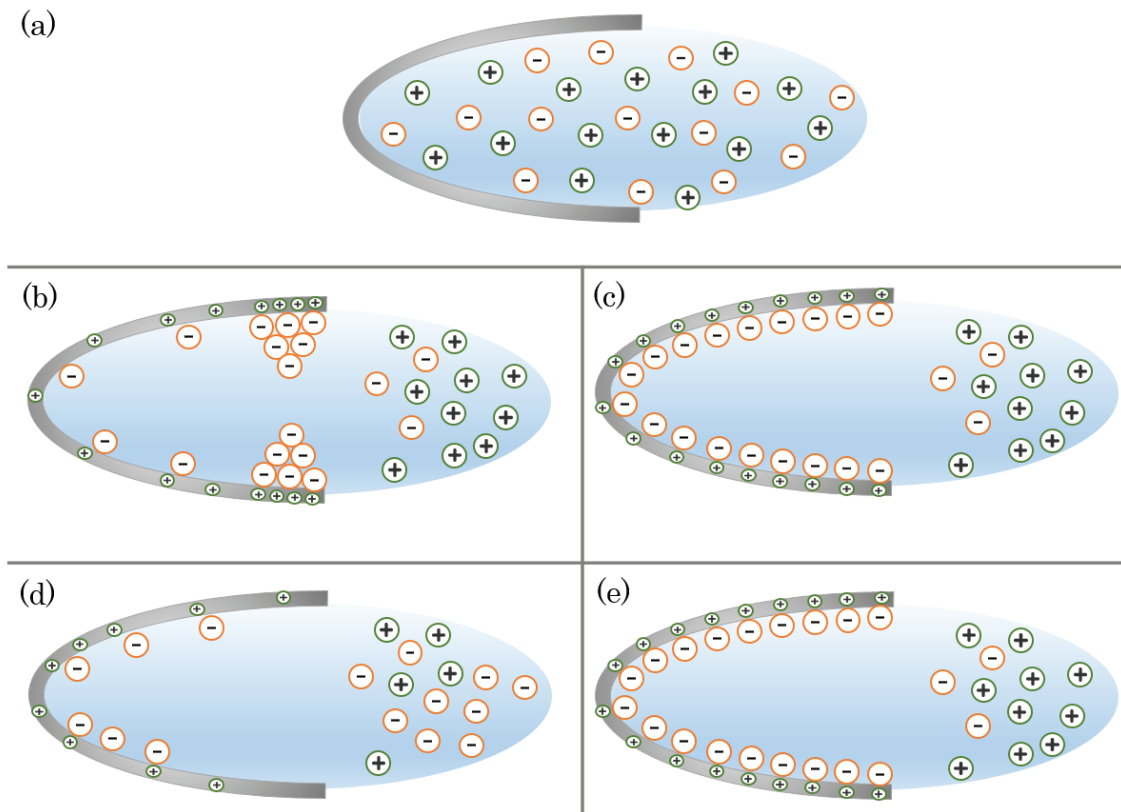
Figure 2-12 Schematic of ion distribution model in a pore for 2 cycle of charging-discharging

(a) Completely discharged: cations and anions are equally distributed. (b) Applying voltage: anions attract to the pore and cations repelled by the pore. There is accumulation of ions at pore opening. (c) Continue of charging: more cations move to the inner part of the pore (meso-, micro-pores). (d) Discharging process: cations are extracted from the pore (remains in the meso-, micro-pores). (e) Charging process: cations attract to the pore. Due to the residual charge, the charging time is decreased.

c) *Effect of redistribution of charge in relaxation phases*

From the beginning of the development of supercapacitors, it has been found that they have high self-discharge/charge rates. When the capacitor is left unconnected to either a charging circuit or an electrical load, the self-discharge/charge is occurred which refers to the gradual decrease/increase in the voltage across the capacitor.

When a DLSC is disconnected from the charging circuit, the accumulated charge in macro-pores are diffused into the electrolyte. Thus, it leads to a reduction of the number of charges in the electrode pores and, therefore, will produce a decrease of the open-circuit voltage [73]. The effect of residual charge also can be seen in the relaxation phases shown in Figure 2-13. It is seen that the higher Q_R (more cycled)

leads to higher open circuit voltage (V_{oc}). It is clear that after each charging phase the amount of Q_R increases.
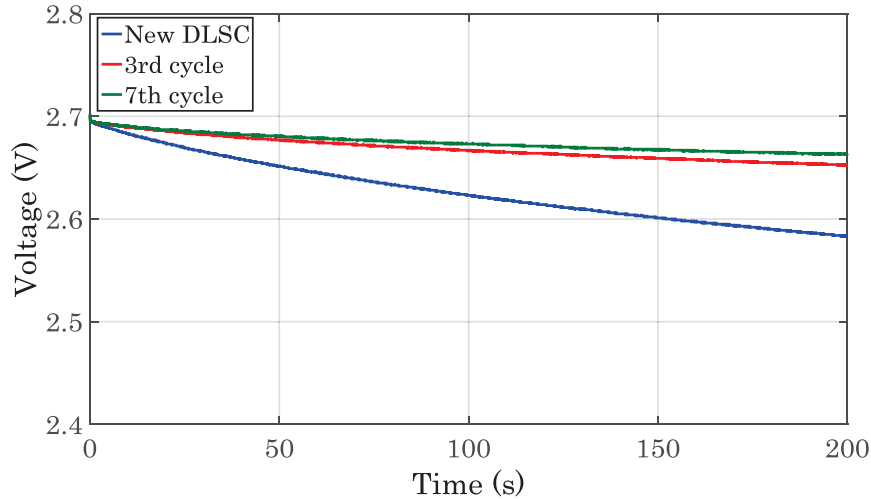
Figure 2-13 Time evolution of DLSC open circuit voltage with different number of cycles

When a DLSC is disconnected from the discharging circuit (load), the stored charge in the meso-, micro-pores come to the macro-pores and consequently the voltage across the DLSC is increased. As a result, the system reacts quite differently in case of discharging in comparison to the charging due to the charge history of the device. This difference can be seen in Figure 2-14. The DLSC with 2.7V initial voltage is discharged to 2.4V. The result is compared to the DLSC with 2.1V initial voltage which is charged to 2.4V. After charging, one can observe a voltage decay. Conversely, discharging yields to the increase in the open circuit voltage. The physical explanation of the charge history phenomenon is shown in Figure 2-15.
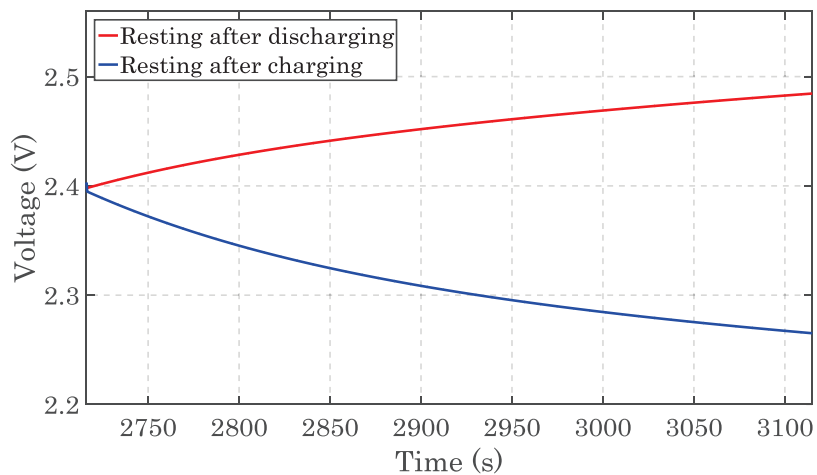
Figure 2-14 Open circuit voltage after charging and discharging with the same voltage
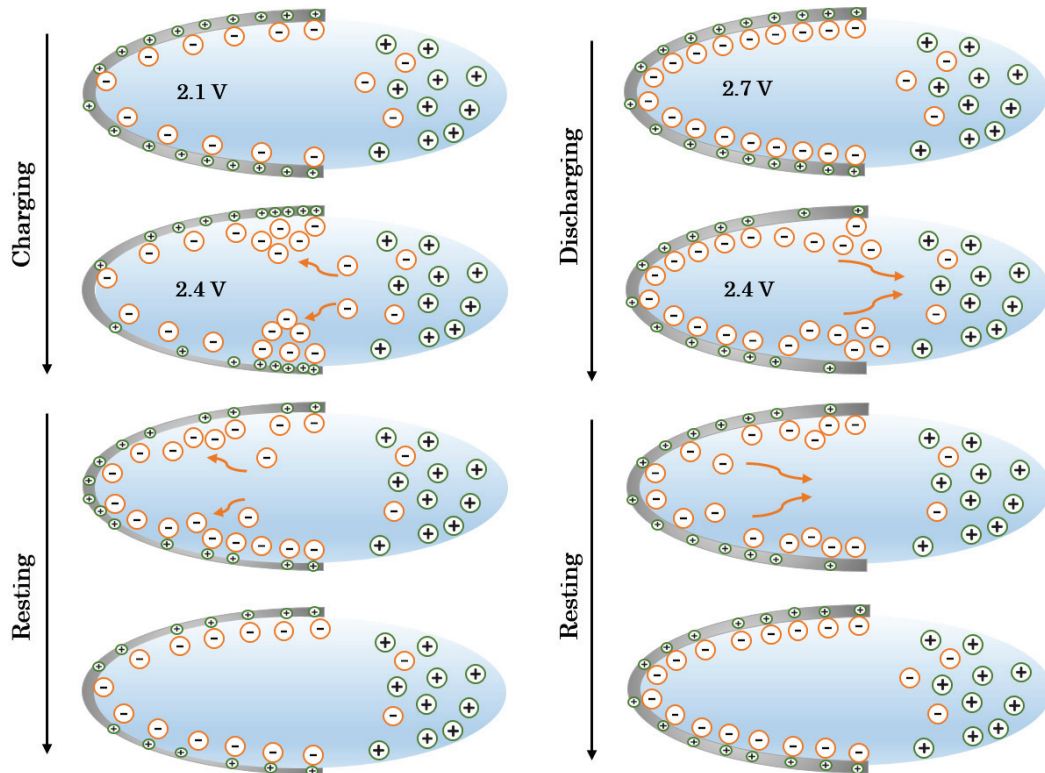
Figure 2-15 Schematic of ion distribution model showing charge history effect

Another experiment is carried out in order to show the effect of voltage level on redistribution of charge pattern. For this purpose, the DLSC is charged to reach to different voltage values (i.e., 2.7 V, 2.4 V, 0.7 V). The time-evolution of the so-called decay voltage across the DLSC is shown in Figure 2-16.
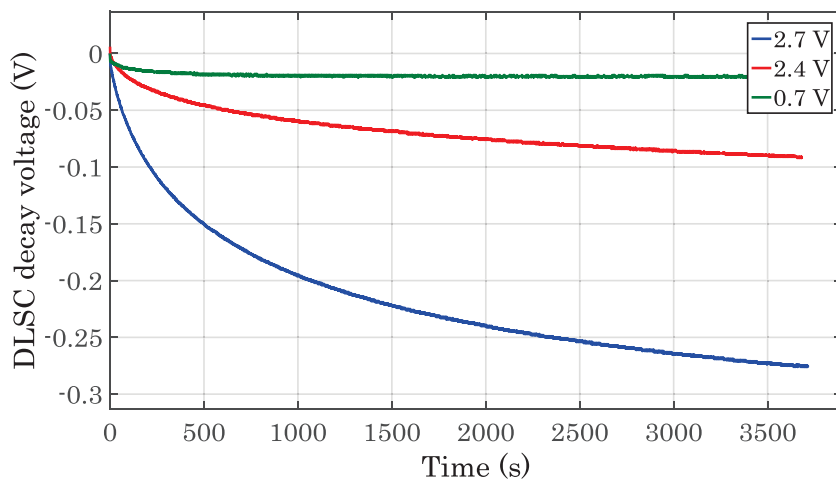
Figure 2-16 Time evolution of open circuit voltage showing the effect of voltage levels

It should be reminded that the charges participating to the redistribution phenomena are those already stored inside the targeted DLSC, (Q_R), plus some other charges injected by the power source to the DLSC during the charging phase. Therefore, the total quantity of charge is less in case of lower final charge voltage. The gradient charge is lower as well which leads to the lower voltage drop. It is well known that the redistribution phenomenon is caused by the irregularity of the DLSC electrodes porous carbon structure involving a gradient of ion concentration within the DLSC electrolyte. This gradient depends on the different time constants of the macro, meso and micro pores of the electrodes-electrolyte interface [74]. This means that during the charging phase, the early-time charges migrate easily toward the macro-pore and then, during the relaxation phase, toward the other smaller pores.

2.2.2 Review of Existing DLSC Modelling Methods

Since the early nineties new supercapacitors dedicated to high power applications have been produced. Some reported works used simplistic models to explain their behavior [2], [3]. However, The DLSCs behavior is not ideal, and they exhibit nonlinear characteristics such as voltage recovery, which occur over very long periods. Many researchers endeavor to model the DLSC considering for their nonlinear behavior. In general, the DLSC models can be grouped in three main categories: dissipation transmission line model, empirical model and analytical model.

1) Dissipation transmission line model

In 1963, de Levie [72] first treated the capacitance in porous electrodes as a dissipative transmission line. The model treats each pore as a dissipative transmission line. It includes a distributed double layer capacitance and distributed electrolyte resistance that extends into the depth of the pore. In 1999, Conway et al. [75] developed an equivalent circuit model based on de Levie transmission line model. The macro-, meso-, and micro-pores are taken into account in this model. A basic outline of the model can be seen in Figure 2-17.
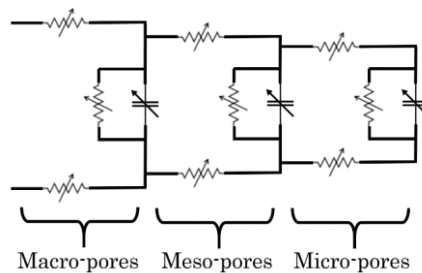
Figure 2-17. DLSC Conway transmission line model

Buller et al. [76] in 2002 proposed a DLSC model transformed from De Levie's porous electrode model. Impedance spectroscopy is used to identify the parameters. However, Buller's model excludes the self-discharge phenomenon that affects the static and dynamic characteristics of DLSCs and it is only interested in very short-term behaviors. Kaus et al. [74] in 2010 established a complex electrical model for DLSC in order to account for the effect of the charge redistribution during self-discharge and it was capable of predicting the effects of charge duration, initial voltage, and temperature on the open circuit voltage decay. The inconvenience of this model is the complex determination of the different elements. Also, a long simulation time is required which bounds to the RC branch numbers. Although the DLSC dissipation transmission line model provides a good intuition of the internal dynamics of the electrochemical capacitors, it is mainly used for understanding the behavior of the device with specific aims such as improving the synthesis of the electrode [77], studying the self-discharging behavior [78], and predicting the surface impedance of the electrode. No DLSC model has been developed to characterize the device as a whole based on a dissipative transmission line model.

2) Empirical model

The empirical model is a gray-box model referring to an electrical RC equivalent circuit model. The main advantage of the empirical model comes from their relatively simple equivalent circuit representations which allow the users to easily incorporate the model into their system simulations. It also provides a good estimation on DLSCs steady state and transient responses. DLSC parameters identification is obtained by experimental measurements. However, considering the physical phenomena in the double layer interface, the supercapacitor cannot be represented by a simple RC circuit.

Miller et al. in 1993 [79] showed that the DLSC could be well represented by 5-branch RC model shown in Figure 2-18. However, finding the parameters of this model is challenging and it is not suitable for online applications due to the high complexity.
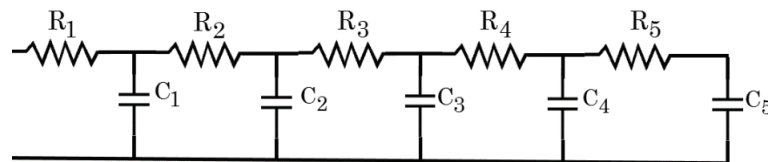
Figure 2-18 DLSC Miller empirical model

In 2000, Zubieta et al. [80] decreased the number of RC branches of Miller model to three. Since it is empirical model, it does not capture the underlying physics, but the equivalent circuit was developed intuitively to match the nonlinear variations of the terminal voltage as a function of time. It proposed a characterization process that

allowed the supercapacitor parameters to be determined automatically. The first branch is an immediate branch with a time constant in the order of a few seconds. The second branch is a delayed branch with a time constant in the range of minutes. And the third branch is a long term branch with a time constant larger than ten minutes.

The main limitation of this model is that they do not take into account for the residual charge. Such a limitation has an influence on the assessment of DLSC parameters as well as on the model applicability. Thus, it cannot capture the electrical behavior over a period of several hours or days and has no means of dealing with temperature dependency effects. Also, a critical simplifying assumption is made that each branch operates independently from the others (e.g., while the immediate branch is charging, there is no interaction with the delayed or long branches).

Belhachemi et al. [81] improved the Zubieta's model by combination of 2-branch Zubieta's model and dissipation transmission line model. The model is shown in Figure 2-19. However, this model cannot account for the long-term redistribution of charge. Rafik et al [82] in 2007 made some improvements based on Zubieta's model in order to obtain better agreement between simulations and experiments for the long term behavior as well as to account for temperature effects. The model is depicted in Figure 2-20.
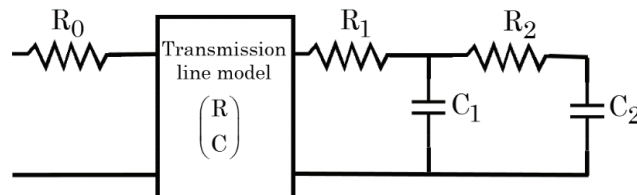
Figure 2-19 DLSC Belhachemi empirical model

This model takes into account the temperature, voltage and the frequency behavior. Circuit 1 is introduced to account for the temperature dependence. Circuit 2 is introduced to increase the precision of the model over a 1 to 10 Hz frequency range. Circuit 3 is a slight modification of the Zubieta model, where leakage current and the internal charge distribution are accounted for. The parameters of the model are identified by EIS. However, this model is not easy to implement due to the high complexity and computation time.

In 2011 Kim et al. [83] modeled the porous of electrodes using equivalent RC circuit. EIS is used to acquire parameters depending on voltage. The self-discharge is modeled as a single resistance which is a great simplification since the redistribution of charge has exponential behavior. Weddell et al. [84] tried to improve the 3-branch RC Zubieta's model by taking into account the interaction between branches during

rapid charging/discharging process. However, this model is difficult to implement on online application with limited computing resources. Musolino et al. [85] in 2013 presents a full-frequency range 6-branch model for DLSCs. A simple procedure is used to identify parameters. It is shown that this model is the most accurate one in order to take into account for self-discharging. However, it would increase the complexity and computation burden. Also, the accuracy of the proposed model for dynamic cycles with long charging/discharging and redistribution phases has not been illustrated.
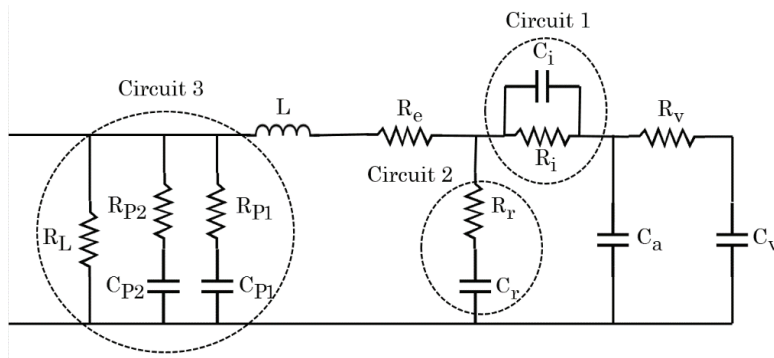
Figure 2-20 DLSC Rafik empirical model

To sum up, the limitation of existence empirical model is that they are not developed on the basis of the physics of the device. As a matter of fact, they cannot accurately replicate the DLSC voltage behavior and energy efficiency during high-dynamic current profiles and longer time intervals where the stored residual charge in the devices can play a key role and the internally generated heat changes the electrical performance of the device.

3) *Analytical model (white)*

It is a white-box model (e.g., [86], [87], [88], [89]–[93]) developed on the basis of the electrochemical capacitor's underlying physics. The electrochemical reactions are most commonly described using the Butler-Volmer equation, where the physicochemical parameters in the equation are often assumed to best fit the experimental results. The key advantage of the analytical models is its ability to accurately predict the electrical behavior of the electrochemical capacitors. In addition, this method is flexible in a sense where one can add or modify the governing equations or the parameters to analyze the impact of the change on the overall device behavior. However, this model cannot be used to predict the aging process or to couple the thermal effects. It is also difficult to use it in the electrical simulations.

2.2.3 Proposed DLSC Empirical Model

The proposed model in this thesis is based on Belhachemi model shown in Figure 2-19. The proposed model is shown in Figure 2-21. Where R_0 is the DLSC input electrode resistance; R_L and C_V are the resistance and the nonlinear capacitance of the DLSC transmission line model; R_1 and C_1 are the resistance and the nonlinear capacitance of the first branch, R_2 and C_2 are the resistance and the nonlinear capacitance of the second branch. The use of multiple branches enables the long-term charging process to be modeled, which is dependent on the physical distribution of charge within the electrode.
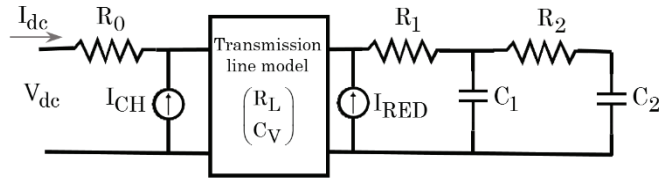
Figure 2-21 DLSC proposed model

The two virtual current sources, I_{CH} and I_{RED}, are considered to improve the diffusion of the residual charge during charge/discharge and resting phases.

a) Optimal assessment of the parameters

Making reference to the model shown in Figure 2-21, the terminal voltage $V_{dc}(t)$ can be represented as a function of the current and the relevant parameters, as follows:

$$V_{dc}(t) = f_1\left[I_{dc}(t), R_L, C_V\right] + f_2\left[I_{dc}(t), R_1, C_1\right] + f_3\left[I_{dc}(t), R_2, C_2\right] \tag{2.8}$$

As mentioned C_1, C_2 and C_V are nonlinear and they depend on the $V_{dc}(t)$. But the resistances are constant. The evaluation of the parameters of (2.8) has been performed by following experimental procedure:

- Test I. Identify the DLSC parameters

Step 1: The acceptable range of V_{dc} has been divided into a certain number of intervals (in our case 10) between zero and the rated voltage $\left\{V_{dc,1}^F, V_{dc,2}^F, ..., V_{dc,n}^F\right\}$.

Step 2: A fully discharged DLSC is charged with nominal constant current (1Crate).

Step 3: The supply generator is turned off and the DLSC rests about 1 hour in order to reach equilibrium.

Step 4: It is discharged completely.

The terminal voltage, in the first time-step (t_0) is mainly determined by the voltage drop at R_0. So, R_0 can be evaluated by (2.9)

$$R_0 = \frac{V_{dc}(t_0)}{I_{dc}(t_0)} \tag{2.9}$$

For each of the intervals $V_{dc,i}^F$ the following optimization problem using least square technique is solved to minimize the difference between the measured terminal voltage $(V_{dc,i}^m)$ and the simulated one.

$$\underset{\substack{R_L,C_V,C_1,\\C_2,R_1,R_2}}{arg\ min}\{V_{dc,i}^m - V_{dc,i}^{sim}\}^2$$

$$V_{dc,i}^{sim} = f_{1,i}\left[I_{dc,i},R_{L,i},C_{V,i}\right] + f_{2,i}\left[I_{dc,i},R_{1,i},C_{1,i}\right] + f_{3,i}\left[I_{dc,i},R_{2,i},C_{2,i}\right] \tag{2.10}$$

I_{CH} and I_{RED} are used to model the effect of residual charge (Q_R). In charging/discharging phases only I_{CH} is active while in case of resting phases only I_{RED} is active. Q_R is redistributed based on the time constant of the branches. As a result, the value of I_{CH} and I_{RED} are computed using the following empirical equations.

$$\begin{cases} I_{CH}(t) = \frac{Q_R}{\tau}e^{-\frac{t}{\tau}} \\ I_{RED}(t) = \left(\eta_1\frac{Q_R}{\tau_1}e^{-\frac{t}{\tau_1}} + \eta_2\frac{Q_R}{\tau_2}e^{-\frac{t}{\tau_2}}\right) \end{cases} \tag{2.11}$$

Where τ, τ_1 and τ_2 are the time constant of transmission Line model, first and second branches respectively. It should be noted that the first branch is associated to the macro-, meso-pores and the second branch is associated to the micro-pores. η_1 and η_2 define the share of each time constant and are obtained experimentally.

In order to compute Q_R, we need to find the relation between the terminal voltage of DLSC (the only parameter that is measurable) and the stored charge (ΔQ). Thus, the whole charge extracted in the discharging phase (ΔQ) is computed for each $V_{dc,i}^F$. Therefore, a lookup table is obtained showing the relation between ΔQ and V_{dc}^F. The $V_{dc}^F - \Delta Q$ relationship is shown in Figure 2-22.
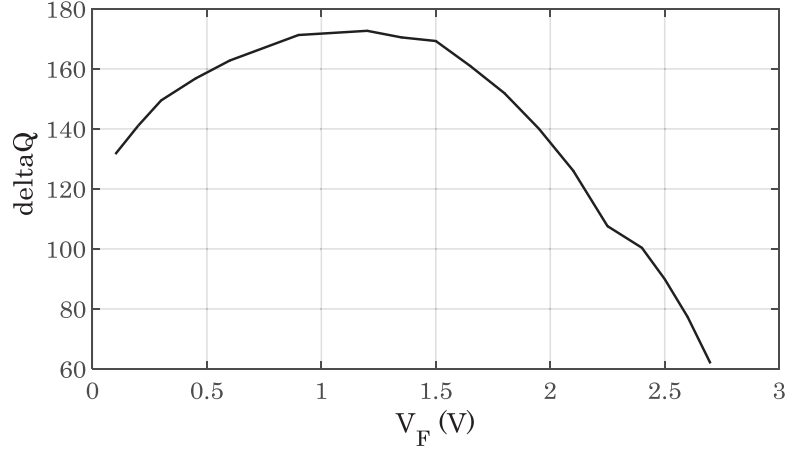
Figure 2-22 Extracted charge for different DC final voltage

At a given time t^* with DLSC voltage $V_{dc}^F(t^*)$, ΔQ is obtained using $V_{dc}^F - \Delta Q$ curve. As a result, Q_R is computed using (2.12)

$$Q_R = \Delta Q - \int_0^{t^*} I_{dc}(t) dt \tag{2.12}$$

2.2.4 Experimental Validations

To characterize the targeted DLSC, the described tests for finding the parameters has been carried out. The results are shown in Table 1 and Table 2. In order to validate the model, five sets of tests are performed. The proposed model is compared with Belhachemi [81] model with optimized parameters and the measured results. The first test is corresponding to a charge/discharge cycle with nominal current (1Crate). It is shown in Figure 2-23. The same test is carried out with 0.75Crate and 1.15Crate, in order to better underline the improvement provided by the proposed model with different amount of current. The results are shown in Figure 2-24 and Figure 2-25.

Table 1: 325F DLSC constant parameters

R_1	$2.5\ m\Omega$
R_L	$3.7\ m\Omega$
R_2	$2.3\ \Omega$
R_3	$18.71\ \Omega$
η_2	0.3
η_3	0.7

Table 2: 325F DLSC nonlinear capacitance values

Range voltage value	Transmission line model nonlinear capacitance values (F)	first nonlinear capacitance values (F)	Second nonlinear capacitance values (F)
0-0.3	278.1	54.3	16.9
0.3-0.6	281.3	54.4	16.9
0.6-0.9	288.2	54.9	17.1
0.9-1.2	297	56.3	17.5
1.2-1.5	307	58	18
1.5-1.8	318	60.1	18.7
1.8-2.1	329	62.1	19.3
2.1-2.4	337	64.2	20
2.4-2.7	348	65.8	21.2
Over 2.7	349	68	21.1
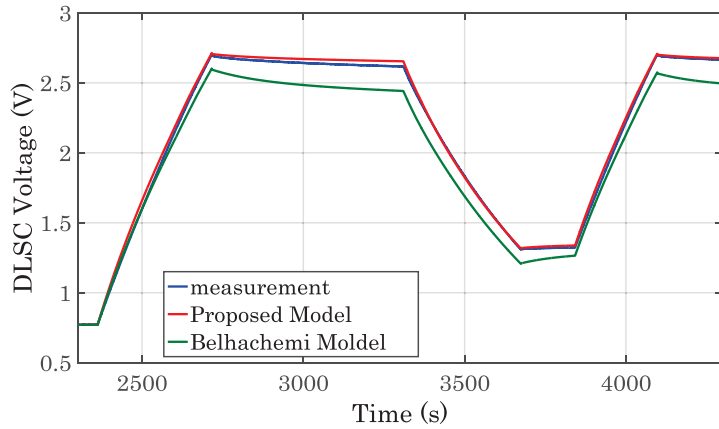
Figure 2-23 DLSC voltage comparison between the proposed model, Belhachemi model and measurement (2A)
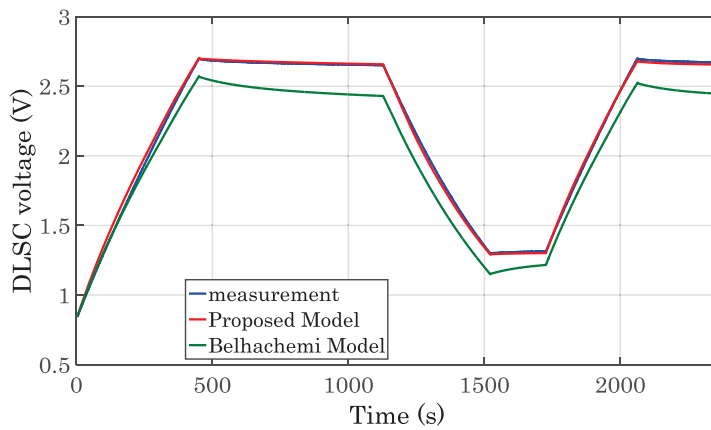
Figure 2-24 DLSC voltage comparison between the proposed model, Belhachemi model and measurement (1.5A)
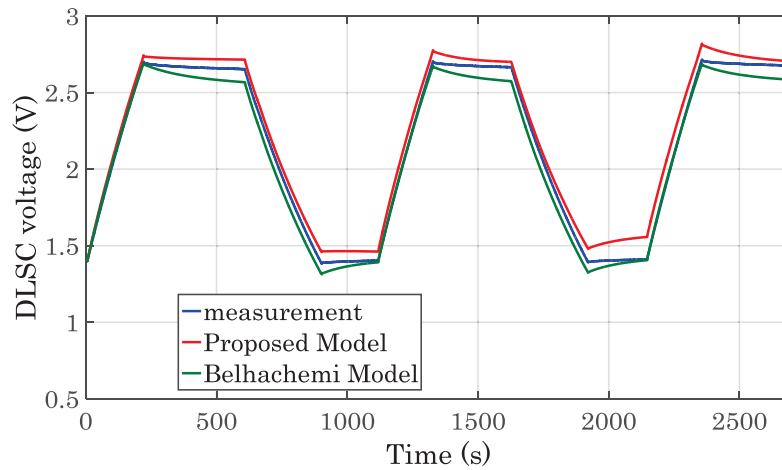
Figure 2-25 DLSC voltage comparison between the proposed model, Belhachemi model and measurement (2.3A)

As it is seen from the above three tests, the error between the measured voltage and the simulated one is extremely low. In particular, a mean squared error in the order of 10^{-4} has been monitored for the proposed model and a corresponding value of 10^{-1} for the Belhachemi model.

Figure 2-26 shows the comparison for a cycle characterized by a deep discharging phase that represents a challenge for all the previous DLSC models. For this cycle the mean square error for the proposed model and Belhachemi model are 0.2% and 15%, respectively.
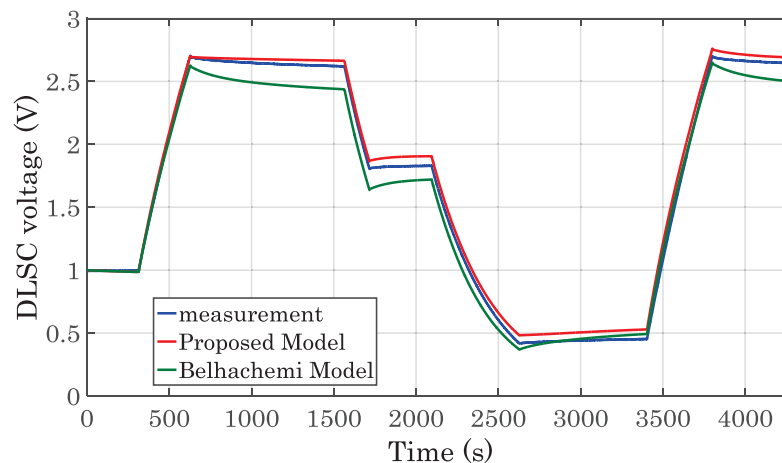
Figure 2-26 DLSC voltage comparison between the proposed model, Belhachemi model and measurement (2A) in case of deep discharging phase

Finally, Figure 2-27 illustrates the comparison for a DLSC cycle with two short charging phases and two short discharging phases followed by a long rest phase. We can observe that the presented model is able to follow the right value with higher precision even if the redistribution of charges does not take place.
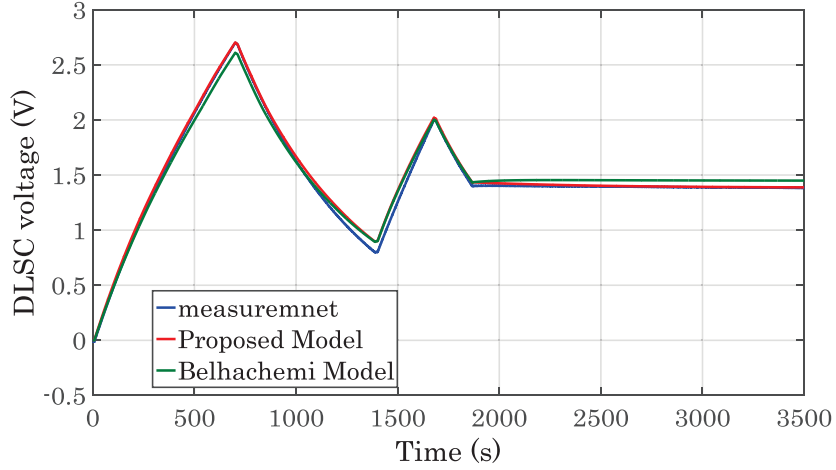
Figure 2-27 DLSC voltage comparison between the proposed model, Belhachemi model and measurement (2A)

It should be noted that, I_{CH} and I_{RED} do not violate the charge balance of the DLSC since they are not injecting an external current; but they model the movement of the charges already stored in the electrolyte. The time integral of currents provided by the two virtual generators has been verified to not to be higher than ΔQ.

Part III. Detailed Dynamic Modelling of Electrochemical Battery

Battery Energy Storage Systems (BESSs) are characterized by relative high value of energy density [94]. The basic principle of BESS lies in the chemical kinetic process inside the battery. This property is introduced by Manwell in 1993 [20]. He considered that in the cell electrolyte there are several layers (as shown in Figure 2-28 for lithium-based batteries) where the charges are passing through.
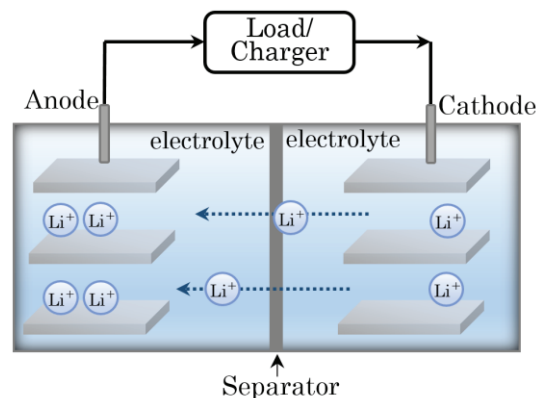
Figure 2-28 Multiple layer structure of the lithium-based battery electrolyte

In particular, the charges are directly delivered toward the load through the surface layers whilst the inner layers are storage reservoirs supplying charges to the surface layers. The charges exchanged between these layers are the major responsible of the nonlinear behavior of the BESSs. This general model is equivalent to the genetic CR model with 2 wells shown in Figure 2-2. In this respect, the effect of redistribution of charge on BESS is described in section 2.3.2.1 making reference to experimental tests carried out in DESL-EPFL Smart Grid Laboratory.

Experimental Setup:

In what follows we make reference to a Lithium-Titanate cell (LTO) characterized by a 30 Ah rated capacity and a nominal cell voltage of 2.3 V. The setup is shown in Figure 2-29. The charging system is controlled by a power supply EA-PS 8080-120. The device allows charging with a completely programmable input voltage and current profile, and it is fully remote controlled. The discharging system is controlled by Electronic load EA-EL 9080-200. The device allows for discharging the cell under test in several modes such as constant current, constant voltage, and constant power modes. It is also fully remote controlled. The battery voltage and current are directly measured using a 16-bits National Instrument, A/D 9215 conversion cards coupled with voltage and current sensor

Figure 2-29 Battery experimental test setup

2.3.1 Charge Redistribution Effects

The rate capacity effect takes place within the BESS like all the other electrochemical BESSs [29], [95]. This phenomenon is shown in Figure 2-30.
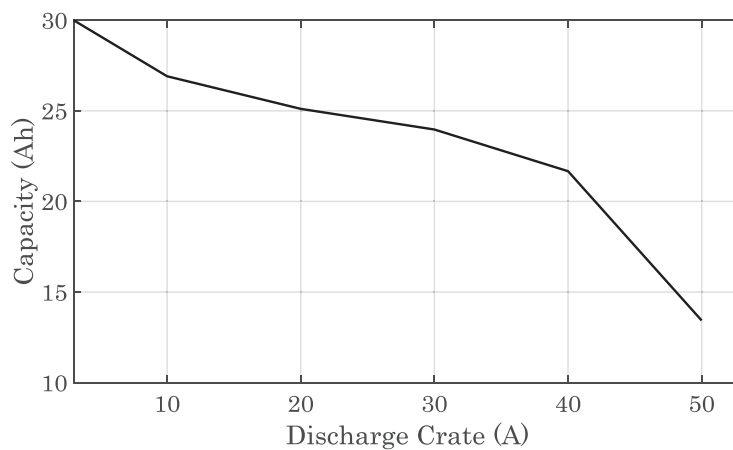
Figure 2-30 LTO cell capacity as a function of different constant current discharge rates

As shown in Figure 2-28, there are several layers in the electrolyte where charges are passing through. For the sake of simplicity, we can assume that there are two main layers inside the electrolyte as shown in Figure 2-31. In particular, the charges are directly delivered toward the load through the surface layer. The inner layer is a storage one that supplies charges only to the surface layer. It is possible to assume that the SoC represents the amount of the available charges in the surface layer. This is similar to what was shown in Figure 2-2.
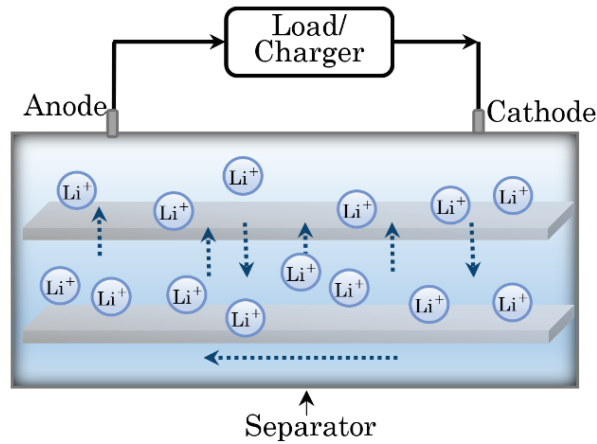
Figure 2-31 BESS structure with two layers

From Figure 2-32, it can be seen that, when the cell current flow is stopped, the recovery effect take place and consequently, the terminal voltage of the BESS increases (for 300s < t < 900s). The amount of charge being available on the surface layer depends on several quantities such as temperature, viscosity and electric conductivity of the electrolyte. The variation of these quantities, along with the extracted current, is nonlinear.
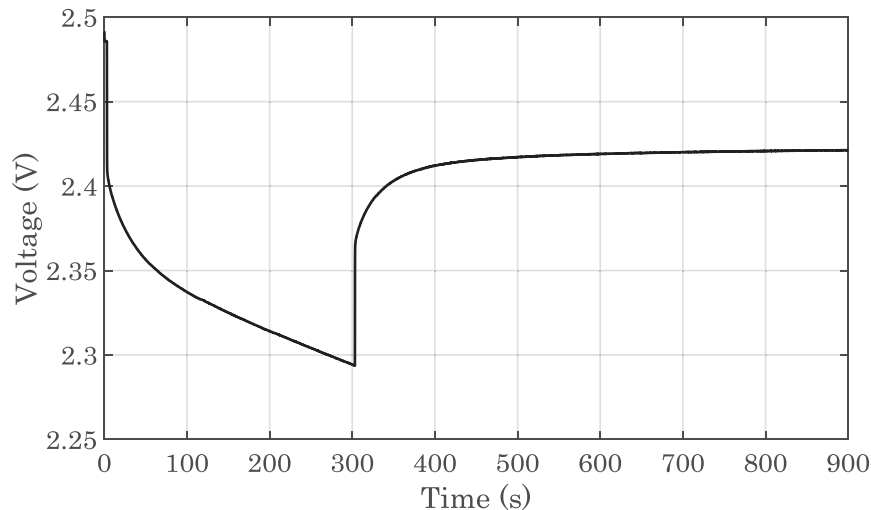
Figure 2-32 Recovery effect visible on the LTO cell voltage

When a load is connected to the battery, the surface charge will be reduced rapidly and the inner charge will remain inside the battery. When the load is removed, charge would flow from the inner layer to the surface layer to reach an equilibrium. Consequently, the battery open circuit voltage, V_{oc}, would increase and more charge would be available to the load compared to the case where the battery is continuously connected to the load (in this case the surface charge will drop to zero). Based on the

above physical considerations, it is possible to assume that the charges of the inner layers play a key role during the redistribution phases.

In order to illustrate the recovering and the rate capacity effects in BESS, Figure 2-33 illustrates the time evolution of the targeted battery cell voltage with 0.6Crate, 1Crate, and 1.5Crate at 25°C. As it can be observed, when the cell current flow is stopped, the redistribution and the associated recovery effect take place and the terminal voltage increases. Also, the rate capacity effect can be clearly seen in the discharging phases (i.e., when the discharging rate decreases, the battery has more potential to reach the equilibrium). Indeed, discharging the battery with higher currents, leads to the larger amount of charges that can be recovered.
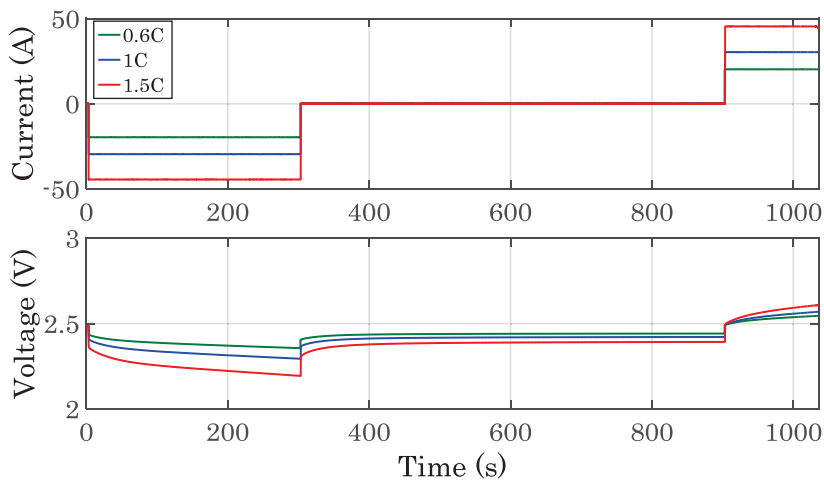
Figure 2-33 Time evolution of the targeted LTO voltage with different Crates at 25°C

The two described effects are also largely influenced by the temperature. In this respect, Figure 2-34 and Figure 2-35 illustrate the time evolution of the battery cell voltage at different temperatures for the case of discharging and charging phases, respectively. It is possible to observe that, in the discharging phases, with the same discharging current, the voltage of the battery operated at lower temperatures may reach a lower value in comparison with the same BESS operated at higher temperatures. For charging phases, in order to reach the same final voltage for the cell operated at different temperatures, a longer time is needed at higher temperatures compared with the rated one. At low temperature, the surface kinetic potential loss becomes important due to several process such as precipitation, dissolution, desorption and adsorption that affect the reaction kinetics. However, the open circuit voltage values are the same for all the cells operated at any temperatures (charging and discharging phases). This can be supported by the fact that at higher temperatures, the charge flow rate from the inner toward the surface layer (or vice versa) increases. The equilibrium voltages reached after the recovering

phase (namely V_{oc}) seems to be independent from the temperature. It seems that the only effect of temperature on the redistribution phase is related to the speed of the internal diffusion phenomena [96].
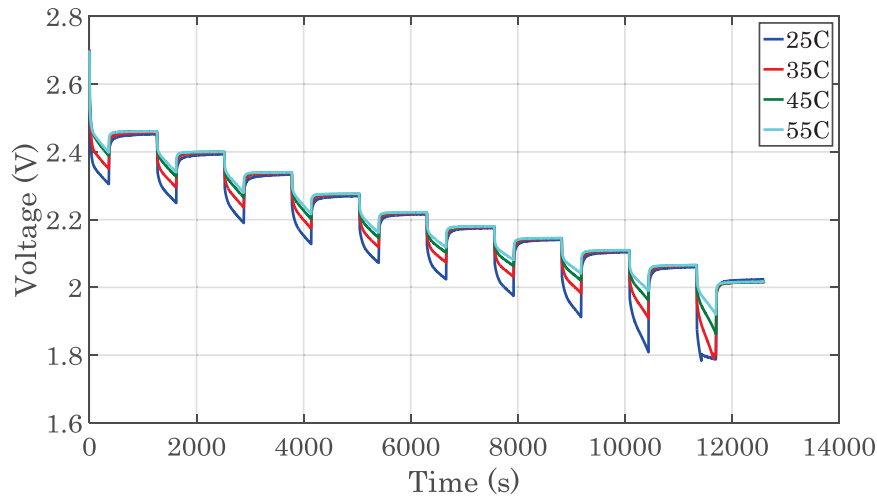
Figure 2-34 Time evolution of the targeted LTO voltage at 1C discharge rate at different ambient temperatures during sub-sequent discharging phases

Moreover, since batteries are normally operated in environments where the temperature could be far from the nominal one, the BESS model needs to be robust, with respect to the variations of this quantity, in terms of voltage prediction. Therefore, having an accurate model of BESS accounting for internal dynamics and charge redistribution effects is of utmost importance.
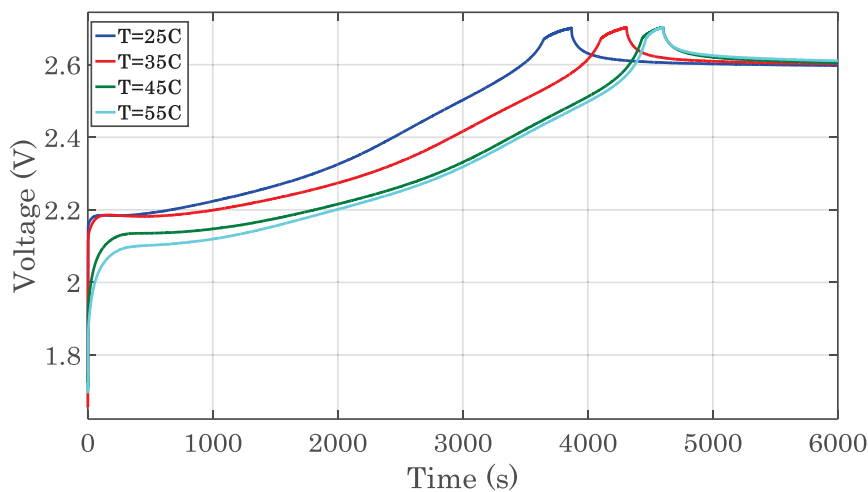
Figure 2-35 Time evolution of the targeted LTO voltage at 1C discharge rate at different ambient temperatures during charging phase

2.3.2 Review of Existing Battery Modelling Methods

The study of the literature concerning BESS modeling allows to identify three main categories of models, namely: analytical model, kinetic battery model and empirical model.

1) Analytical model

The analytical model (Also called electrochemical model) (e.g.,[97], [98], [63]) is a white-box model based on complex nonlinear differential equations aiming at describing the electrochemical processes taking place within the battery cell (in particular, on the electrolyte/electrodes interface). The electrochemical modeling described by Newman [99] in 1991 has been applied to the batteries (e.g., [100]-[64]). Doyle et al. [96], [101], [102] in 1993-1994 developed an electrochemical model for lithium-based batteries. This model consists of six coupled, nonlinear differential equations. Solving these equations gives the voltage and current of the battery as a function of time. The analytical model is the most accurate model; however, it calls for a highly detailed description of the battery chemical processes, expensive instrumentation for analyzing the microspore structure of electrolyte and electrodes, and high computational resources. From this standpoint, it seems difficult to use this type of model for real-time battery power management systems and circuit simulation.

2) Kinetic Battery Model (KiBaM)

The second category of models is named Kinetic Battery Model (KiBaM) introduced by Manwell et al. [20], [103] in 1993-1994. KiBaM is a very intuitive model using a chemical kinetic process as its basis. It is simplified electrochemical models that can capture nonlinear capacity effects and predict runtime of the batteries with reduced order of equations. However, this model cannot describe the electrical dynamic (i.e., current and voltage time evolution) that are important for electrical circuit simulation and multi-cell battery design. It also requires internal information on the material properties; which is not easy to be evaluated and it could result in computation time increase.

3) Empirical model

It is a gray-box model aiming at abstracting the physical phenomena taking place inside the battery cell by using the combination of voltage and current sources, capacitors and resistors. In this model, the parameters of the equivalent RC model are obtained by experimental tests. However, these identified parameters have little reflect to the real physical parameters of the battery. There are two main methods of creating these dynamic models. Using experimentally obtained data to create lookup tables which are referenced by the simulation, or using experimentally obtained data to create nonlinear equations which represent how the battery

parameters change during operation. The first battery electrical circuit model was proposed by Zimmerman et al at 1978 [104] for Nickel-Cadmium battery cell. In 1982, an electrical model of battery based on Thévenin circuit was proposed by Appelbaum et al [105] for lead-acid batteries. This model was not accurate since the model parameters were considered constant. In 1992, an electrical model was proposed in [106] allowing a continuous evaluation of battery performance using Two Time Constant (TTC) Thévenin equivalent circuit.

Hageman [107] in 1993 used a simple PSpice circuits. In 1995, Baudry et al [108] proposed a dynamic model of a battery that contains one RC branch, with linear behavior. However, the actual behavior of the battery is found to be significantly nonlinear. Glass et al [109] in 1996 and Gold [110] in 1997 proposed a similar model as [107] for lithium-based batteries. In both models a capacitor and a resistor are used to represent the capacity of the battery and battery resistance respectively. A voltage against SoC lookup-table is also used to determine the initial state of the battery. Although this model is simple, it needs significant effort to configure it. Furthermore, it is not so accurate in predicting the battery behavior and it has errors up to 12% [110]. In 2000, Ceraolo [111] proposed a dynamic model for lead-acid batteries using electrical circuit. This model is complicated by the fact that the proposed equations contain several parameters that have to be identified. In 2004, [112] used the same model and a rapid test was proposed to derive the model parameters. However, this model does not completely account for battery nonlinear capacity behaviors. This involves an inaccurate prediction of the remaining battery capacity and, consequently, an inaccurate voltage-current time evolutions predictions. Chen et al. [113] in 2006 tried to improve the TTC model considering the runtime prediction and SoC tracking. The model parameters were extracted using experimental data. However, this model is also unable to capture nonlinear capacity behavior of the battery since a constant capacity is considered to represent the remaining usable capacity of the battery. Zhang et al. [114] improved this model to capture the battery dynamics. However, due to the high complexity of this model, it does not appear feasible for applications with low overhead computational means (e.g., real-time performance estimation/prediction of battery power management systems). Kim et al. [115] in 2011 improved the model in [113] by combination of the model with KiBaM scheme to account for the recovery and rate capacity effects. However, the model is not appropriate for real-time applications, still due to their high complexity.

To sum up, we can say that all the existing battery models have at least one of the following drawbacks:

i)   Requiring intensive computation due to the high complexity,

ii)   Not applicable for electrical circuit design and simulation,

iii)   Not capable of accurately capturing the dynamic behavior of the battery and SoC tracking due to the neglect of the nonlinear capacity effects.

As a result, this part of the thesis is focused on an accurate battery model with good tradeoff between performance, complexity, and parameterization effort.

2.3.3 Proposed Battery Model

Since, equivalent circuit models have a good tradeoff between exactness, complexity, and usability, the proposed model in this thesis is based on the model presented in [106] using Two Time Constant (TTC). The TTC model allows to take into account slow electrochemical process characterizing the slow charging/discharging and redistribution phases. This model is certainly the most popular in view of its low computational burden and straightforward implementation in electrical circuit solvers. It is shown in Figure 2-36.
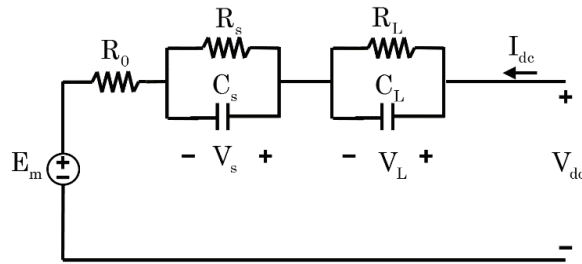
Figure 2-36 Classic TTC model for batteries

R_0 is the battery input resistance which is used to characterize the charge/discharge energy losses of the battery cell. It models the effects of finite conductivities in the electrodes and separators, the limited reaction rates at the electrodes, and the concentration gradients near the electrodes.

R_s, C_s are the resistance and the capacitance of the first branch respectively, modeling the fastest electric dynamics; C_s models the effects arising from polarization and the diffusion of charges near the electrode/electrolyte interface.

R_L, C_L are the resistance and the capacitance of the second branch respectively, modeling the slowest electric dynamics;

E_m is the electromotive force of the battery which can be measured as voltage across the open circuit terminals.

All the above parameters are nonlinear and depend on SoC , temperature and Crate [116]- [117]. In order to account for the limitations of the classic TTC model, this

work proposes an Enhanced TTC (ETTC) model accounting for the charge redistribution phenomena. Indeed, the idea of the proposed model for DLSC is extended for BESS. In this respect, a virtual current generator (I_{vir}) is considered as illustrated in Figure 2-37.
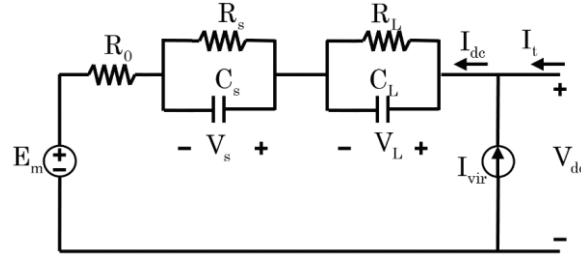
Figure 2-37 Proposed enhanced TTC (ETTC) model

The parameters of the model depend on SoC, Crate and temperature. The variability of the model parameters versus SoC is accounted by using the look-up tables containing the values of the parameters corresponding to discrete SoC values. And the dependency of parameters on Crate is accounted by the virtual current generator.

a) Optimal assessment of parameters

Several work have been performed for estimating the parameters of the cell and modeling their dependency to the SoC [118]-[116]-[119]-[120]. Despite of being successful in many aspects, most of them still have several drawbacks such as high complexity or low accuracy. In this work the parameters of the circuit of Figure 2-37 is assessed by using experimental data. For inferring the dependency of the parameters on SoC, Crate and temperature, one of them is considered to be variable and the other ones are assumed constant. The lookup table representing the $V_{oc} - SoC$ relationship is obtained by performing the following test:

- <u>Test I</u>. $V_{oc} - SoC$ lookup table

This test has been performed into a climatic chamber where the temperature is strictly set to the nominal value of the cell, namely 25°C. The discharge current is set to 1Crate. This condition is considered as benchmark. (1Crate, 25°C).

Step 1: The V_{dc} range is divided into n intervals between zero and the rated voltage $\left\{ V_{dc,1}^{F}, V_{dc,2}^{F}, ..., V_{dc,n}^{F} \right\}$.

Step 2: The fully-discharged battery is charged with 1Crate until reaching $V_{dc,i}^{F}$

Step 3: The battery rests for 30 minutes and V_{oc} is recorded.

Step 4: The battery is discharged completely and the value of the extracted charges is recorded. Consequently, the related SoC is computed.

Step 5: Steps 2-4 are repeated for {i=1,..,n} to obtain the corresponding $V_{oc} - SoC$ lookup table.

It should be noted that the new tested battery had to be cycled before starting the tests.

In order to evaluate the parameters, the following pulse test is carried out.

- ▪ Test II. Pulse discharge test to infer the parameters

Step 1: The SoC range $\begin{bmatrix} 0 & 1 \end{bmatrix}$ is divided into certain number $\{SoC_1, SoC_2, ..., SoC_n\}$. In our case it is divided with 0.1 interval.

Step 2: A fully-charged battery (SoC=1) is discharged with 1Crate until reaching the next SoC interval (SoC=0.9 in our case).

Step 3: The battery rests for 30 minutes.

Step 4: It is discharged with 1Crate until reaching the next SoC interval (SoC_i).

Step 5: Steps 3-4 are repeated for {i=1,..,n} until fully-discharged condition reached.

In other words, a pulse discharge current profile is applied to the battery. The current and voltage profiles are shown in Figure 2-38. The results obtained for each of these intervals is used to obtain the parameters related to each corresponding SoC.
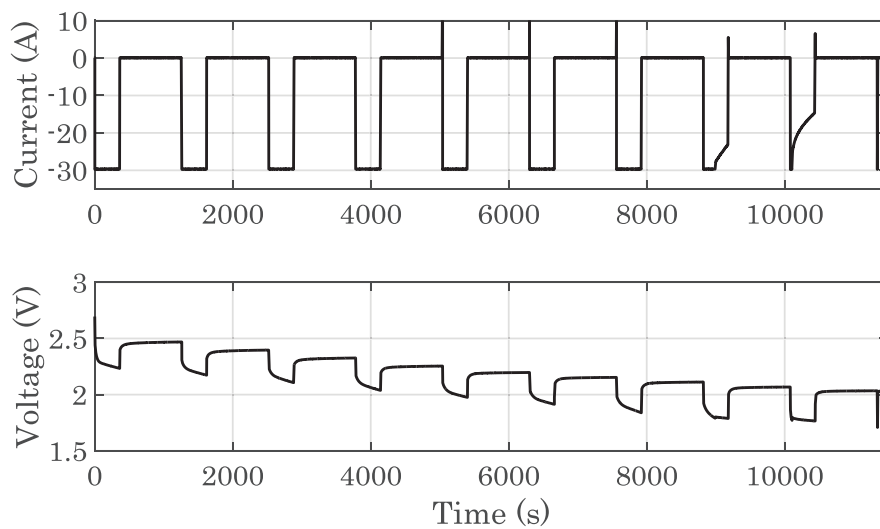
Figure 2-38 Pulse discharge current test

It is possible to assume that, during the targeted cycle, the terminal voltage, $V_{dc}(t)$, can be represented as a function of the relevant circuit parameters:

$$V_{dc}(t) = f_1 \left[I_{dc}(t), R_S, C_S \right] + f_2 \left[I_{dc}(t), R_L, C_L \right] + f_3 \left[I_{dc}(t), R_0, E_m \right] \tag{2.13}$$

Where:

f_i (i=1, 2, 3) are the circuit equations of the cell model and represent the contribution of electrical elements to $V_{dc}(t)$;

For each of SoC intervals the difference between the simulated battery cell voltage $V_{dc,i}$ and the measured battery cell voltage $V_{dc,i}^m$ can be used to determine the model parameters using a least square fitting procedure.

$$\underset{\substack{R_s, C_s, R_L, \\ C_L, R_0, E_m}}{arg\ min} \left\{ V_{dc,i}^m - V_{dc,i} \right\}^2 \tag{2.14}$$

a) Model initialization

The time domain equations of the TTC model is presented in (2.15).

$$V_{dc}(t) = E_m + (R_0 + R_S + R_L).I_{dc}(t) +$$
$$(V_s(t_0) - R_S.I_{dc}(t)) e^{\frac{-(t-t_0)}{R_s C_s}} + (V_L(t_0) - R_L.I_{dc}(t)) e^{\frac{-(t-t_0)}{R_L C_L}} \tag{2.15}$$

In order to initialize the cell model, the knowledge of its initial SoC is necessary. For this purpose, the $(V_{oc} - SoC)$ lookup table is used. This lookup table for the targeted LTO cell is given in Table 3.

Table 3: Open circuit voltage and associated stored charge

V_{oc} (V)	SoC (pu)
1.77	0
1.85	0.15
2.06	0.32
2.18	0.52
2.28	0.64
2.37	0.76
2.46	0.87
2.70	0.98

In order to accurately measure V_{oc}, the cell is kept in a relaxation phase for few hours. The terminal voltage associated with the end of this sub-phase is the V_{oc}. If the V_{oc} is between two discretized values, the associated SoC can be inferred by a linear interpolation between these two values. Once the SoC_{init} is computed, the initial values of the six parameters ($R_0, R_s, R_L, C_s, C_L, E_m$) are evaluated.

The proposed TTC model has two state variables, namely the voltage V_s and V_L across C_s and C_L, respectively. The initial values for these voltages should be calculated. From circuit theory and by using the Laplace transformation, we have (2.16)

$$\frac{V_s}{V_L} = \frac{C_L \cdot s + \frac{1}{R_L}}{C_s \cdot s + \frac{1}{R_s}} \qquad (2.16)$$

Also, by rewriting (2.15) at initial point ($I_{dc} = 0$), we will get (2.17).

$$V_s(t_0) + V_L(t_0) = V_{dc} - E_m \qquad (2.17)$$

With a very good approximation (2.16) can be written as (2.18).

$$\frac{V_s}{V_L} \approx \frac{R_s}{R_L} \qquad (2.18)$$

Using (2.17) and (2.18), the initial values of V_s and V_L are inferred.

b) *Computation of the virtual current generator contribution*

If Crate is different from the one used for the parameters assessment, the virtual generator is activated in order to account for the different amount of charge being redistributed in comparison with the amount of the reference benchmark cycle (1Crate, 25°C). The virtual current generator delivers the following current (2.19).

$$I_{vir} = \frac{\Delta Q_{RED}}{\tau_S} \eta_1 e^{-t/\tau_S} + \frac{\Delta Q_{RED}}{\tau_L} \eta_2 e^{-t/\tau_L} + \frac{\Delta Q_{RED}}{T} \eta_3 e^{-t/T} \qquad (2.19)$$

where ΔQ_{RED} is the amount of charge to be redistributed in order to model the recovery effect for a case different from the reference one; τ_S and τ_L are the time constant of the two RC branches; T is the charging/discharging time for the targeted cycle sub phase; η_1, η_2 and η_3 define the share of each time constant (they are proportional to their respective time constants).

At a given time window $\begin{bmatrix} t_0 & t_1 \end{bmatrix}$, the amount of $\Delta Q_{RED}(t_1)$ is computed by (2.20).

$$\Delta Q_{RED}(t_1) = \Delta Q /_{1C}(t_1) - \Delta Q /_{iC}(t_1) \tag{2.20}$$

Where $\Delta Q /_{1C}(t_1)$ and $\Delta Q /_{iC}(t_1)$ are the amount of charges needed from the cell to pass from the $SoC(t_0)$ to $SoC(t_1)$ with 1Crate and a generic iCrate, respectively.

$$\Delta Q /_{1C}(t_1) = \left(SoC(t_1) - SoC(t_0) \right) \cdot C(I /_{1C}) \tag{2.21}$$

$$\Delta Q /_{iC} = \int_{t_0}^{t_1} I_{dc}(t) dt \tag{2.22}$$

Where $C(I /_{1C})$ is the capacity of the battery at 1Crate. Thus, the value of ΔQ_{RED} is continuously updated. It is necessary to underline that the virtual generator does not violate the principle of charge conservation. In fact, it does not inject any external charge but it models the internal flow of the charge previously stored in the device. It should be noted that in order to prove that the proposed model is robust regarding the temperature variations, the assessment of the model parameters has been performed for different temperatures.

2.3.4 Experimental Validation

The trend of $V_{dc}(t)$ with the optimally-identified parameters at 1Crate at 25°C (the reference case) is shown in Figure 2-39. It can be observed that the optimally-identified parameters allows to obtain a quite good matching between the predicted $V_{dc}(t)$ and the measured one.

The limitation of the TTC model appears when the cell is cycled with Crate different from the one used to infer the parameters. This limitation arises from the fact that the presented TTC model is not able to account completely for the rate capacity and recovery effects. This can be seen in Figure 2-40, when 0.66 Crate is used. The battery DC voltage obtained from the simulation is compared with the measured one. It can be observed that in this case, the TTC model is unable to model correctly charge-flow coming from the inner layer to the surface layer and vice versa.
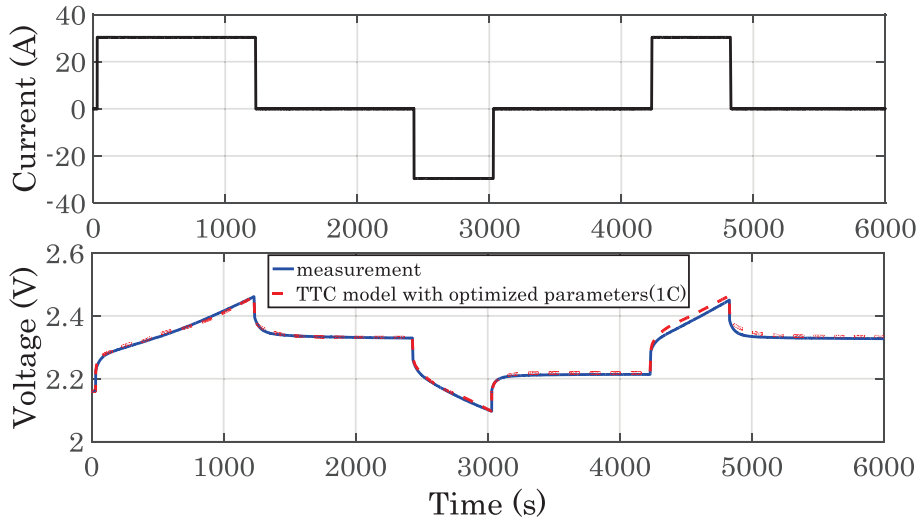
Figure 2-39 Comparison of predicted and measured trend of the LTO cell voltage during the cycle used for the parameter assessment (1Crate)
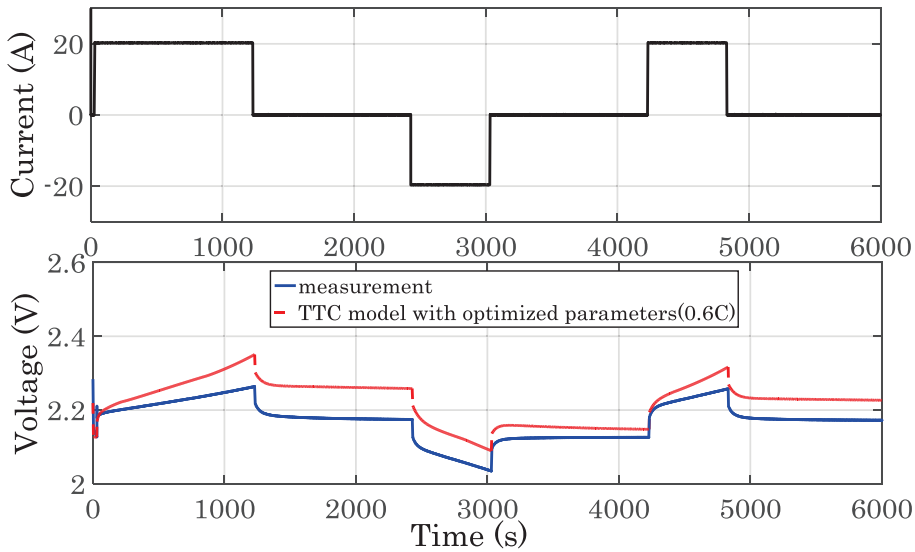
Figure 2-40 Comparison of simulated and measured trend of the LTO cell voltage during a cycle at 0.66Crate

The proposed model is experimentally validated with various cycles characterized by different charging, discharging Crate and relaxation phases. It is also shown that the ETTC model is robust against the temperature variations.

Figure 2-41 shows the results for the same cycle as Figure 2-40 with TTC and the proposed ETTC models. It can be seen that the proposed model can accurately reproduce the battery dynamic behavior. Furthermore, the model is able to accurately trace the SoC variation. It should be underlined that the mean squared error between the battery measured voltage and the proposed one is extremely low

and in the order of 10^{-4} and a corresponding value of 0.003 has been evaluated for TTC model.
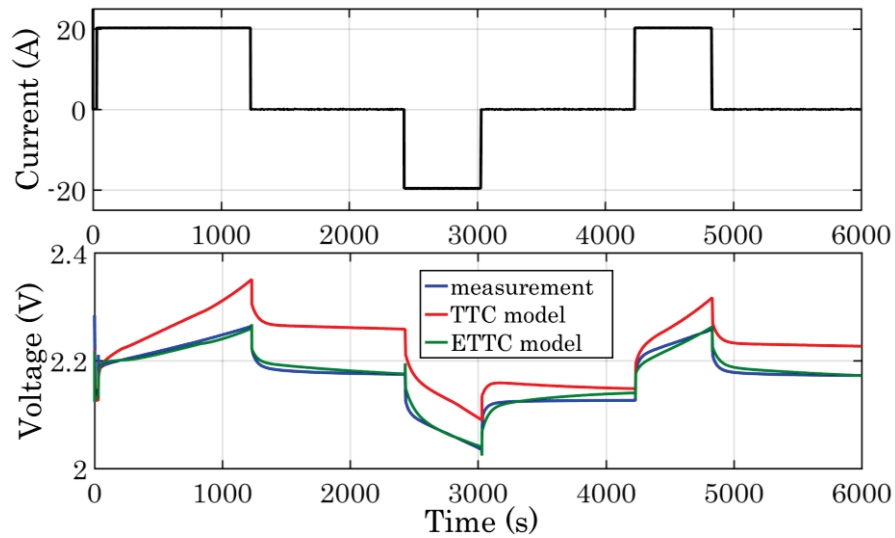
Figure 2-41 Time evolution of battery DC voltage with 0.6Crate
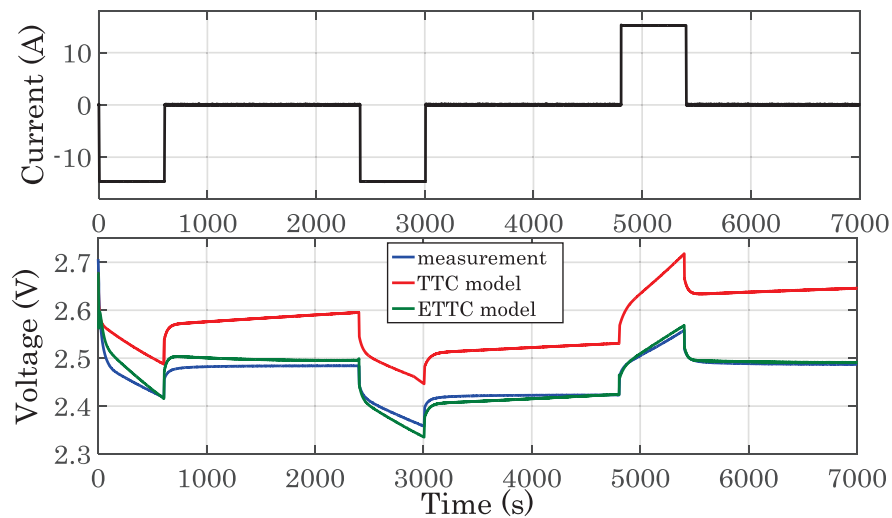
Figure 2-42 Time evolution of battery DC voltage with 0.5Crate

Figure 2-42 illustrates the experimental validation of the proposed ETTC model for a 0.5 Crate. The results are compared with those derived from the classic TTC model. As it can be observed, unlike the TTC model, the proposed ETTC model is able to predict the voltage evolution. It is possible as well to observe that if the starting point (initial V_{OC} and/or initial SoC) change the TTC model is not able to accurately predict the electrical battery dynamic. The mean squared error between the battery measured voltage and the TTC one is of 0.3% and a corresponding value of 0.01% has been evaluated for ETTC model.

In order to prove the applicability of the model with respect to more realistic charge/discharge profiles, we have adopted the battery current profile inferred from [14] that makes reference to a microgrid application of a battery storage system. We have here adopted the battery current profile related to test (a) of [14] and reproduced it by means of the same battery test bench. In Figure 2-43 we report the time evolution of the battery DC voltage with respect to this specific test condition. As it can be noticed, even for this peculiar cycle characterized by a highly dynamic current profile, the proposed model matches the measurements with a high level of fidelity. In this respect, it can be concluded that the proposed enhanced battery model represents an adequate extension of the classical electrical circuit one with a minimal computational overhead.
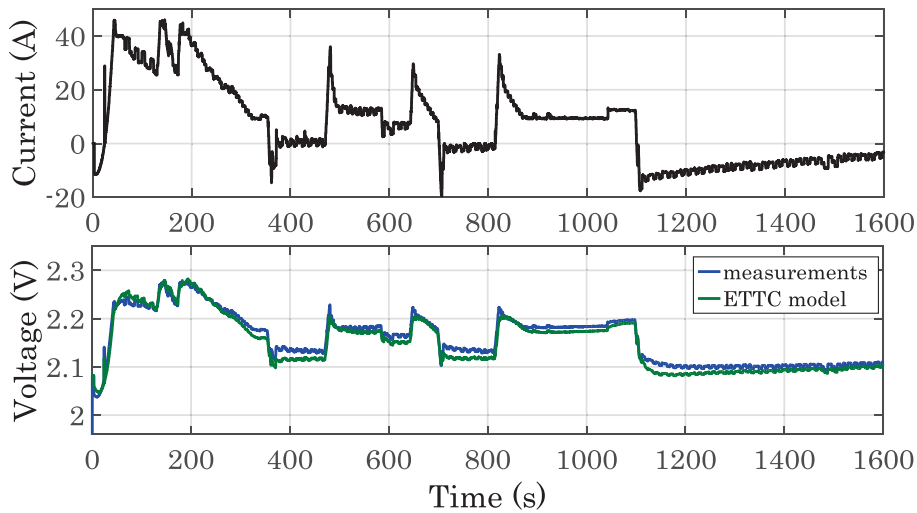
Figure 2-43 Time evolution of battery DC voltage with respect to realistic fast charge/discharge profiles

Also, BESS lifetime declared by the manufacturer is referred to the nominal temperature that, for the majority of cell technologies, is of 25°C. However, these devices are, in real operating conditions, placed in environments where the temperature could be far from the nominal one. Consequently, the BESS model should be capable to consider the temperature effects on the dynamic behavior of the cell. In order to show that the ETTC model is robust against the temperature variations, Figure 2-44 illustrates the comparison between the measured voltage and the predicted ones in the case of the common TTC model and the case of the ETTC model, with a 2C discharging current at 45°C. The mean squared error between the measured cell voltage and the TTC one is of 0.42% and a corresponding value of 0.014% has been evaluated for the ETTC model. Moreover, it is important to predict the DC voltage of the battery pack system instead of a single cell. There is a lack of literatures related to this topic. In this respect, the parameter assessment along with the characterization of the virtual generator has been performed for a battery

system of 25 kWh, 50 kW and composed by 900 cells connected in series and in parallel at EPFL-DESL laboratory in Lausanne, Switzerland. Figure 2-45 illustrates the experimental validation of the proposed model for the above battery system. The mean squared error between the batteries measured voltage and the ETTC one is 0.0082%.
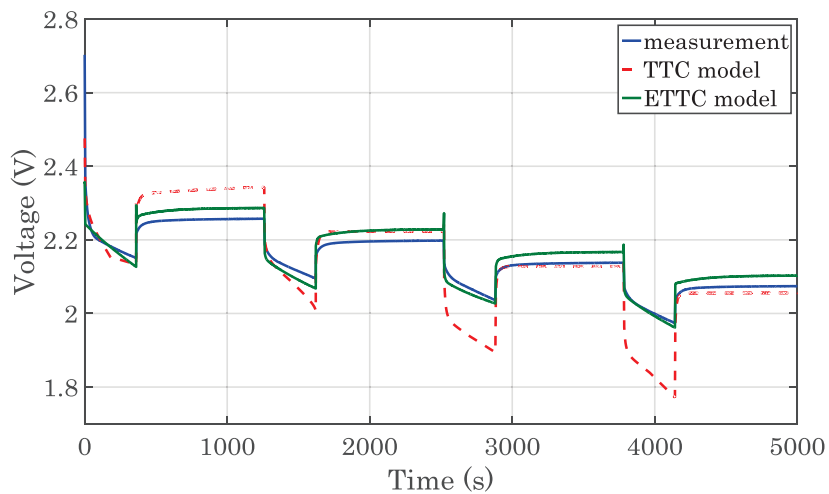
Figure 2-44 Time evolution of the targeted BESS voltage with 2Crate and at 45°C
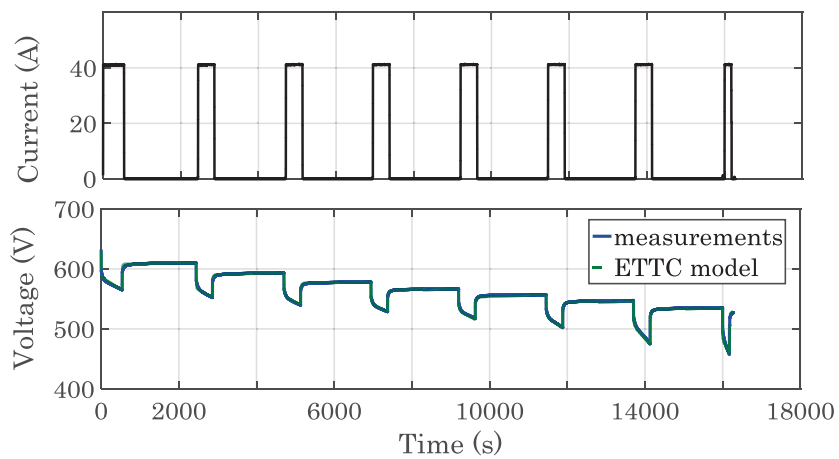
Figure 2-45 Time evolution of battery pack DC voltage with respect to realistic charge/discharge profile

Conclusion

Modeling of electrochemical energy storage systems is a subject that always receives attention in view of the increasing importance of storage devices in power systems and mobility applications. In this respect, the accurate estimation of storage system states is utmost important. Among the several approaches proposed in the literature to estimate the state of charge of energy storage systems, coulomb counting method is more appropriate for online estimations. However, this method does not entirely account for the nonlinear capacity behavior. In this regard, this chapter first proposed an accurate algorithm for state-of-charge estimations. Then, detailed dynamic models for supercapacitors and lithium-based batteries have been proposed to enhance the dynamic behavior by representing the so-called charge redistribution phenomenon that characterizes the dynamic of the storage system voltage during long time charging/discharging and relaxation phases. Making reference to experimental tests carried out on a 325F supercapacitor and a Lithium-Titanate battery in DESL-EPFL Smart Grid Laboratory, the chapter has first discussed the optimal parameters assessment of the relevant models and, then, it has shown the improvement of the model behavior by accounting for the charge redistribution phenomenon. In this respect, it can be concluded that the proposed enhanced models represent an adequate extension of the classical ones with a minimal computational overhead.

3

Advanced Decentralized Control of Active Distribution Networks with the Integration of Dispersed Energy Storage Systems

Summary

This chapter focuses on the advanced decentralized control of Active Distribution Networks (ADNs) actuated by means of a limited number of Distributed Energy Storage Systems (ESSs). This chapter includes three parts. Part I presents a network partitioning strategy for the optimal voltage control of ADNs. The proposed partitioning uses voltage sensitivity concept in order to linearize the problem. Then in part II, two decentralized operational scheduling algorithms are proposed relying, respectively, on Thévenin equivalents and a recursive approaches. Part III proposes a real-time decentralized control algorithm for the clustered ADNs using only distributed Battery Energy Storage Systems (BESSs). In particular, we propose a zonal control strategy targeting voltage support and line congestion management. The proposed zonal control relies on an accurate dynamic model of BESSs capable to account for their DC active power limits. In both proposed decentralized scheduling and real-time control algorithms, the communication among different areas is defined using the concept of multi-Agent Systems (MAS). The effectiveness of the proposed zonal control/scheduling methods is assessed using test cases composed of the IEEE 13 and IEEE 123 nodes distribution test feeders suitably adapted to include stochastic generation and ESSs.

Introduction

In this thesis, ESSs are identified to be the only controllable devices in order to provide active support to mitigate line congestions, provide voltage support as well as spinning reserve in the operation of ADNs. The control of ESSs can be achieved using either centralized or decentralized schemes. Theoretically, operation and control of ADNs can be achieved centrally, as for transmission systems through the dispatch of active and reactive power of ESSs. Such an active management scheme would involve the centralization of all the information and consequent decisions in a single processing unit (or Central Controller) [121]. Although the centralized strategy is the most straightforward way to achieve the management of the network, it has several drawbacks: (1) there is a consequent computation complexity associated to the central information gathering/processing; (2) it faces difficulties in some applications when global information is not available [122],[123]; (3) in case of a failure of the central supervisor, the control is lost all over the network; (4) it needs high investment in communication and data processing. Due to the above-mentioned downsides, the question arises whether centralized schemes are still the most appropriate. A possible solution is to move from the centralized operation paradigm to the decentralized one subdividing the network into quasi-autonomous entities defined as areas, zones or clusters (these terms are used as synonyms in this thesis). To this end, given a set of ESSs optimally located in a balanced and radial ADN, the network is decomposed into several areas; each under the control of one ESS. In order to define a decentralized scheme and decrease the communication costs and computation burden, the following assumptions are made:

(i)   The operating information within each zone is not shared with the others;

(ii)   Each zone is independently controlled merely relying on the dedicated single ESS unit whose control variables are its active and reactive power set points; thus, it does not contain any directly-controllable generator, or load.

(iii)   The proposed zonal control capability focuses on voltage control and line congestion management.

(iv)   It is considered that the locations of ESSs in the network are provided by the process described in [124]. It consists of an optimal planning method accounting for the investment and operation costs of the ESSs.

As a result, operation scheduling and real-time control of ADNs are proposed to perform in a decentralized manner. Agent techniques are employed to search for a solution of efficient dispatching through agent-based communication, reasoning and

decision making. MAS [125] consists of a collection of agents that directly interact via a form of message passing. One of the main advantages of MAS is the ability to distribute agents across multiple execution units. In contrast to monolithic, centrally controlled systems, such a distribution scheme improves the robustness of the system by moving control software closer to the hardware.

This chapter contains three parts. Part I proposes a network clustering algorithm with the aim of optimal voltage control of ADNs. Part II illustrates two proposed decentralized operation scheduling algorithms using a linear programming technique relying on the so-called voltage sensitivity coefficients. The associated message exchange processes are shown as well. The effectiveness of the proposed algorithms is assessed and their performances are compared with those of the equivalent centralized scheme. Part III proposes the decentralized grid real-time control strategy including voltage control and congestion management based on the BESS dynamic model presented in chapter II. The performance evaluation of the proposed algorithms is presented making reference to the IEEE 13 and 123 nodes test distribution feeders.

Part I. Active Distribution Network Clustering

This part is structured as follows: Section I.1 summarizes the method proposed in the literature for network clustering and then, the proposed clustering algorithm is presented in section I.2. Section I.3 shows an illustrative example on the proposed algorithm making reference to IEEE 13 nodes test feeder.

3.1.1 Review of Existing Clustering Techniques

The partitioning of electrical networks can be approached in several ways. Wanger et al. in 1990 [126] proposed a simple rule-based approach for transmission system clustering. A network graph technique is used for this purpose. Lyons et al. in 2006 [127] proposed a collection of zones of variable size where supply/demand are kept balanced in order to efficiently control dispatchable DGs. The fluctuations in supply/demand (such as peak/off-peak load variations) change the boundaries of the zones. The drawback of this method is that all the buses need to belong to all possible areas. Further, it requires the direct control of each DG unit. In [128] a partitioning algorithm is proposed using the so-called community detection theory. It is assumed that the network is initially decomposed in pre-defined areas. Then, the algorithm tries to merge them in such a way that the local reactive power balance inside the resulting areas is fulfilled. This approach is appropriate only for transmission system since the voltage is controlled only by adjusting the reactive power. However, voltage variations in distribution networks may depend also on active powers as a

function of the R/X ratio of lines longitudinal parameters [129]. [130] proposes a novel partitioning algorithm using community detection theory as well. A hierarchical scheme divides the power grid into areas in which electrical distances between the nodes inside each one are close to each other. This method is also suitable for transmission network for the same reason. [131] designs a network partitioning strategy that enables the efficient management of DGs and reduces costs. In this approach, a node can be included in an area neglecting the fact that it should be connected physically to the corresponding area. In other words, along the path connecting this node to the corresponding area, there are nodes belonging to other areas. [132] proposes a partitioning method for AND accounting for the influence of DGs. None of the partitioning methods existing in the literature accounts for technical issues such as voltage control or line congestion managements along with electrical distances between nodes.

3.1.2 Proposed Clustering Technique

A network partitioning method is proposed considering the voltage control of ADNs. In order to decouple the voltage control among a set $\mathcal{B}$ (dim$\{\mathcal{B}\}$=B) of ESSs optimally located in a balanced and radial ADN, the proposed partitioning algorithm decomposes the ADN into several quasi-autonomous zones, each one under the control of a single ESS. Therefore, the boundaries of each area are determined with this criterion: each ESS within a zone of unknown border must have significant influence on the co-zonal controlled variables (in our case the node voltages) in comparison with the nodes outside the zone of interest. In order to achieve such a goal, there is the need to quantify the influence of the control variables (i.e., nodal power injection/absorptions of each ESS) on the controlled ones, namely the node voltages. The use of linear programming through voltage sensitivity coefficients (*VSC*) is used for this purpose (e.g.,[133], [134], [135], [136], [137]). As known, *VSC* depends on the topology and the operating state of the grid. In this study, it is relied on the method presented in [133] to compute the *VSCs*. Given a certain operating state of the network, $VSC_{i \to j}$ quantifies the change on the voltage at node j for a variation of the injected/absorbed active/reactive powers at node i.

The steps of the proposed heuristic decomposition algorithm are described hereafter.

Step 1. Computation of the *VSC* matrices: for a given network operating state Γ^1, two sensitivity matrices are computed for both active and reactive powers

---

$\left(\left[VSC^P \right]_{B \times N} \right.$ and $\left. \left[VSC^Q \right]_{B \times N} \right)$. The relevant elements can be formally defined as in (3.1) (N is the number of network nodes and B the number of ESS units).

$$VSC_{i \to j}^{P} = \frac{\partial V_j}{\partial P_i}\big|_\Gamma \; ; \; VSC_{i \to j}^{Q} = \frac{\partial V_j}{\partial Q_i}\big|_\Gamma \; ; \; i \in B \, ; \, j \in N \tag{3.1}$$

Step 2. Assessment of the ESSs voltage influence factors (*VIF*): the *VIF* of a generic ESS located at node i on node j is defined as the ratio of a given VSC defined by (3.1) and the scalar sum of all *VSCs*. As a result, two influence matrices ($\left[VIF^P \right]_{B \times N}$ and $\left[VIF^Q \right]_{B \times N}$) are derived using (3.2).

$$VIF_{i \to j}^{P} = \frac{\partial V_j \big/ \partial P_i}{\sum\limits_{n=1}^{N} \partial V_n \big/ \partial P_i}\big|_\Gamma \; , \; VIF_{i \to j}^{Q} = \frac{\partial V_j \big/ \partial Q_i}{\sum\limits_{n=1}^{N} \partial V_n \big/ \partial Q_i}\big|_\Gamma \tag{3.2}$$

Step 3. Merge matrices $\left[VIF^P \right]_{B \times N}$ and $\left[VIF^Q \right]_{B \times N}$: the use of (3.2) allows to infer two matrices $\left[VIF^P \right]_{B \times N}$ and $\left[VIF^Q \right]_{B \times N}$. In order to have a more compact indicator considering both effects of active and reactive powers of ESS simultaneously, it is proposed to merge these two matrices in a single one $\left[VIF \right]_{B \times N}$. For this purpose, a linear relationship is built based on the concept of the electric distances using (3.3). $\left[VIF^P \right]_{B \times N}$ and $\left[VIF^Q \right]_{B \times N}$ are weighted by the corresponding resistance and reactance electric distance between the nodes respectively. This can be easily proven numerically as shown in the appendix A.

$$[VIF]_{B \times N} = [\alpha]_{B \times N} \cdot [VIF^P]_{B \times N} + [\beta]_{B \times N} \cdot [VIF^Q]_{B \times N} \tag{3.3}$$

Each element of $[\alpha]_{B \times N}$ and $[\beta]_{B \times N}$ are defined as in (3.4).

$$\alpha_{i \to j} = \frac{\left(\sum R_{ij} \right)^2}{\left(\sum \left| \overline{Z}_{ij} \right| \right)^2} \; ; \quad \beta_{i \to j} = \frac{\left(\sum X_{ij} \right)^2}{\left(\sum \left| \overline{Z}_{ij} \right| \right)^2} \quad ; \alpha + \beta = 1 \tag{3.4}$$

Where $\sum R_{ij}$, $\sum X_{ij}$ and $\sum \overline{Z_{ij}}$ are respectively the sum of the line resistances/reactances/impedance of the lines between node i and node j. As a result, a single matrix $\left[VIF \right]_{B \times N}$ is obtained.

Step 4. Network node clustering with respect to the ESS units: as anticipated, only one ESS per area is considered. For each node, the ESS that has the most impact is determined by finding the maximum component value of each column of the matrix $\left[VIF \right]_{B \times N}$. More precisely, each node is assigned to the area associated to the ESS with the highest VIF on that node. In this way, it is guaranteed that each node belongs to one and only one area.

It should be noted that the $VSCs$ computation at each time-step requires solving a central load flow problem. Deterministic load flow ignores uncertainties in power systems nodal power fluctuations (i.e., those of DG and loads). Whereas it is expected that such uncertainties would change the frontiers of the zones. Actually, changing the borders accordingly (dynamic partitioning) contradicts the assumption that each zone should independently control its area without sharing any information with the neighbors. In order to take into account for this aspect, different mathematical approaches can be used, such as the probabilistic approach, fuzzy sets and interval analysis. Probabilistic Load Flow (PLF) (e.g.,[138]) has been applied instead of a classical deterministic load flow in order to consider the possible combinations of loads/generations. The PLF requires a priori knowledge of the Probability Distribution Functions (PDF) of the nodal powers injections/absorptions together with their time covariance. In order to infer this statistical information, a set of experimental data (available for a time period of one year) obtained from a real ADN located in the south-east region of Switzerland is used. For each time period t^* (in our case t^* corresponds to a slot of 15 minutes) of a given day d, the empirical Cumulative Distribution Function (CDF$_{d,t^*}$) of nodal injection powers is built using all the measurements collected at t^* in correspondence of $d\text{-}15$ and $d\text{+}15$. 96 CDFs of active/reactive powers per day and per node are obtained. From the knowledge of the nodal CDFs, the PLF is solved numerically using a Monte Carlo Simulation (MCS) (e.g., [139]). For this purpose, the nodal powers are assumed as Independent and Identically Distributed (IID) variables.

It is worth noting that since the electric distances between the system nodes are considered in the proposed clustering method using (3.3), the nodes always tend to remain in the area corresponding to the closest ESS. In addition, a PLF have been performed for an entire year to infer the VIF of ESS powers at the grid nodal voltages. Thus, all the possible combinations of loads/generations accounting for the uncertainties of the stochastic resources are considered.

It should be noted that running PLF for partitioning the grid inherently accounts for the uncertainties of the stochastic resources connected to the system (i.e., loads and stochastic generation). Therefore, the associated computation of *VSC* accounts for these uncertainties.

3.1.3 Illustrative Example

In order to illustrate the partitioning algorithm, an example is presented in this part referring to the IEEE 13 nodes distribution test feeder. It is supposed to have non-dispatchable DG units composed of PVs (on nodes 4, 8 and 10). The power injections of PVs are represented by voltage-independent active power injections with null reactive component. Concerning the representation of the network loads, they are considered as voltage independent PQ absorption. Three ESSs (on nodes 6, 4 and 12) are optimally located. Figure 3-1 and Figure 3-2 show respectively the CDFs of the load apparent power absorptions and PV active power injections for a summer and a winter day for node 9 of the benchmark grid of Figure 3-4. The PLF is performed along 1 year generating 10000 runs per 15 min. The obtained minimum/maximum variations of the *VIF* for the three ESS are plotted in Figure 3-3. As it is seen, the nodes with the highest *VIF* belongs to the corresponding area where the associated ESS is located. The network schematic and the obtained zones decomposition are shown in Figure 3-4.
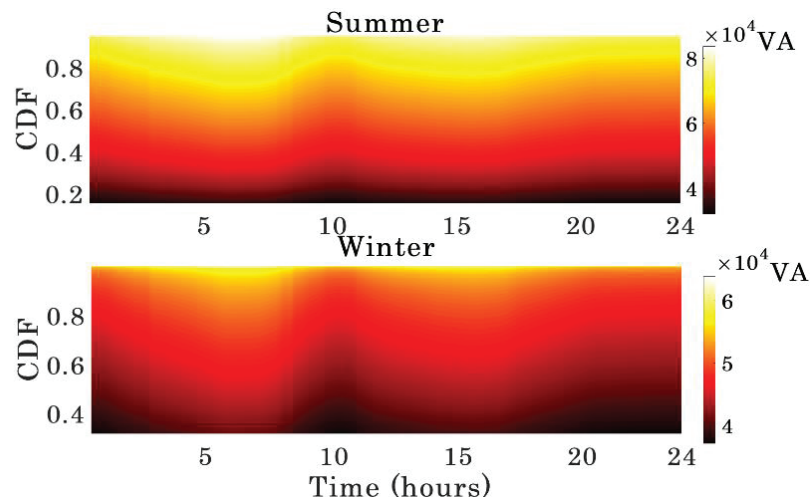
Figure 3-1 CDFs of load apparent power during summer-winter for node 9 of 13 bus system
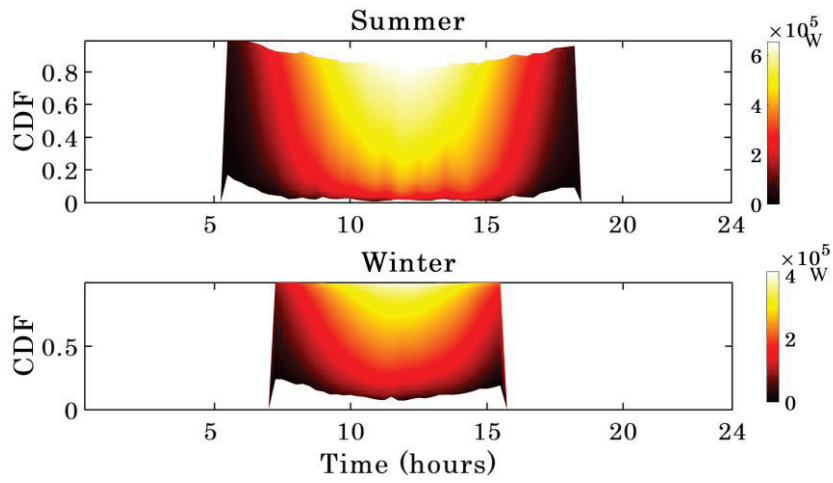
Figure 3-2 CDFs of PV generation during summer and winter for node 9 of 13 bus system
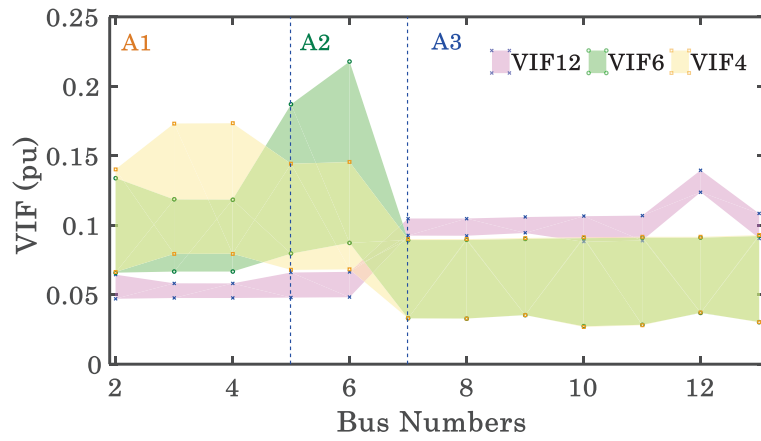
Figure 3-3 Annual range of *VIF* of ESSs on all nodes of 13 bus system
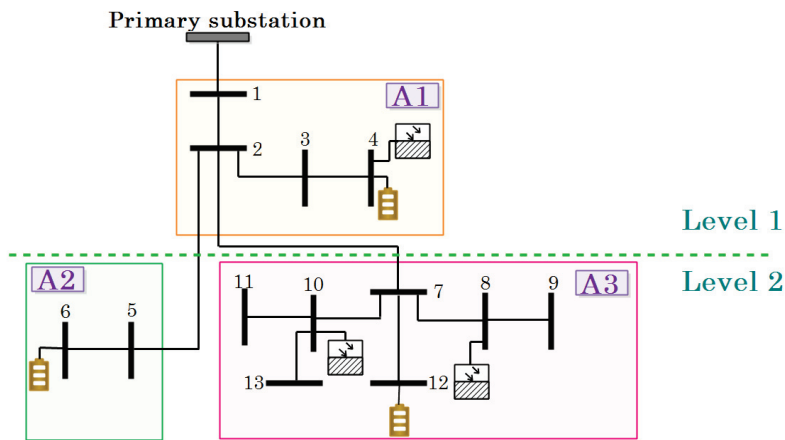
Figure 3-4 Clustered IEEE 13 bus test system.

Part II. Decentralized Optimal Operation Scheduling Method of Energy Storage Systems in Clustered Active Distribution Networks

Fast optimal scheduling of controllable resources in ADNs is essential for operation of the grid with inherent stochastic players such as renewable sources and electric vehicles. Optimal scheduling brings significant impact on secure and economic operation of ADNs. This part presents optimization-based decentralized methods using adaptive control schemes in order to optimally operate ESS in coordination with renewable energy resources and load variations. Thus, the proposed models generate optimal charge/discharge schedules of ESS, while satisfying distribution network operational constraints such as voltage limits over a finite time horizon.

This part is structured as follows: According to the literatures, section II.1 presents different existing dispatching scheduling model for ADN. Then, section II.2 illustrates two proposed decentralized scheduling algorithms relying, respectively, on Thévenin equivalent and recursive approaches. Section II.3 presents the performance assessment of the decentralized proposed algorithms making reference to the IEEE 13 and 123 nodes test distribution feeders.

3.2.1 Review of Existing Operational Scheduling Techniques

Several studies have focused on the optimal operation of ADNs with distributed energy resources and ESSs. All scheduling methods propose either partially non-convex formulation of the Optimal Power Flow (OPF) problem (requiring the use of heuristic techniques) (e.g., [140], [141], [134], [142], [143], [144], [145], [146]) or address only the economic dispatch problem (e.g., [147], [148], [149], [150], [151], [152], [153]). The main challenge corresponding to the scheduling methods using OPF is related to the computational speed since making the OPF problem convex results in an increase in the computational burden. The main drawbacks with the economic dispatch methods is that the technical constraints related to electrical network constraints are not modeled and taken into account for.

In addition, most of the scheduling methods existing in the literature have been developed according to a centralized way [154], [144], whereas very little work has been developed according to a distributed way [155], [11]. In these works, different power dispatch algorithms are proposed for DGs focusing only on reactive power dispatch. However, the reactive power compensation relying on those DGs' inverters could not be sufficient to achieve satisfying grid control. In order to overcome the downsides of the existing ADNs scheduling methods, we propose decentralized stochastic methods to solve the day-ahead optimal scheduling problem of radial

ADNs in presence of ESSs and renewable resources. The proposed method is developed using MAS with the aim of voltage control. For this purpose, ESSs are modelled by representing their State-of-Energy, as well as their capabilities, to support the network by variable injected/absorbed active/reactive powers on the four quadrants.

3.2.2 Proposed Decentralized Operational Planning Methods

Two decentralized optimal scheduling algorithms are proposed relying, respectively, on Thévenin equivalent and a recursive approaches. These algorithms are developed using the MAS concept.

3.2.2.1 MAS Structure

According to the clustering method presented in part I, the whole distribution network is divided into K areas; each one including only one ESS. This consideration introduces the idea that the scheduling management problem might be solved in a distributed manner. Therefore, each area should have zonal control capability. For this purpose, an agent is assigned to each area which is called "area agent". An agent is a piece of software or a hardware that can perceive any changes in its environment through sensors and act upon through actuators. MAS is one of the most convenient approaches distributing the control in a large-scale system. MAS is composed by multiple intelligent agents that are able to process the data and make the decision in a distributed manner [156]-[157]. Intelligent agents can be defined by the following typical characteristics: Reactivity, pro-activeness and social ability. Reactivity of agents is the ability of agents to perceive their environment and respond in a timely fashion in order to satisfy their design objectives. Pro-activeness of agents exhibits goal-directed behaviors by taking the initiative in order to satisfy their design objectives. Social ability of agents is the interaction of agents with other agents in order to satisfy their design objectives. These characteristics signify the importance of MAS in developing a complex system. All the interactions between agents take place via a form of message passing. The Foundation for Intelligent Physical Agents (FIPA) defines agent's communication in terms of a function, or action called Communicative Act. There are several type of exchanged messages. Some of them are used in this thesis:

INFORM: the sender informs the receivers that some actions are performed. It also sends its new updates.

REQUEST: the sender requests the receivers to perform some actions.

CONFIRM: the sender informs the receivers that a given proposition is true, where the receiver is known to be uncertain about the proposition.

In this study, the proposed zonal scheduling scheme is implemented with the aim of voltage control since the frequency is dictated by the upper transmission network. Due to the hypothesis of the radial structure of the considered ADN and the partitioning features, there is only one connection line between any two adjacent areas. An abstract representation of a clustered network is shown in Figure 3-5. Since there is only one controllable ESS in an area, the area agent is dedicated to the related ESS which is called "ESS Agent" (EA). Each EA has a full vision on its own area with reference to the state of their related ESS unit. Area loads/generations data are used as forecast inputs. Each EA is supposed to share no information about its area with the other EAs except the information at the boundary buses. In this respect, for a given pair of adjacent areas, one of them is extended to include the boundary node of the other (in Figure 3-5, area A_h is extended to include bus g of area A_g, which is one of its neighbors). Node g is defined as the Common Boundary Bus ($CBB^{A_{h,g}}$) of both areas A_h and A_g. As a result, between any two adjacent areas one node is selected as CBB. It should be noticed that the CBB is registered within both relevant EAs.
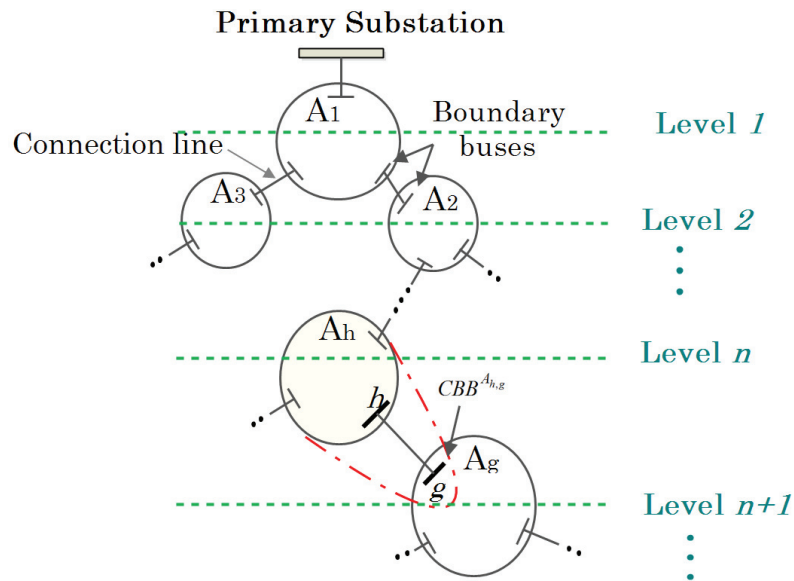
Figure 3-5 Representation of CBBs in the clustered network with the area level numbers allocation

It should be noted that in case of any changes in the topology of the network, the clustering method should be re-performed and each node can be reassigned to a new associated area. In this respect, it is worth observing that ADNs are characterized by the presence of a limited number of breakers resulting into a finite number of feasible different topologies. The distribution system operator might run the

proposed clustering algorithm offline for each of them in order to find the border of each zone for each topology.

In this part, two different decentralized scheduling methods for multi-area ADN are proposed namely, "Thévenin-based" and "Top-down sweep" scheduling methods. For both scheduling methods, the aim is to keep the area nodes voltages close to the desired values by carrying out the scheduling algorithm locally. The agent *EA* in each area determines the ESS operating point (i.e. its active, reactive power set-points) in a dedicated day-ahead scheduler with time-step of 15 minutes. The ESS set-points are determined by each *EA* without the explicit knowledge of the data of adjacent areas except the CBBs data. A major difference between the two proposed scheme is related to the interactions between *EAs* with respect to the messages exchanged.

In the "Thévenin-based scheduling method", *EA*s interact each other indirectly through a Coordination Agent (*CA*). In this respect, each *EA* provides to the *CA* a Thévenin equivalent model seen from each of its CBBs as well as the voltage value of each CBB. Based on these inputs, the *CA* takes care about the coordination between all the *EA*s tasks. It is important to notice that *CA* is not a central controller. It does not have full vision of the entire state of the network, but it has the knowledge of all the CBBs IDs and their respective computed state variables (voltages).

The "Top-down sweep scheduling method" is based on a recursive approach. The architectural model of the message exchange of this second approach is peer to peer (p2p) as any agent is able to initiate communication with its adjacent one or to be the subject of an incoming communication at any time from those adjacent agents. Therefore, unlike the previous method, *EA*s interact directly without the need for any *CA*. In this approach, a level number is assigned to each area in such a way that the area including the main slack bus of the system (primary substation) receives the level number equal to 1. All other areas are levelled from top to down successively due to the radial structure of the distribution network. Once an area gets a level number (n), the adjacent downstream areas are the next ones that are given the level numbers ($n+1$). In Figure 3-5, the allocation of the level number to each area is shown as an example. Thus, A_1 has the level number equal to 1. After that, A_2 and A_3 have the next level numbers that is 2. It is worth noting that this process relies uniquely on the radially of the system topology. Therefore, if this condition holds, it can be extended to any distribution networks including also different voltage levels (e.g. medium and low voltage grids).

In what follows, both proposed scheduling methods are explained in details.

3.2.2.2 Thévenin-Based Decentralized Scheduling Method

The general framework of this scheduling method is shown in Figure 3-6. The
algorithm is performed at each Δt (the time-step between two subsequent control
actions) by all *EA*s and *CA*. It should be noted that the load/generation forecasted
data is considered as the input for the algorithms. The proposed method relies on 5
tasks carried out in sequence. These tasks are described as follows considering a
given area A_h.
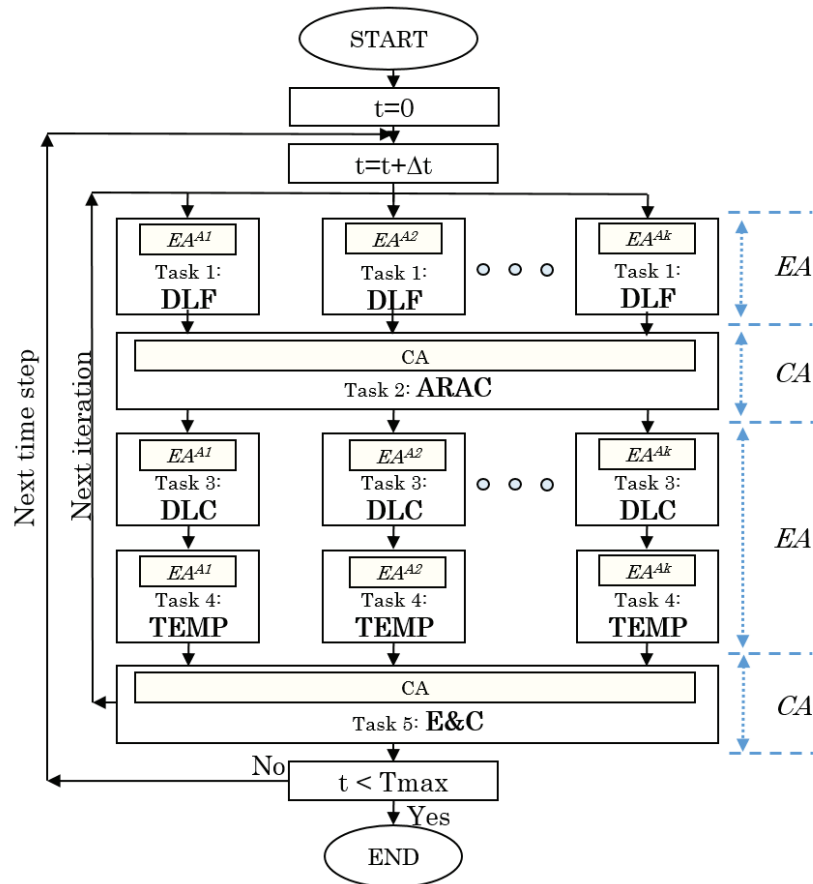
Figure 3-6 General framework of the proposed Thévenin-based scheduling method

Task 1. Distributed Load Flow (DLF) computation by *EAs*: In order to perform the local load
flow in each area, individual slack nodes are randomly selected by the EA^{A_h}. Thus, the load flow
can be performed locally. Also, the equivalent complex power at CBBs must be known. Since
this power is a priori unknown, it is computed iteratively using the process described below.

At each time-step, in the first iteration, an initial value is selected for each CBB of
an area (i.e., the initial value of the forecasted load/generation at this node). In the

subsequent iterations, this complex power is updated thanks to the voltage values resulting from task 3 and the CBBs voltages update provided by task 5.

Task 2. Area Reference Angle Corrections (ARAC) by the *CA*: In order to comply with the results derived from a centralized scheme, the *CA* need to align the voltage angles that each *EA* has obtained using its own slack bus with respect to the main slack node of the system (i.e., the primary substation). The process starts from the top area located at level 1 (since it includes the main reference node) moving towards the bottom areas in the next levels sequentially. At the initialization of this task, the top area is defined as a "principal area" and its direct neighbors as "dependent areas". Then, the difference of the voltage angles seen from the principal area and the dependent areas are computed using (3.5).

$$\Delta\delta = \delta_{CBB}^{dependent} - \delta_{CBB}^{principal} \tag{3.5}$$

Then, the voltage angle at every node in the "dependent areas" are shifted with the above-mentioned angle difference $\Delta\delta$.

$$\delta_i^{new} = \delta_i - \Delta\delta \qquad i \in \textbf{\textit{dependent area nodes}} \tag{3.6}$$

In the next steps, every previous "dependent area" becomes, in turn, a "principal area" and its direct neighbours as new "dependent areas". The procedure of angle adjustment in the "dependent areas" propagates downwards until reaching the bottommost area. It is straightforward to conclude that this process works only if the network has a radial topology.

Task 3. Decentralized Local Control (DLC) by EAs: Each EA^{A_h} has now the knowledge of its internal state inferred through the solution of the distributed load flow. Therefore, the *VSCs* can be computed for both active/reactive powers of ESS located in A_h. It is now possible to formulate a linear-programming optimal control problem (based on the knowledge of *VSCs*) in order to keep the voltage close to the desired value at each node belonging to A_h. The control variables of the optimization problems are the injected/absorbed active/reactive power of the ESS on the AC-side of their power converters (i.e., $P_{ESS}^{A_h}$ and $Q_{ESS}^{A_h}$). In general, *SoC* is used for electrochemical storage system to indicate the available amount of charge that can be extracted from the system at a given discharge rate. Therefore, this quantity does not explicitly quantify the energy reservoir level of the storage system. In this respect, it is necessary to define a State-of-Energy, SoE^{A_h}, including the energy that can be extracted from a generic storage system at any discharge rate. The energy flow is assumed to be positive during the charge and negative during its discharge. SoE^{A_h}, is defined as the remaining energy inside the device assuming, as a first approximation, a unity energy efficiency of the device.

$$SoE^{A_h}(t) = SoE^{A_h}(t-\Delta t) \pm P_{ESS}^{A_h}(t) \cdot \Delta t \tag{3.7}$$

Where $SoE^{A_h}(t-\Delta t)$ is the *SoE* in the previous time-step, Δt is the control time

interval and $P_{ESS}^{A_h}$ the output of the optimal scheduling problem (per unit). The objective function and the constraints of the optimal scheduling problem are formulated for each area as (3.8). In order to get a solution in any case, the inequality constraints associated to the lines ampacities and voltage limits at the nodes are disregarded.

$$\min_{P_{ESS}^{A_h},Q_{ESS}^{A_h}} \quad \sum_{d,t} \left\| \left| \overline{V}_{u,t}^{A_h} \right| - V_{ref}^{A_h} \right\|^2 + (SoE^{A_h} - SoE_{ref}^{A_h})^2$$

$$s.t \quad \begin{aligned} SoE_{min}^{A_h} \le SoE^{A_h} \le SoE_{max}^{A_h} \\ P_{ESS}^{A_h}{}^2 + Q_{ESS}^{A_h}{}^2 \le S_{r,ESS}^{A_h}{}^2 \end{aligned}$$

(3.8)

Where $\left| \overline{V}_{d,t}^{A_h} \right|$ is the voltage magnitude of node u in A_h at time t ($u=1,2,...,N^*$). N^* is the number of the internal buses in A_h including the CBBs, $V_{ref}^{A_h}$ and $SoE_{ref}^{A_h}$ are the voltage and SoE reference values respectively. The constraints for the optimization problem are related to the SoE^{A_h} as well as the capability curves of the power converters assumed to interface the ESS^{A_h} with the grid. In this respect, the $S_{r,ESS}^{A_h}$ is the rated power of the converter of ESS^{A_h}. The storage devices are not allowed to be charged or discharged completely. The associated limits ($SoE_{min}^{A_h}$ and $SoE_{max}^{A_h}$) are, in general, defined in order to prevent any damage to the storage system and/or reducing its lifetime.

The voltage at internal bus u could be expressed as its initial value plus a variation provided by the ESS^{A_h}.

$$\left| \overline{V}_{u,t}^{A_h} \right| = \left| \overline{V}_{u,t}^{init,A_h} \right| + \Delta \left| \overline{V}_{u,t}^{A_h} \right|$$

(3.9)

Where $\overline{V}_{u,t}^{init,A_h}$ comes from the results of DLF task. $\Delta \left| \overline{V}_{u,t}^{A_h} \right|$ is computed by the following (approximated) linear equation:

$$\Delta \left| \overline{V}_{u,t}^{A_h} \right| = VSC_{b \to u}^{P} \cdot P_{ESS}^{A_h} + VSC_{b \to u}^{Q} \cdot Q_{ESS}^{A_h}$$

(3.10)

where b is the node where ESS^{A_h} is located. So, the new voltage values for the internal buses and CBBs are provided by EAs to CA.

Task 4. Computation of Area Thévenin Equivalent Model Parameters (TEMP) by EAs: As mentioned earlier, EAs provide Thévenin equivalent models to the CA. For

a given pair of adjacent areas A_h and A_g, the corresponding $CBB^{A_{h,g}}$ divides the whole network in two distinct sub-grids containing A_h and A_g. It is considered that the $CBB^{A_{h,g}}$ is split into two virtual buses CBB^{A_h} and CBB^{A_g} associated to A_h and A_g respectively. It is assumed that each sub-grid is represented by its Thévenin equivalent model seen from the $CBB^{A_{h,g}}$ (see Figure 3-7). The voltage of the $CBB^{A_{h,g}}$ calculated for A_h is $\overline{V}_{th}^{A_{h,g}}$; while this voltage calculated for A_g is $\overline{V}_{th}^{A_{g,h}}$. From the circuit of Figure 3-7 the uniqueness of the voltage at the shared CBB can be enforced. If the calculated voltages at $CBB^{A_{h,g}}$ are different, the algorithm makes the voltage to be unique at this node using the procedure described in Task 5. The Thévenin impedance seen from $CBB^{A_{h,g}}$ regarding A_h is calculated using (3.11).

$$\overline{Z}_{th}^{A_{h,g}} = \frac{\left|\overline{V}_{th}^{A_{h,g}}\right|^2}{\overline{S}_{CBB}^{*\,A_{h,g}}} \tag{3.11}$$

This equation can be also written for A_g inverting the indices h and g. $\overline{S}_{CBB}^{A_{h,g}}$ is the equivalent apparent power flowing from A_h to A_g through $CBB^{A_{h,g}}$ which is calculated using active and reactive injection power equations as follows:

$$P_{CBB}^{A_{h,g}} = \sum_{u=1}^{N^*} \left|V_{th}^{A_{h,g}}\right|\left|V_u\right|\left|Y_{CBB^{A_h},u}\right| cos(\theta_{CBB^{A_h},u} - \delta_{CBB^{A_h}} + \delta_u) \tag{3.12}$$

$$Q_{CBB}^{A_{h,g}} = -\sum_{u=1}^{N^*} \left|V_{th}^{A_{h,g}}\right|\left|V_u\right|\left|Y_{CBB^{A_h},u}\right| sin(\theta_{CBB^{A_h},u} - \delta_{CBB^{A_h}} + \delta_u) \tag{3.13}$$

$$\overline{S_{CBB}^{A_{h,g}}} = P_{CBB}^{A_{h,g}} + j \cdot Q_{CBB}^{A_{h,g}} \tag{3.14}$$

Where N^* is the number of the internal buses in area A_h including CBBs; $\overline{Y}$ is the admittance matrix of area A_h. $\left|Y_{CBB^{A_h},u}\right|$ and $\theta_{CBB^{A_h},u}$ are the magnitude and phase of the element of the admittance matrix corresponding to row $CBB^{A_{h,g}}$ and column u. $\delta_{CBB^{A_h}}$ and δ_u are the voltage phases of $CBB^{A_{h,g}}$ and bus u respectively. For a given area the Thévenin impedance and voltage should be computed for each of its related CBBs.
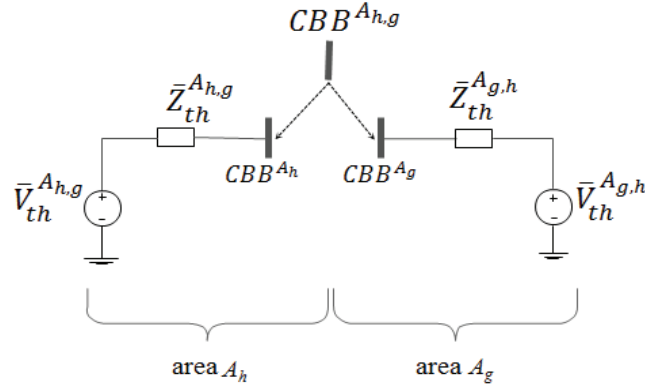
Figure 3-7 Thévenin equivalent circuit models seen from CBB

Task 5. Exchange and update of CBBs information and Convergence condition check (E&C) by CA: As mentioned earlier, for each pair of adjacent areas the voltage at the shared CBB must be unique. In other words, for a given $CBB^{A_{h,g}}$ linking A_h and A_g, the equality constraint (3.15) must be respected; where the voltages $\overline{V}_{th}^{A_{h,g}}$ and $\overline{V}_{th}^{A_{g,h}}$ are computed separately for A_h and A_g respectively by their related EAs.

$$\overline{V}_{th}^{A_{h,g}} = \overline{V}_{th}^{A_{g,h}} \tag{3.15}$$

The CA first checks for all CBBs weather (3.15) is simultaneously satisfied. If this is the case, then the decentralized scheduling at the current time t converged and the active/reactive ESSs power set-points are updated. If it is not the case, the CA forces the voltage at each CBB to be unique using (3.16). In the proposed method, the overall optimum solution is achieved iteratively.

$$\overline{V}_{th,new}^{A_{h,g}} = \overline{V}_{th,new}^{A_{g,h}} = \frac{\dfrac{\overline{V}_{th}^{A_{h,g}}}{\overline{Z}_{th}^{A_{h,g}}} + \dfrac{\overline{V}_{th}^{A_{g,h}}}{\overline{Z}_{th}^{A_{g,h}}}}{\dfrac{1}{\overline{Z}_{th}^{A_{h,g}}} + \dfrac{1}{\overline{Z}_{th}^{A_{g,h}}}} \tag{3.16}$$

a) Illustrative example of EAs and CA message exchange

In order to illustrate the message exchange process between EAs and CA, an example is presented with respect to the IEEE 13 nodes distribution test feeder shown in Figure 3-4. Bus 2 and 7 are selected as CBBs between areas A_1 and A_2 as well as areas A_1 and A_3 respectively. The Sequence diagram for communication process among CA and EAs is shown in Figure 3-8. The message exchange follows the following sequence.

Sequence 1: *EA*s perform DLF task.

Sequence 2: *EA*s send the "INFORM" message to *CA* accompanying with the calculated values for CBB voltages.

Sequence 3: *EA*s send the "REQUEST" message to *CA* asking for ARAC task.

Sequence 4: ARAC task is done by *CA* when the "REQUEST" message is received from all *EA*s. The difference of the CBBs voltage angles seen respectively from each of the areas are computed as (3.17).

$$\Delta\delta_2 = \delta_2^{A_2} - \delta_2^{A_1} \quad ; \quad \Delta\delta_7 = \delta_7^{A_3} - \delta_7^{A_1} \qquad\qquad (3.17)$$

Sequence 5: *CA* sends "INFORM" message with the content of the value of the calculated $\Delta\delta_2$ and $\Delta\delta_7$ to EA^{A_2} and EA^{A_3} respectively.

Sequence 6: *CA* sends "REQUEST" messages to all *EA*s asking for DLC and TEMP tasks.

Sequence 7-8: *EA*s perform DLC and TEMP tasks.

Sequence 9: *EA*s send "INFORM" messages to *CA* with the content of the updated values of CBBs voltages.

Sequence 10: *EA*s ask for E&C check task by sending the "REQUEST" message to *CA*.

Sequence 11: *CA* performs E&C task. If the differences of the CBBs voltages calculated by adjacent areas are equal to zero, the procedure goes to the next time step at sequence 14. If this is not the case it goes to sequence 12.

Sequence 12: *CA* sends "INFORM" message to *EA*s allowing them to know the updated value of CBB voltages.

Sequence 13: *CA* asks the *EA*s for the DLF task by sending the REQUEST message and the procedure goes to sequence 1.

Sequence 14: *CA* sends CONFIRM message to *EA*s to let them know about the convergence of the current time-step.

The main feature of the proposed method is the independence of the scheduling scheme for each area and the possibility for any area to join into or move back from the proposed scheme. However, the main drawback is that the process requires the presence of the *CA*.
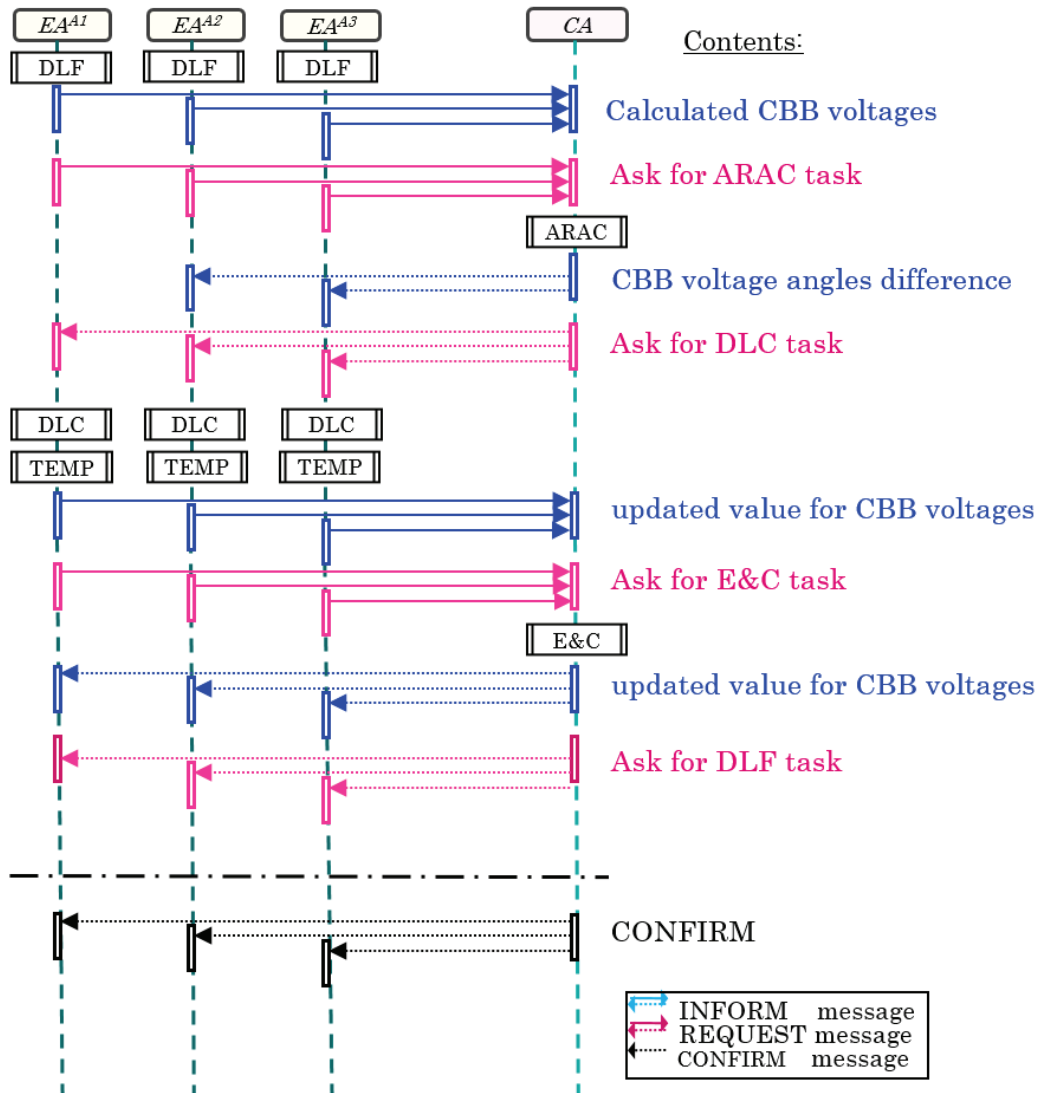
Figure 3-8 Sequence diagram for communication procedure for Thévenin-based scheduling method

3.2.2.3 Top-Down Sweep Scheduling Method

The second proposed scheduling algorithm is a recursive one. In this approach, CBBs are considered as the area slack nodes except the area including the physical slack bus of the system (i.e., the primary substation). For the area with more than one neighbour, the CBB between the area and the adjacent neighbour located at the lower level is selected as the slack bus. First, the approach propagates the Area Local Voltage Control (ALC) from the area located at level 1 towards the peripheral ones. In this propagation, the slack node voltage of a given area at the generic level n is imposed by the unique adjacent area at level n-1. Then, the algorithm moves from the bottommost areas to the level 1. In this backward motion, the supply-demand

power mismatches of a given area (including also the internal area power losses) are transferred sequentially to the main slack node connected to the physical slack.

This process is repeated until the calculated injected power at the main slack node of the system converges to a fixed value. The ALC relies on four tasks. For a given area A_h:

Task 1: Perform distributed load flow: The *EA*s perform a distributed load flow considering the slack node voltage as indicated earlier as well as the transferred powers calculated from the adjacent areas located at the higher level (see Task 4).

Task 2: VSCs computation: VSCs are computed for both active/reactive powers of ESS^{A_h} .

Task 3: Control of area nodes voltages: The local voltage control method is the same used in Thévenin-based decentralized scheduling method (i.e., obtained using (3.8)-(3.10)).

Task 4: Computation of the area internal power mismatches: As known, main slack node is responsible for providing the power to compensate the losses and the supply-demand mismatches of the system. Since several slack nodes are considered, sharing these mismatches by all the area slack nodes should be avoided. In fact, the area slack nodes are virtual ones that enable *EA*s to perform the local distributed load flow. Therefore, the area losses, as well as the area supply-demand power mismatches, must be transferred to the real slack node of the system (in general the primary substation). In this respect, each area computes these powers in correspondence of the virtual slack node. So for area A_h, the slack node powers are computed using (3.18).

$$P_s^{A_h} - jQ_s^{A_h} = \overline{V}_s^{*A_h} \cdot (\overline{V}_s^{A_h} \sum_{\substack{j=1 \\ j \neq s}}^{N^*} \overline{Y}_{sj}^{A_h} - \sum_{\substack{j=1 \\ j \neq s}}^{N^*} \overline{V}_j^{A_h} \cdot \overline{Y}_{sj}^{A_h}) \qquad (3.18)$$

where $\overline{V}_s^{A_h}$ is the voltage of the A_h virtual slack node and N^* is the number of internal nodes in A_h including CBBs. $\overline{Y}_{sj}^{A_h}$ is the element of the admittance matrix of A_h corresponding to row s (slack) and column j. This calculated power is added to the CBB of the adjacent area located at the lower level as a load.

a) Illustrative example on message exchange

In this method, the architectural model of the MAS is p2p. The *EA*s decisions are based on local information as well as those provided by neighbour *EA*s. In particular, a specific agent, say EA^{A_h} , has access to the following set of information:

$$EI^{A_h} = \left[n^{A_h}, \gamma^{A_h}, \Gamma^{A_h} \right] \qquad\qquad (3.19)$$

$$N^{A_h} : \left\{ \mathcal{G}^{A_{h,l}} \right\}; \qquad \mathcal{G}^{A_{h,l}} = \left[n^{A_l}, V_{CBB}^{A_l}, S_s^{A_l} \right] \qquad\qquad (3.20)$$

Where n^{A_h} is the level number of the considered EA^{A_h}; Γ^{A_h} is the set of internal state of the area A_h (in particular, nodes voltages, losses, etc.); $S_s^{A_l}$ is losses plus supply-demand power mismatches in the considered area A_l. $V_{CBB}^{A_l}$ is the voltage of the CBB node between area A_h and A_l and γ^{A_h} is EA^{A_h} status which has two modes; named *SL* and *LS* whose meaning is given by the proposition here below. Based on the level number and the area current status, a given *EA* defines which adjacent *EAs* to communicate with and which information should be exchanged, using the following proposition.

Proposition #1 – *A given area with the current status of SL at level χ can communicate only with the adjacent areas with the level number χ+1 and the exchanged information between them is the voltages of the related CBBs. The area with the current status of LS at level χ can just communicate with the only adjacent one with the level number χ-1; and the exchanged information between them are the area losses and the area power mismatches.*

Each area changes its status considering the received information from the adjacent ones. Receiving updated values for slack node voltage results in *SL* mode; while receiving updated values for S_s computed by(3.18), results in *LS* mode. It should be noted that the *EA*s located at the lowest and highest levels in the system do not change their statuses since they are always with *SL* and *LS* statuses respectively. In addition, the updated S_s values should be received from all adjacent *EA*s with *LS* status in order to let the specific *EA* fulfills its tasks.

At the current time *t*, the Top-down sweep scheduling method starts the process from the area with the level equal to 1. Then, the algorithm pursues the following general procedure for a given area A_h at level n.

Step 1: the area local voltage control (ALC) is performed by EA^{A_h}. The set *EI* defined by (3.19) is updated.

Step 2: based on the current status, the EA^{A_h} sends the INFORM messages to the applicable adjacent *EA*s. If its status is *SL*, each message is sent to a *EA* at level n+1 with the content of the corresponding CBB voltage. If the status is *LS*, the message is sent to the only *EA* at level *n-1* along with the content of S_s. Each INFORM

message is accompanied by a REQUEST message asking for performing the local voltage control.

Step 3: The adjacent *EA* which receives the REQUEST message changes its status based on the received information. If it receives an update on the slack node voltage (CBB), the status become *SL*; while, if it receives the update on CBBs powers, the status become *LS*. Furthermore, it updates its neighboring agent set *N* considering the information provided by the *EA*s that send the REQUEST messages.

Step 4: if the *EA* that receives the REQUEST message is A_1, the algorithm convergence criterion is checked. The convergence criterion is based on the active/reactive powers injected from the main primary substation. EA^{A_1} checks the powers variations of the main slack node with respect to the former values from the previous iteration. If this variation is lower than a specific threshold, the distributed control at the current time t converges. If this is not the case, the algorithm goes to step 1.

In order to demonstrate the message exchanges between *EA*s for the sweep top-down scheduling method, an example is presented using the same IEEE 13 nodes distribution test feeder of Figure 3-4. As before, an *EA* is assigned to each ESS. Bus 2 and 7 are selected as CBBs. These buses are the slack nodes for area A_2 and A_3 respectively. A_1 is located at level 1 since it includes the main slack node of the system. A_2 and A_3 are located at the same level 2.

For a generic time t, EA^{A_1} performs the ALC task and it updates its own three-tuple (3.19) as: $EA^{A_1} : \left\{ 1, SL, \Gamma(t)^{A_1} \right\}$. Since EA^{A_1} has the *SL* status mode, it sends the INFORM message along with the obtained values for $V_2(t)^{A_1}$, $V_7(t)^{A_1}$ to A_2 and A_3 at level 2. Afterward, EA^{A_1} sends the REQUEST message to A_2 and A_3 and asks them to perform the ALC task. EA^{A_2} and EA^{A_3} receive the REQUEST message from A_1 with the updated values for their slack nodes voltages. Normally, the A_2 and A_3 status (γ^{A_2} and γ^{A_3}) should be changed to become similar to γ^{A_1}. However, since EA^{A_2} and EA^{A_3} have the highest level numbers, they are not able to change their status from *LS* to *SL*. The sets N^{A_2} and N^{A_3} are updated considering the received information from A_1: $N^{A_2} : \left\{ \left[1, V_2(t)^{A_1}, S_s(t)^{A_1} \right] \right\}$, $N^{A_3} : \left\{ \left[1, V_7(t)^{A_1}, S_s(t)^{A_1} \right] \right\}$. Then, EA^{A_2} and EA^{A_3} perform the ALC task locally. They update their own three-tuples (3.19) as $EA^{A_2} : \left\{ 1, LS, S_s(t)^{A_2}, \Gamma(t)^{A_2} \right\}$, $EA^{A_3} : \left\{ 1, LS, S_s(t)^{A_3}, \Gamma(t)^{A_3} \right\}$.

Subsequently, EA^{A_2} and EA^{A_3} send the INFORM message along with the computed values for $S_s(t)^{A_2}$, $S_s(t)^{A_3}$ to EA^{A_1} which is located at the lower level. Once EA^{A_1} receives the INFORM messages from all the adjacent *EA*s at higher levels, it updates

its neighboring agent set: $N^{A_1}:\left\{\left[2,V_2(t)^{A_2},S_s(t)^{A_2}\right],\left[2,V_7(t)^{A_3},S_s(t)^{A_3}\right]\right\}$. EA^{A_2} and EA^{A_3} also send the REQUEST message to EA^{A_1} asking for the ALC task. The computed losses and power mismatches $S_s(t)^{A_2}$ and $S_s(t)^{A_3}$ are added to the load of bus 2 and bus 7 respectively before performing the ALC task. Since the ALC is to be performed by EA^{A_1} located at level 1, the convergence condition must be checked. In this respect, the EA^{A_1} verifies the main slack node injected power variations with reference to its previous value. If the variation is less than an acceptable threshold, the decentralized Top-down sweep scheduling is converged. Otherwise, the process continues until the convergence condition is met.

3.2.3 Performance Evaluation

The performance evaluation of the two methods is carried out by using a case study. For the sake of benchmarking the 123 IEEE test grids [158] is used. However, the network loads and PV injections are inferred from experimental data observed on a real ADN located in the southeast region of Switzerland. Non-dispatchable PV units are connected to the system. Their power injections are represented by voltage-independent active power injections with the null reactive component[1]. The network loads are considered as voltage independent PQ absorptions. The lines are modelled using the classical equivalents. Thus, the reactive power associated to shunt impedance of the lines is also considered. The schematic of the system, as well as the zone decomposition obtained using the method presented in section II, is shown in Figure 3-9. The two proposed scheduling methods are applied in the system considering five ESSs.

---

[1] It should be noted that reactive power compensation from only PV inverters could be sufficient to keep the acceptable voltage profiles only in network with low R/X ratios of longitudinal line impedance parameters, whereas in ADNs normally the feeder R/X ratio might be high. Moreover, the operation of PV inverters with non-unity power factor will result in lower active power production [171]. As a result, in this paper it is considered that the control of the grid is obtained only using ESSs.
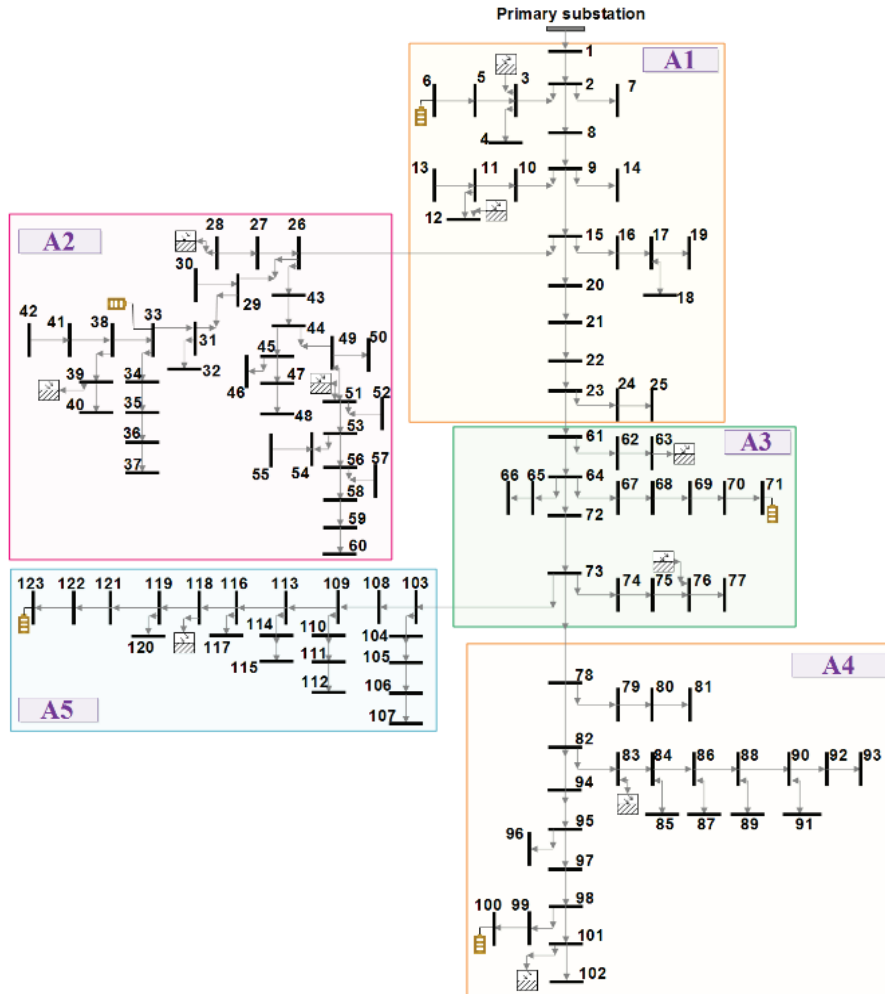
Figure 3-9 Clustered IEEE 123 nodes test system

3.2.3.1 Distributed Load Flow Solution in Thévenin-Based Method

As a consequence of the network partitioning, buses 23, 26, 72, 73, are considered as CBBs. In order to validate the computation of the network equivalents, Figure 3-10 shows the CBB voltage profiles in a given day with no ESS contribution. In particular, Figure 3-10 compares the CBBs voltage magnitudes computed by a fully centralized vs a decentralized load flow accounting for the network equivalents. Figure 3-11 indicates the largest error of voltage amplitude of each CBB at each iteration of Thévenin model update for a specific time. It reflects the convergence of the process during the iterations. In this respect, Figure 3-11 also shows the number of times a given load-flow needs to be computed for a given control action. It can be seen that the method converges in few iterations.
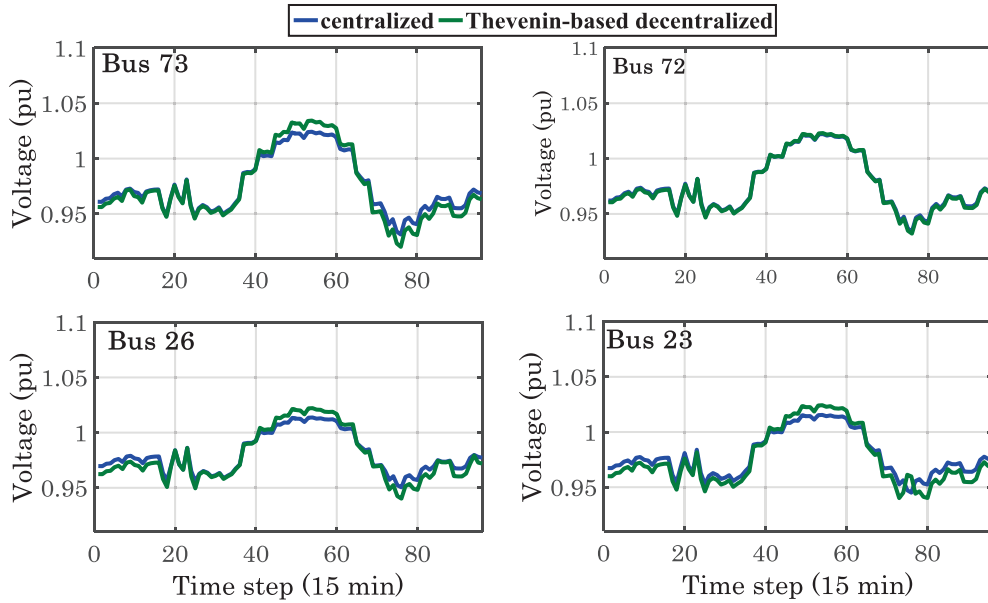
Figure 3-10 CBB voltage profiles with no ESS control actions: comparison between a fully-centralized load flow and a local load flow with Thévenin equivalents method
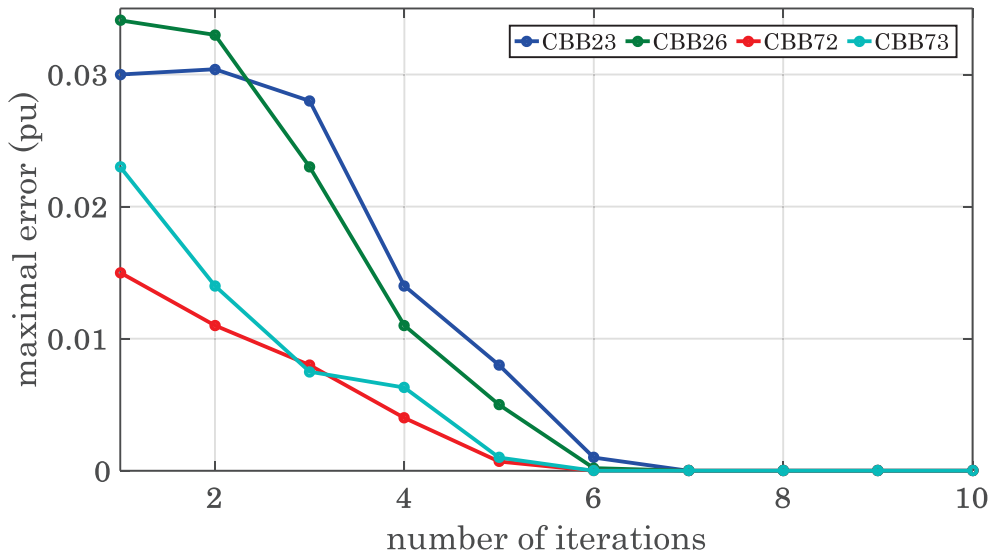
Figure 3-11 Maximal error of voltage amplitude of each CBB for each iteration of Thévenin model update

3.2.3.2 Distributed Load Flow Solution in Top-Down Sweep Method

Figure 3-12 shows the largest error of the transferred losses among areas in each iteration for a given time-step (i.e., for a given control action). The subsequent downtrend of all curves shows the convergence of the proposed method, properly. It

also shows the number of times that a given load-flow needs to be computed for a given control action. Also, in this case it can be seen that the method converges in few iterations.
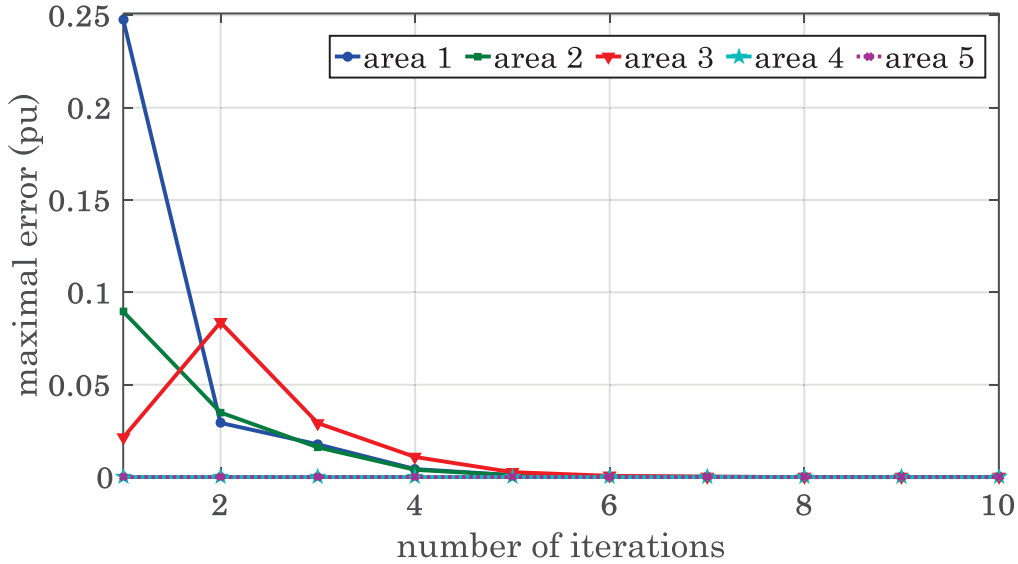
Figure 3-12 Maximum errors of transferred losses among areas for each iteration of the Top-down sweep scheduling method

3.2.3.3 Performance Assessment

In order to show the performances of the two methods concerning the improvements in the voltage profiles, they are compared with the equivalent centralized scheme. In all the simulations, the optimization problem is solved using the YALMIP optimizer [159] and Gurobi optimization software [160]. Figure 3-13 shows the maximum, minimum and mean values of all the network node voltages for each 15-minutes period of the day, for the following cases: i) no control on ESSs, ii) centralized scheme, iii) Thévenin-based decentralized and iv) Top-down sweep decentralized scheme. As it can be seen, both decentralized scheduling methods provide almost the same voltage improvements compared to the centralized scheme. As expected, the proposed decentralized methods lead to slightly worst voltage profiles in comparison with the centralized one since they do not account for *VSC* associated to ESSs located in areas other than the targeted one. However, they always allow limiting the voltage deviations within the range and avoiding the need of sharing all the network data.
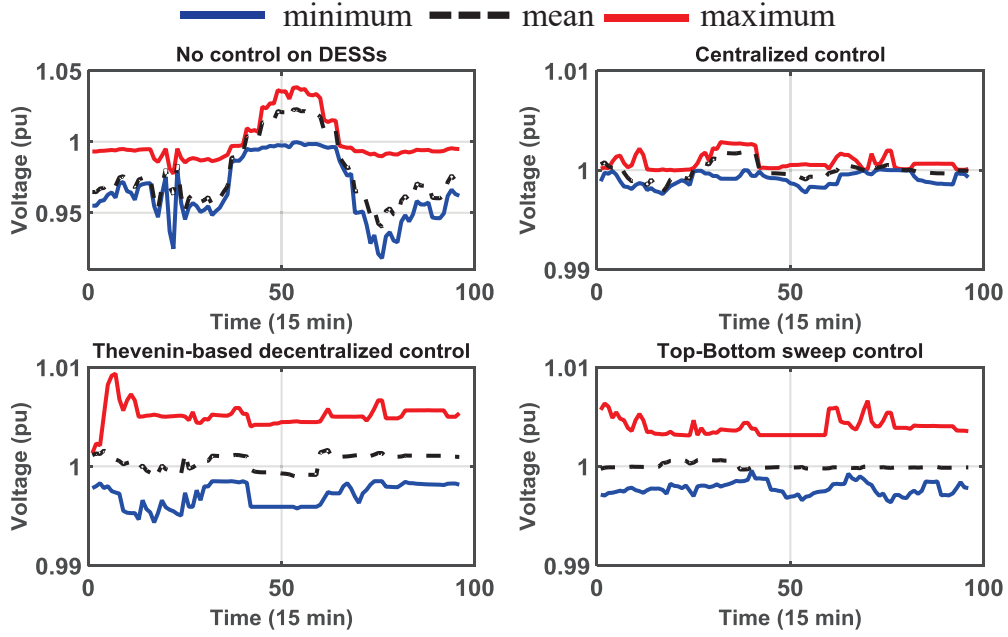
Figure 3-13 Distribution of all node voltages for i) no control, ii) centralized scheme, iii) Thévenin-based decentralized scheduling scheme   and iv) Top-down sweep decentralized scheduling scheme (the time is discretized with a 15 minutes' interval)

The root-mean-square error (RMSE) between centralized and decentralized approaches is calculated using (3.21), for one-year voltage profile for all buses of the system. The results are shown in Figure 3-14.

$$RMSE = \sqrt{\frac{\sum_{t}^{T_{max}} \sum_{i=1}^{N} (V_{centralized}(i,t) - V_{decentralized}(i,t))^2}{N}} \tag{3.21}$$

It can be seen that the RMSE differences for the centralized vs. decentralized schemes are in the order of 0.2%. By comparing the results shown in Figure 3-13 and Figure 3-14 associated to the two decentralized method, it can be seen that the Top-down sweep scheduling method performs slightly better than the Thévenin-based one. As a matter of fact, the use of the network equivalents involves the approximated representation of the external areas using, indeed, a linearized model represented by the network equivalent itself.

In order to have a more comprehensive comparison of the proposed methods, the scenarios referring to two different days in summer and winter are considered. Figure 3-15 shows the empirical CDFs of the difference of the bus voltages obtained by the centralized algorithm and the two proposed decentralized ones. Also in this

case, it is observed that the behavior of the Top-down sweep scheduling method is closer to the centralized one rather than the Thévenin-based method.
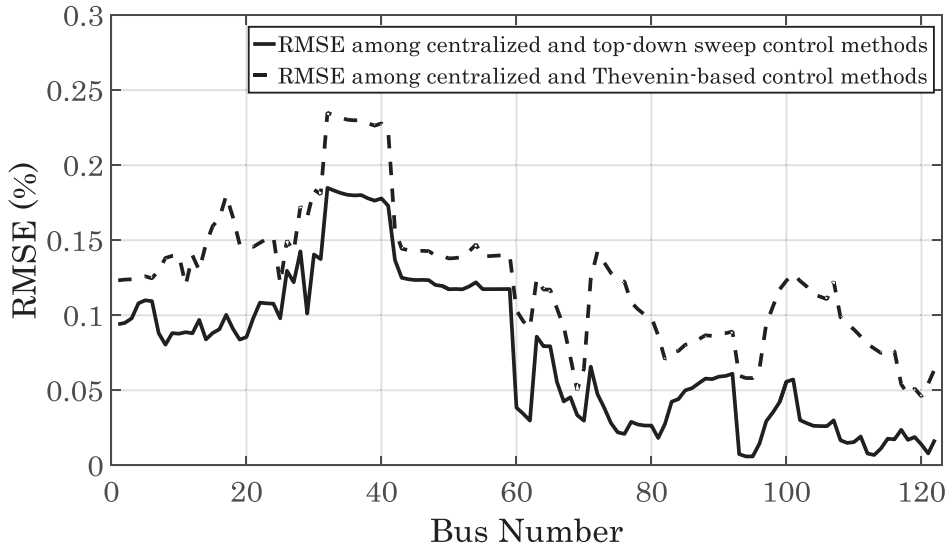
Figure 3-14 RMSE between centralized and decentralized approaches
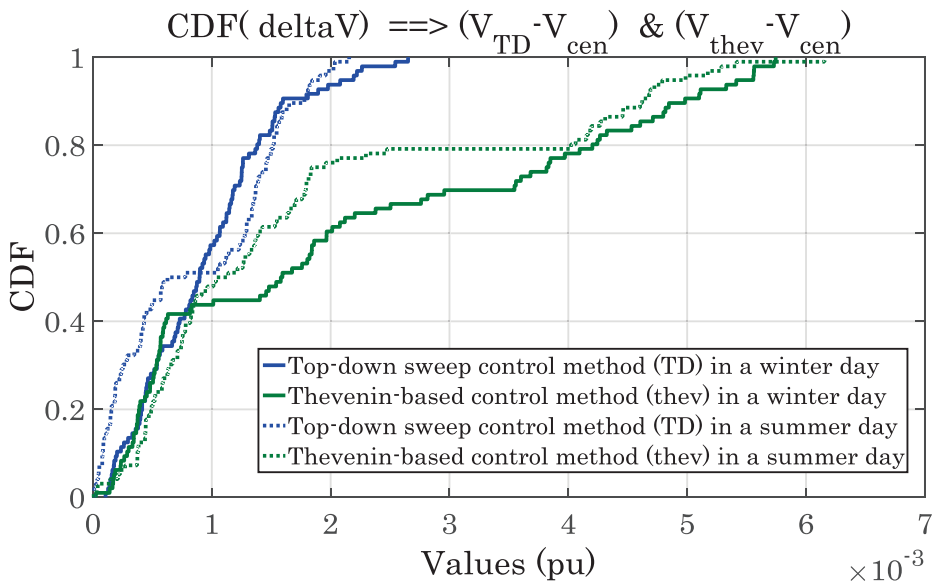
Figure 3-15 CDF of the difference of the bus voltages obtained by the centralized and the two proposed decentralized scheduling methods for two days in summer and winter

Figure 3-16 and Figure 3-17 shows the CDFs of the differences between the active and reactive power set-points of ESSs obtained by centralized scheme and the two proposed ones for both scenarios. It is seen that the active/reactive power set-points of ESSs in Top-down sweep method are also closer to those in the centralized one than those in the Thévenin-based one.
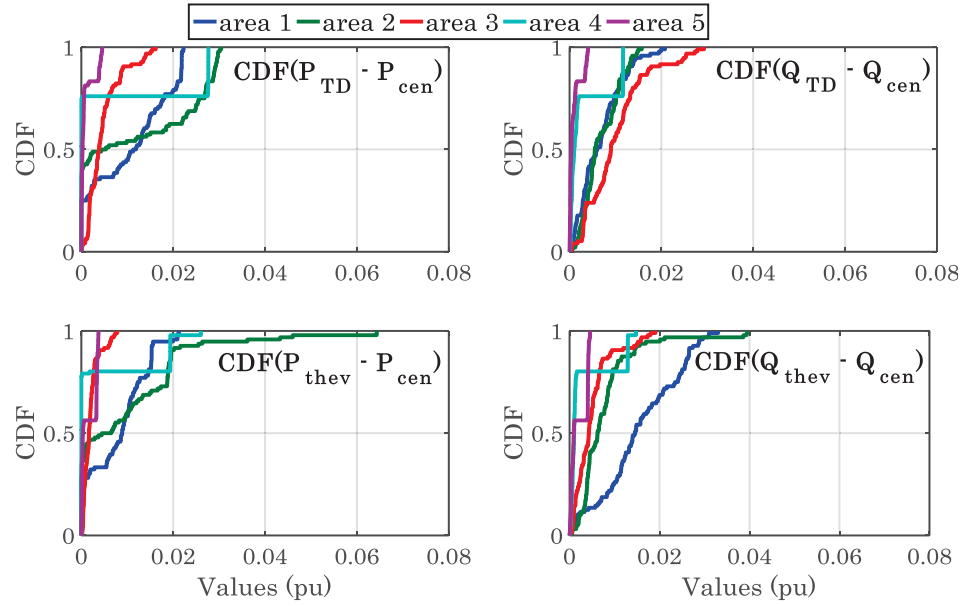
Figure 3-16 CDFs of the difference between the active/reactive power set-points of ESSs obtained by Centralized (cen) and Thévenin-based (thev) / Top-down sweep (TD) methods for a day in winter.
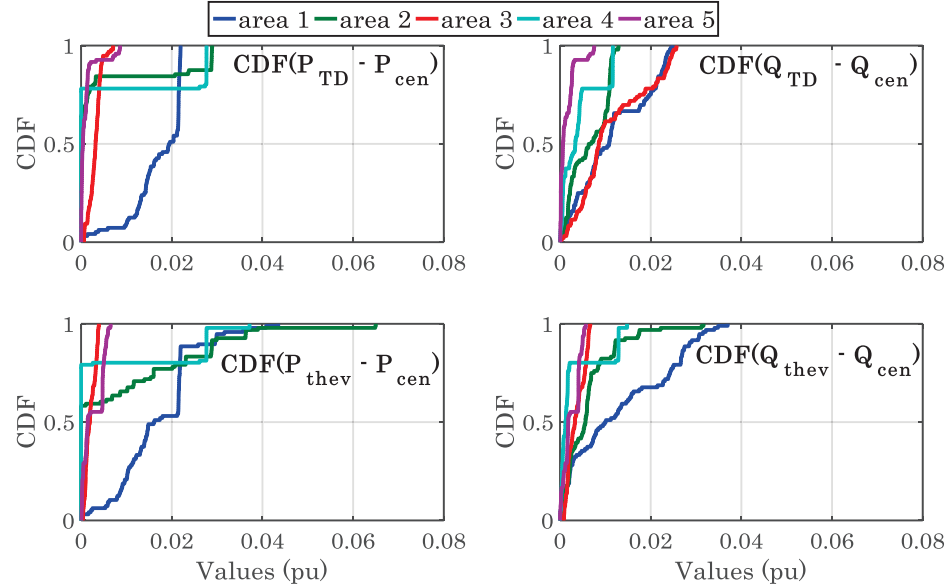
Figure 3-17 CDF of the difference between the active/reactive power set-points of ESSs obtained by Centralized (cen) and Thévenin-based (thev) / Top-down sweep (TD) methods for a day in summer

The computational time is calculated for centralized and the two proposed decentralized method for a given day. The results is shown in Figure 3-18. As expected, it is seen that the decentralized schemes relieve the computational burden

since the amount of information to be centrally treated would considerably decrease. This computation time has been achieved on a workstation equipped with a 2.7 GHz quad core INTEL i7 processor, 8 GB of RAM running the Matlab® computation environment.

3.2.3.4 Optimality

It should be pointed out that the centralized problem in our case is a convex optimization problem which always leads to a global optimal solution. Linear programming technique using voltage sensitivity coefficients are used for this purpose. Although the two proposed decentralized algorithms are of heuristic nature providing sub-optimal solutions, they are very close to those of the equivalent centralized problem (see Figure 3-14). In addition, the convergence of the two proposed algorithms are shown in Figure 3-11and Figure 3-12 for a grid with 123 nodes that exceed the size of typical distribution networks.

3.2.3.5 Agent Exchanged Messages

The number of exchanged messages for both proposed decentralized algorithm are shown in Figure 3-19 for an entire year. It can be seen that the number of messages exchanged among the *EA*s in the Top-down sweep scheduling method is much lower than the ones in the Thévenin-based scheduling method.
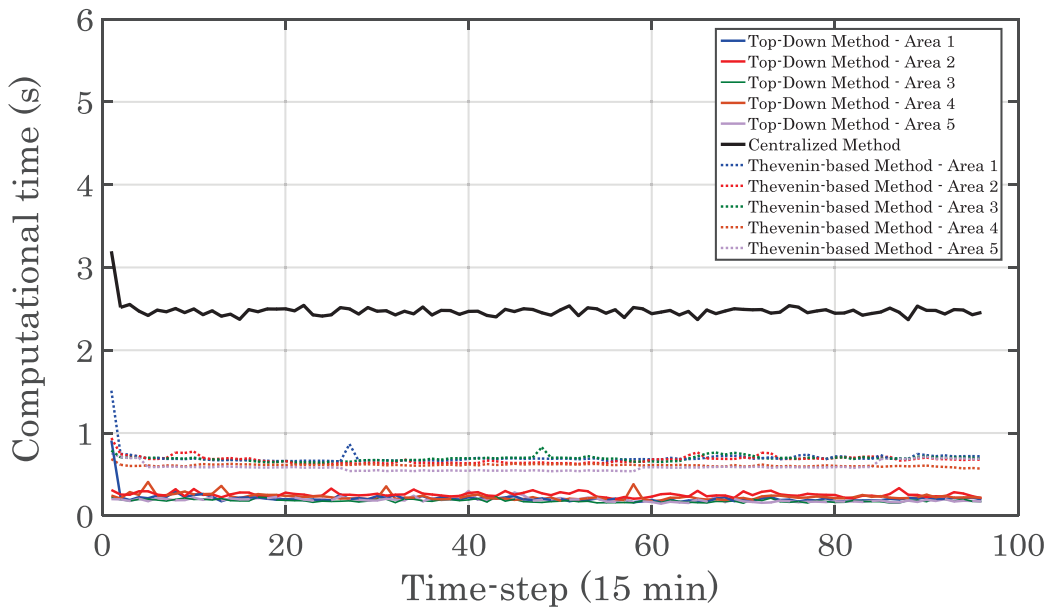
Figure 3-18 Computational time burden comparison between Centralized and the two proposed decentralized method for a given day
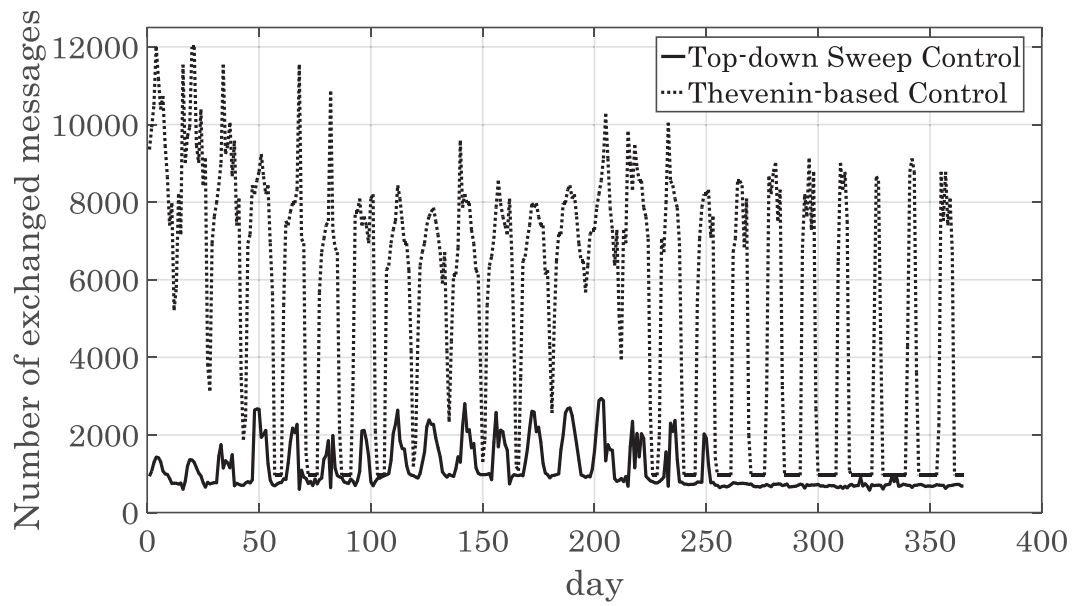
Figure 3-19 Number of exchanged messaged per time interval (i.e., 15 min) for both proposed decentralized method along an entire year

Part III. Decentralized Adaptive Model-Based Real-Time Control for Active Distribution Networks Using Energy Storage Systems

This part proposes a real-time decentralized control algorithm in multi-area ADNs relying only on distributed BESSs. In particular, we propose a zonal control strategy targeting voltage support and line congestion management. The proposed zonal control relies on an accurate dynamic model of BESSs capable to account for their DC active power limits. For this purpose, an experimentally-fitted two-time constant (TTC) dynamic model presented in chapter 2 for Lithium-based battery is used. An agent is assigned to each area and MAS is used for implementing the communication among different areas.

This part is structured as follows: Section III.1 presents different existing control methods for ADNs. Section III.2 reviews the two BESS model presented in chapter II (CR and TTC models). The formal computation of DC active power of the BESS is presented in this section. Section III.3 proposes the decentralized grid control strategy including voltage control and congestion management based on the BESS dynamic model presented in III.2. Section III.4 illustrates the performance evaluation of the proposed control method with reference to the IEEE 13 node test distribution feeder.

3.3.1 Review of Existing Decentralized Real-Time Control Methods

Due to the increasing penetration of DGs, the issue of voltage regulation of ADNs becomes more significant. Several methods have been proposed in the literature to overcome this issue including centralized and decentralized schemes [161]. [129] proposed a centralized primary voltage control using real-time demand response broadcast low-rate communication signal. Also, it used the same broadcast signal deployed for controlling loads to manage the distributed storage. Decentralized voltage control using the DGs' inverters has been proposed, for instance, in [13], [14], [162], [163], [164]. However, the optimal coordination of hundreds of inverters might require a complex telecommunication infrastructure leading to high investment costs. In addition, the active power control by DGs might be not permitted due to the existing grid code for prosumers. Thus, in the network characterized by high ratios' R/X of longitudinal line impedances, the reactive power compensation relying on those DGs' inverters could not be sufficient to achieve satisfying grid control. Moreover, the coordination strategy between agents are centrally treated by registering all the agents in a common directory. [165] used On-Load Tap Changing method in order to control the grid voltages in a distributed manner. However, the structure of the feeders affects the effectiveness of this method significantly. In [5] different agents are proposed for each DG, bus, load, and feeder. Thus, the

distribution system operator should install extra controllers/agents in some specific buses which impose extra investment costs. In addition, none of the presented works account for the dynamic behaviour of the controlled devices.

In this work, a novel decentralized real-time control is presented using the clustering technique presented in part II. It is assumed that each area is controlled by the controller associated to its corresponding ESS. With this assumption, the influence of the DGs on the grid is indirectly regulated by the controllers already available at the ESSs. The peculiarity of distributed control in multi-area systems is that the internal state of each area is not shared with the others.

In a previous work [166], the author of this thesis has proposed a control process where ESSs is used for the grid control. In that work, the ESSs have been modeled as ideal energy reservoirs and their dynamic behavior was not taken into account. In this part, an adaptive model-based control (MBC) relying on the accurate dynamic representation of BESSs is proposed. For this purpose, an experimentally-fitted two-time constant dynamic model of Lithium-Titanate battery, is used. For this purpose, at each time step, the controller solves a control optimal problem and it determines a feasible BESSs operating points (i.e. their active/reactive power set-points) with a refresh rate that, for instance, can be of hundreds of ms. Then, assuming to know the *SoE,* the controller computes the operative bounds of the BESSs in terms of DC active power limits for the next time step. These bounds are included as constraints in the control optimization problem.

3.3.2 BESS Dynamic Models

Since BESSs are supposed to be the only controllable devices of the ADN regulator, their modeling will inherently influence the feasibility and optimality of the regulator actions. In this respect, the detailed two BESS models (CR and TTC models) presented in chapter 2 part III are used and compared to compute the real-time power output constraints of the BESS. These constraints are considered in the real-time MBC algorithm.

3.3.2.1 Charge Representative Model (CR)

This type of model (e.g., [29]) does not account for the internal charge flow and diffusion processes of battery cells. Instead, it considers the cell as an ideal reservoir of charge and energy. As mentioned before, the *SoC* does not explicitly quantify the energy reservoir level of the storage system. Therefore, *SoE* is used to indicate the energy that can be extracted from a generic storage system at any discharge rate. *SoE* is defined with a unity energy efficiency of the device using (3.22).

$$SoE(t) = SoE(t_0) + \int_{t_0}^{t} \frac{P_{BESS}^{dc}(\tau)}{E_{nom}} d\tau \qquad (3.22)$$

As a result, BESSs are represented as an ideal energy reservoir. No dynamics of the
BESS are considered and, therefore, its constraints are only the *SoE* upper and lower
bounds. It is interesting to observe that, since there is no voltage dynamic accounted
in this model, charge and energy are equivalent quantities.

3.3.2.2 BESS TTC State Space Model

The most common electrical model of Lithium-based electrochemical cell is based on
the adoption of an equivalent Thévenin-circuit (e.g., [118]). As shown in chapter 2
and Figure 3-20, this model is composed of two RC time constants (see chapter 2-
part III for more details). Since it is considered that the delivered/absorbed charge
of the battery changes continuously due to the real-time voltage controller, the effect
of the redistribution phenomena can be neglected.
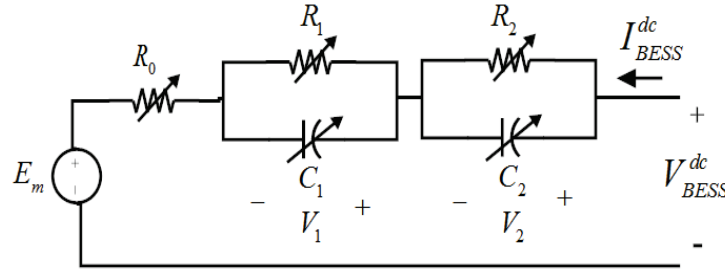
Figure 3-20 BESS TTC model

From the TTC equivalent circuit shown in Figure 3-20, it is possible to derive the
state space model (3.23)-(3.25) expressed as a function of two state variables
$X = [V_1, V_2]^T$, I_{BESS}^{dc} as the only input and V_{BESS}^{dc} as the only output.

$$\begin{cases} \dot{V}_1 = \dfrac{-1}{R_1 C_1} V_1 + \dfrac{1}{C_1} I_{BESS}^{dc} \\[2mm] \dot{V}_2 = \dfrac{-1}{R_2 C_2} V_2 + \dfrac{1}{C_2} I_{BESS}^{dc} \\[2mm] V_{BESS}^{dc} = V_1 + V_2 + R_0 I_{BESS}^{dc} + E_m \end{cases} \qquad (3.23)$$

$$\begin{cases} \dot{X} = \mathbf{A} X + \mathbf{B} I_{BESS}^{dc} \\[2mm] V_{BESS}^{dc} = \mathbf{C} X + \mathbf{D} I_{BESS}^{dc} \end{cases} \qquad (3.24)$$

$$\mathbf{A} = \begin{bmatrix} \dfrac{-1}{R_1 C_1} & 0 \\[2mm] 0 & \dfrac{-1}{R_2 C_2} \end{bmatrix}; \quad \mathbf{B} = \begin{bmatrix} \dfrac{1}{C_1} \\[2mm] \dfrac{1}{C_2} \end{bmatrix}; \qquad (3.25)$$

$$\mathbf{C} = \begin{bmatrix} 1 & 1 \end{bmatrix}; \quad \mathbf{D} = \begin{bmatrix} R_0 \end{bmatrix}; \qquad V_{BESS}^{dc}(0) = Em$$

The energy flow is assumed to be positive during the charge and negative during the cell discharge. All the cell parameters depend on the *SoE* as well as on Crate. For this reason, matrices **A**, **B**, and **D** need to be experimentally fitted for different *SoE* using the process described in chapter 2.

Formal Computation of the BESSs DC Power Constraints

The computation of DC power here is inspired from the work presented in [167] for the case of electrochemical double layer supercapacitors. The active power of BESS cell is calculated by (3.26) at each time step.

$$P_{BESS}^{dc}(t) = V_{BESS}^{dc}(t) \times I_{BESS}^{dc}(t) \qquad (3.26)$$

The power of the BESS changes dynamically with the *SoE* since the parameters of the TTC are function of this quantity. For this purpose, the following assumptions are made:

- Parameters of the TTC model are known and obtained by means of the process described in chapter 2 as a function of the *SoE*.

- The battery cells are arranged in suitable parallel and series connections to form an array of a given total energy and power capacities such that the status of one cell identifies the entire array.

- The maximum of $P_{BESS}^{dc}(t)$ is associated to the cell charge (positive value) and its minimum to the cell discharge (negative value). It is obvious that the limits for the BESS DC power change dynamically with *SoE*.

It is assumed that the update rate of the battery set-points imposed by the controller is small enough ($\Delta t = 100ms$), thus *SoE*, and, consequently the battery parameters, can be considered constant between two consecutive set-point computations. This assumption is reasonable in view of the typical large size of BESS resulting from optimal planning problems. It is worth observing that AC active/reactive set-points

of the BESS are kept constant between two subsequent updates of the controller set-points. Therefore, by knowing SoE at time $t - \Delta t$, the SoE for the next time t is computed using (3.22). At time $(t - \Delta t)$, a set of all feasible DC power set-points for the next time interval $([t - \Delta t, t])$ are computed accounting for minimum/maximum $V_{BESS}^{dc}(t)$, $I_{BESS}^{dc}(t)$ and $SoE_{BESS}(t)$ (i.e., $V_{BESS}^{dc,min}, V_{BESS}^{dc,max}, I_{BESS}^{dc,min}, I_{BESS}^{dc,max}, SoE_{BESS}^{min}, SoE_{BESS}^{max}$).

Using (3.25) and (3.26), the $V_{BESS}^{dc}(t)$ is computed as a function of $P_{BESS}^{dc}(t)$ for the current time t using (3.27).

$$V_{BESS}^{dc}(t) = f\left(P_{BESS}^{dc}(t)\right) = \frac{(\mathbf{C}X) \pm \sqrt{(\mathbf{C}X)^2 + 4\mathbf{D}P_{BESS}^{dc}(t)}}{2} \tag{3.27}$$

Since we assume that the BESS power flow is positive during its charge and $V_{BESS}^{dc}(t)$ is always positive, the only feasible solution of (3.27) for the charging phase is the one linked to the positive sign of the square root. For the discharge (negative power flow), both solutions linked to the positive and negative signs might give positive $V_{BESS}^{dc}(t)$. As known, the battery DC voltage has continuous behavior. Thus, the continuity should stand also on the zero crossing of the BESS power flow (from charge to discharge or vice versa). As a result, charging with a small amount of positive DC power (ε^+) gives the same amount of DC voltage as for the case of discharging with small amount of negative DC power (ε^-).

$$V_{BESS}^{dc}\left(t\bigg|_{P_{BESS}^{dc}(t)=\varepsilon^+}\right) = V_{BESS}^{dc}\left(t\bigg|_{P_{BESS}^{dc}(t)=\varepsilon^-}\right) \tag{3.28}$$

Since $V_{BESS}^{dc}\left(t\bigg|_{P_{BESS}^{dc}(t)=\varepsilon^+}\right) = \mathbf{C}X$, the only acceptable solution for the discharge phases is the one linked to the positive sign likewise the charging case.

To sum up, with a unique value of P_{BESS}^{dc}, there is one and only one feasible solution for V_{BESS}^{dc} given by (3.29).

$$V_{BESS}^{dc}(t) = \frac{(\mathbf{C}X) + \sqrt{(\mathbf{C}X)^2 + 4\mathbf{D}P_{BESS}^{dc}(t)}}{2} \tag{3.29}$$

Matrices $\mathbf{C}$ and $\mathbf{D}$, as well as the system state X, are related to the current time-step. However, for the sake of simplicity, the index of time is removed. Note that the square root in (3.29) results in finding the critical DC power computed by (3.30).

$$P_{BESS}^{dc,cr}(t) = \frac{-(\mathbf{C}X)^2}{4\mathbf{D}} \tag{3.30}$$

$P_{BESS}^{dc}(t)$ should be always greater than the $P_{BESS}^{dc,cr}(t)$.

Since the function $V_{BESS}^{dc}(t) = f\left(P_{BESS}^{dc}(t)\right)$ has a monotonic behavior (see proposition I), the limits of the DC power can be easily computed.

Proposition I: The function of $V_{BESS}^{dc}(t) = f\left(P_{BESS}^{dc}(t)\right)$ shown by (3.28) is monotonic.

Proof:

A function is monotonic if and only if it is either entirely increasing or decreasing in the considered interval. Therefore, for any two values of $P_{BESS}^{dc}(t)^{(1)}$ and $P_{BESS}^{dc}(t)^{(2)}$;   if $P_{BESS}^{dc}(t)^{(2)} \geq P_{BESS}^{dc}(t)^{(1)}$ then $V_{BESS}^{dc}(t)^{(2)} \geq V_{BESS}^{dc}(t)^{(1)}$ (or   if $P_{BESS}^{dc}(t)^{(2)} \leq P_{BESS}^{dc}(t)^{(1)}$ then $V_{BESS}^{dc}(t)^{(2)} \leq V_{BESS}^{dc}(t)^{(1)}$).

Using (3.29) and taking the derivative of $V_{BESS}^{dc}(t)$ with respect to $P_{BESS}^{dc}(t)$, we get:

$$\frac{dV_{BESS}^{dc}(t)}{dP_{BESS}^{dc}(t)} = \frac{\mathbf{D}}{\sqrt{(\mathbf{C}X)^2 + 4\mathbf{D}P_{BESS}^{dc}(t)}} \tag{3.31}$$

Since the argument of the root as well as $\mathbf{D}$ are positive, $\dfrac{dV_{BESS}^{dc}(t)}{dP_{BESS}^{dc}(t)} \geq 0$. Thus,

$$\frac{dV_{BESS}^{dc}(t)}{dP_{BESS}^{dc}(t)} = \frac{V_{BESS}^{dc}(t)^{(2)} - V_{BESS}^{dc}(t)^{(1)}}{P_{BESS}^{dc}(t)^{(2)} - P_{BESS}^{dc}(t)^{(1)}} \geq 0 \tag{3.32}$$

From (3.32), it is clear that if $P_{BESS}^{dc}(t)^{(2)} \geq P_{BESS}^{dc}(t)^{(1)}$, then $V_{BESS}^{dc}(t)^{(2)} \geq V_{BESS}^{dc}(t)^{(1)}$ (conversely   if $P_{BESS}^{dc}(t)^{(2)} \leq P_{BESS}^{dc}(t)^{(1)}$,   then $V_{BESS}^{dc}(t)^{(2)} \leq V_{BESS}^{dc}(t)^{(1)}$).

∎

In order to find the limits of the BESS DC active power, we rely on the following constraints related to DC voltage, DC current and *SoE* limits:

$$
\begin{cases}
a) & V_{BESS}^{dc,min} \leq V_{BESS}^{dc}(t) \leq V_{BESS}^{dc,max} \\
b) & I_{BESS}^{dc,min} \leq I_{BESS}^{dc}(t) \leq I_{BESS}^{dc,max} \\
c) & SoE_{BESS}^{min} \leq SoE_{BESS}(t) \leq SoE_{BESS}^{max}
\end{cases}
\tag{3.33}
$$

a) DC voltage limits:

Rewriting (3.29), we can obtain $P_{BESS}^{dc}(t)$ as a function of $V_{BESS}^{dc}(t)$ shown by (3.34). This function is plotted in Figure 3-21. It is clear that the part related to the negative DC voltage is not feasible (blue-shaded area).

$$
P_{BESS}^{dc}(t) = f^{-1}\left(V_{BESS}^{dc}(t)\right) = \left(\frac{1}{\mathbf{D}}\right)V_{BESS}^{dc}(t)^2 - \frac{(\mathbf{CX})}{\mathbf{D}}V_{BESS}^{dc}(t)
\tag{3.34}
$$

It should be noted that during charging, $V_{BESS}^{dc}(t)$ increases. Thus, the maximum $P_{BESS}^{dc}(t)$ is obtained during charging phase considering the maximum limit of the DC voltage ($P_{BESS}^{dc\,maxV}\left(t\Big|_{V_{BESS}^{dc}(t)=V_{BESS}^{dc,max}}\right)$). On the contrary, during the discharge, $V_{BESS}^{dc}(t)$ decreases and the minimum $P_{BESS}^{dc}(t)$ is reached only during discharging phase considering the minimum limit of the DC voltage ($P_{BESS}^{dc\,min}\left(t\Big|_{V_{BESS}^{dc}(t)=V_{BESS}^{dc,min}}\right)$). Moreover, it should be noted that the pink-shaded area in the discharging phase is inconsistent with continuity.

The DC power constraints accounting for the DC voltage limits ($P_{BESS}^{dc,maxV}(t)$, $P_{BESS}^{dc,minV}(t)$) are computed by (3.35).

$$
\begin{cases}
P_{BESS}^{dc,maxV}(t) = f^{-1}\left(V_{BESS}^{dc,max}\right) \\
P_{BESS}^{dc,minV}(t) = f^{-1}\left(max\left(V_{BESS}^{dc,min}, \frac{\mathbf{CX}}{2}\right)\right)
\end{cases}
\tag{3.35}
$$
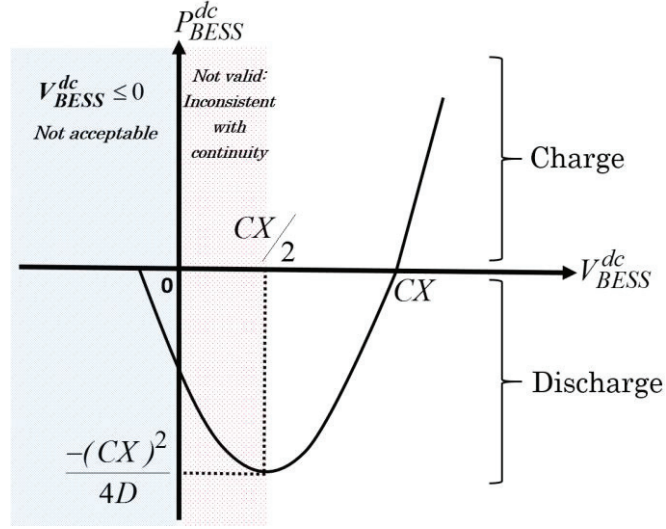
Figure 3-21 DC power of BESS as a function of DC voltage

b) DC current limits:

Eq. (3.36) is derived from (3.26) and (3.29).

$$P_{BESS}^{dc}\left(t\right)=g\left(I_{BESS}^{dc}\left(t\right)\right)=\mathbf{D}I_{BESS}^{dc}\left(t\right)^{2}+\left(\mathbf{C}X\right)I_{BESS}^{dc}\left(t\right)\tag{3.36}$$

The function (g) is plotted in Figure 3-22. In charging phase, by increasing $I_{BESS}^{dc}\left(t\right)$, $P_{BESS}^{dc}\left(t\right)$ increases. Thus, the maximum of $P_{BESS}^{dc}\left(t\right)$ is related to the maximum of dc current ($P_{BESS}^{dc,max\,I}\left(t\big|_{I_{BESS}^{dc}(t)=I_{BESS}^{dc,max}}\right)$). During discharging phases with negative current flow, the minimum of $P_{BESS}^{dc}\left(t\right)$ is corresponding to the one related to the $I_{BESS}^{dc,min}$ ($P_{BESS}^{dc,min\,I}\left(t\big|_{I_{BESS}^{dc}(t)=I_{BESS}^{dc,min}}\right)$). It should be noted that, due to the monotonic behavior of the $V_{BESS}^{dc}\left(t\right)$ and the BESS model presented by (3.23), there is only one solution of $I_{BESS}^{dc}\left(t\right)$ related to the $P_{BESS}^{dc}\left(t\right)$.

$$\begin{cases}P_{BESS}^{dc,max\,I}\left(t\right)=g\left(I_{BESS}^{dc,max}\right)\\ P_{BESS}^{dc,min\,I}\left(t\right)=g\left(I_{BESS}^{dc,min}\right)\end{cases}\tag{3.37}$$
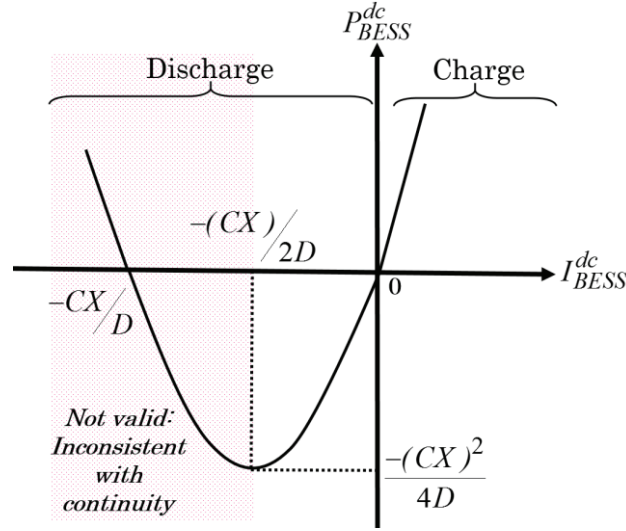
Figure 3-22 DC power of BESS as a function of DC current

c) SoE limits:

Using (3.22) and knowing the *SoE* at the current time, the DC power as a function of *SoE* is computed and plotted in Figure 3-23. The green-shaded area is the feasible area considering the *SoE* limits. Thus, for the current *SoE*, the maximum/minimum $P_{BESS}^{dc}(t)$ are calculated by (3.38). E_{nom} is the rated energy.

$$\begin{cases} P_{BESS}^{dc,max\,SoE}(t) = \dfrac{-E_{nom}}{\Delta t}\left(SoE(t) - SoE_{BESS}^{max}\right) \\ P_{BESS}^{dc,minSoE}(t) = \dfrac{-E_{nom}}{\Delta t}\left(SoE(t) - SoE_{BESS}^{min}\right) \end{cases} \tag{3.38}$$

∎

As a results a set of dynamic constraints are defined by (3.39).

$$\begin{cases} P_{BESS}^{dc,max}(t) = min\left(P_{BESS}^{dc,max\,I}(t), P_{BESS}^{dc,max\,V}(t), P_{BESS}^{dc,max\,SoE}(t)\right) \\ P_{BESS}^{dc,min}(t) = max\left(P_{BESS}^{dc,max\,I}(t), P_{BESS}^{dc,max\,V}(t), P_{BESS}^{dc,min\,SoE}(t)\right) \end{cases} \tag{3.39}$$

In order to compute the AC active/reactive power limits of the BESS, the converter model needs to be taken into account. A bidirectional DC/AC converter is used to interface the storage with the grid. The power converter is assumed to operate in four quadrants. In order to model the power converter, the constraints on AC active and reactive power are taken into account. It is assumed that the DC/AC converter is characterized by an efficiency, Ψ independent of its power flow. Thus, the converter is modeled using (3.40) and (3.41).

$$P_{BESS}^{dc}(t) = P_{BESS}^{ac}(t) + P_{conv}^{loss}(t) \qquad (3.40)$$

$$P_{conv}^{loss}(t) = (1 - \Psi)\sqrt{P_{BESS}^{ac}(t)^2 + Q_{BESS}^{ac}(t)^2} \qquad (3.41)$$

Considering the maximum/minimum DC active power of the BESS and using (3.40) and (3.41), the maximum/minimum AC active/reactive powers of BESS cell ($P_{BESS}^{ac,max}(t), P_{BESS}^{ac,min}(t), Q_{BESS}^{ac,max}(t), Q_{BESS}^{ac,min}(t)$) on the AC side of the power converter are computed. It should be stressed that the TTC model includes also the CR model. If we consider the CR model only for BESSs, this constraint is neglected.
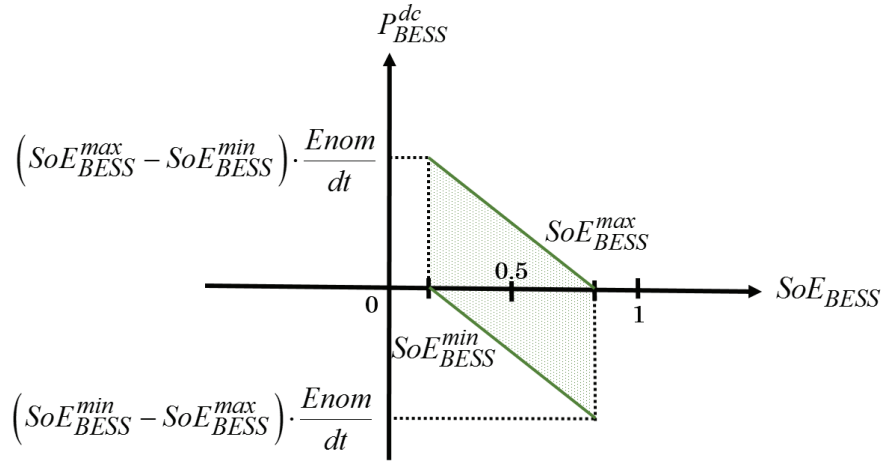
Figure 3-23 DC power of the BESS as a function of SoE

3.3.3 Distributed Grid Control Scheme

3.3.3.1 General Principles

Following the procedure presented in part I, the ADN is decomposed into k areas, each under the control of only one BESS. The mutual influences between the areas are neglected in order to avoid sharing the area internal states with the others. Thus, the control problem might be solved in a distributed manner. It is obvious that the number of CBBs involved in a given area is equal to the number of its neighbors. The zonal control is implemented using MAS concept [156]-[157]. In this work, Lithium-based BESSs is the considered as ESS technology. Since the only controllable unit in the areas is the ESS, an agent is assigned to each area dedicated to the related BESS which is called "BESS Agent" (*BA*). *BAs* have a full vision on their own areas states including the state of their related BESSs units, and area loads/generations.

3.3.3.2 Area Adaptive Model-Based Control Algorithm (MBC)

An adaptive real-time clustered MBC relying on an accurate dynamic representation of BESSs is proposed for multi-area ADNs. The proposed real-time control scheme is fully decentralized and performed independently by each *BA* in case of any bus voltage fluctuations over the limits or line ampacity violation in the corresponding areas. At each time-step, each *BA* performs two tasks:

1) Compute PL&C profile

The *BA* computes the maximum AC active/reactive powers that it can import/export from/to its direct neighbors at CBBs by its related BESS, along with the cost for the exchanged power. These values are sent to the corresponding neighbors at each time step as Power Limits and Cost ("PL&C") profile. In the same way, it receives the PL&C profile of the direct neighbors at each time step. In a given area, in order to compute the maximum active/reactive powers that it can import/export from/to each of its direct neighbors at its CBBs ($P_{CBB}^{ac,min}(t), P_{CBB}^{ac,max}(t), Q_{CBB}^{ac,min}(t), Q_{CBB}^{ac,max}(t)$), the operational limits of the related BESS in terms of DC active power are taken into account ($P_{BESS}^{dc,min}(t), P_{BESS}^{dc,max}(t)$). In this respect, power sensitivity coefficients (Λ^P and Λ^Q) are used. Λ^P and Λ^Q are calculated using the so-called *VSC* [133] at each time-step. For the sake of simplicity, the index of time is removed in the coefficients. The *VSC*s can be computed for both active/reactive powers of BESS located in ADNs (VSC^P, VSC^Q). For each CBB, Λ^P and Λ^Q specifically link CBB powers to BESS P/Q power variation using (3.42)-(3.43).

$$\Lambda_{BESS \to CBB}^{P} = \frac{\partial P_{CBB}}{\partial P_{BESS}} = \frac{\dfrac{\partial V_{CBB}}{\partial P_{BESS}}}{\dfrac{\partial V_{CBB}}{\partial P_{CBB}}} = \frac{VSC_{BESS \to CBB}^{P}}{VSC_{CBB \to CBB}^{P}} \tag{3.42}$$

$$\Lambda_{BESS \to CBB}^{Q} = \frac{\partial Q_{CBB}}{\partial Q_{BESS}} = \frac{\dfrac{\partial V_{CBB}}{\partial Q_{BESS}}}{\dfrac{\partial V_{CBB}}{\partial Q_{CBB}}} = \frac{VSC_{BESS \to CBB}^{Q}}{VSC_{CBB \to CBB}^{Q}} \tag{3.43}$$

Knowing $\Lambda_{BESS \to CBB}^{P}$, $\Lambda_{BESS \to CBB}^{Q}$ and AC power limits at BESSs buses, the boundary limits of imported/exported P/Q at each CBB are obtained using (3.44)-(3.47).

$$P_{CBB}^{ac,min}(t) = P_{BESS}^{ac,min}(t) \times \Lambda_{BESS \to CBB}^{P} \tag{3.44}$$

$$P_{CBB}^{ac,max}(t) = P_{BESS}^{ac,max}(t) \times \Lambda_{BESS \to CBB}^{P} \tag{3.45}$$

$$Q_{CBB}^{ac,min}(t) = Q_{BESS}^{ac,min}(t) \times \Lambda_{BESS \to CBB}^{Q} \qquad (3.46)$$

$$Q_{CBB}^{ac,max}(t) = Q_{BESS}^{ac,max}(t) \times \Lambda_{BESS \to CBB}^{Q} \qquad (3.47)$$

At each time-step, each *BA* sends its AC active/reactive power limits at CBBs to the corresponding neighbors. Also, it sends the cost of the active power it can provide to the neighbors at CBBs. It is assumed that there is no cost for the exchanged reactive power between areas and the cost is only related to the exchanged active power. The cost of the $P_{CBB}^{ac}(t)$ is calculated, for instance, by (3.48).

$$h(t) = \lambda \cdot P_{CBB}^{ac}(t)^{2} \qquad (3.48)$$

As a result, the five-tuple $\left\{ P_{CBB}^{ac,max}(t), P_{CBB}^{ac,min}(t), Q_{CBB}^{ac,max}(t), Q_{CBB}^{ac,min}(t), h(t) \right\}$ is updated by each *BA* at each CBBs as PL&C profile information.

2) Local Optimization Problem

Each *BA* monitors the area internal states (i.e. node voltages, line currents) with a refresh rate that, for instance, can be of hundreds of ms. In case of any violation on node voltages or line ampacity, it solves the MBC optimization problem locally accounting for the PL&C profiles received from neighbors. Finally, it determines a feasible BESS operating points (i.e. active/reactive power set-points) for its corresponding BESS as well as the required active/reactive powers needed from neighbors. In this study the power flow is assumed to be positive for power import and negative for power export. The area optimization problem is formulated as (3.49).

$$\min_{\substack{P_{BESS}^{ac}(t), Q_{BESS}^{ac}(t) \\ P_{CBB_{w}}^{ac}(t), Q_{CBB_{w}}^{ac}(t)}} \beta_{1}\Gamma(t) + \beta_{2}\Upsilon(t) + \beta_{3}H(t) + \beta_{4}\Psi(t) \qquad (3.49)$$

$$s.t \begin{array}{ll} a) & SoE^{min} \le SoE(t) \le SoE^{max} \\ b) & P_{BESS}^{ac}(t)^{2} + Q_{BESS}^{ac}(t)^{2} \le S_{conv}^{2} \\ c) & P_{BESS}^{dc,min}(t) \le P_{BESS}^{dc}(t) \le P_{BESS}^{dc,max}(t) \\ d) & P_{CBB_{w}}^{ac,min}(t) \le P_{CBB_{w}}^{ac}(t) \le P_{CBB_{w}}^{ac,max}(t) \\ e) & Q_{CBB_{w}}^{ac,min}(t) \le Q_{CBB_{w}}^{ac}(t) \le Q_{CBB_{w}}^{ac,max}(t) \\ f) & \left| I_{sr}(t) \right| \le I_{sr}^{max} \end{array}$$

$\beta_{1}, \beta_{2}, \beta_{3}, \beta_{4}$ are weighting the terms of the objective function.

a) Objective function:

The objective function includes four parts:

a.1) BESSs operation costs $\left(\Gamma(t)\right)$

The operation cost of the battery is expressed with (3.50) as a penalty of the deviation
of the *SoE* from a reference value. Since the adopted control does not include any
prediction on the load absorptions and DG injections, this choice is justified to keep
the battery into an average *SoE* condition that allows to equally absorb and provide
energy with respect to the stochastic injections/absorptions.

$$\Gamma(t) = k\left(SoE(t) - SoE_{ref}\right)^4 \cdot \left(a \cdot SoE(t)^2 - b \cdot SoE(t) + c\right) \tag{3.50}$$

Where a,b,c are constant. The function $\Gamma(t)$ is shown in Figure 3-24. It is seen that
the cost increased significantly when the battery *SoE* is close to the fully
charged/discharged condition.

a.2) Area node voltage regulation $\left(\Upsilon(t)\right)$

In order to keep the area nodes voltages, close to the desired value, the norm of the
voltage deviations is minimized for all nodes of the area at each time-step.

$$\Upsilon(t) = \sum_{i \in N_{area},t} \left\| \left|\overline{V}_i(t)\right| - V_{ref} \right\|^2 \tag{3.51}$$

Since the link of this objective function with the control variable is non-convex
(power flow equations), we have adopted a linear programming approach relying on
VSC. As a result, the voltage at bus *i* could be expressed as its initial measured value
($\overline{V}_i^{init}(t)$) plus a variation ($\Delta\left|\overline{V}_i(t)\right|$) provided by the BESSs pertaining to the current
area and its neighbors.

$$\left|\overline{V}_i(t)\right| = \left|\overline{V}_i^{init}(t)\right| + \Delta\left|\overline{V}_i(t)\right| \tag{3.52}$$

$\Delta\left|\overline{V}_{i,t}\right|$ is computed by the following linear equation:

$$\Delta\left|\overline{V}_i(t)\right| = \left(P_{BESS}^{ac}(t) \cdot VSC_{BESS \to i}^P + Q_{BESS}^{ac}(t) \cdot VSC_{BESS \to i}^Q\right) + \sum_{w=1}^{CBBN} \left(P_{CBB_w}^{ac}(t) \cdot VSC_{CBB_w \to i}^P + Q_{CBB_w}^{ac}(t) \cdot VSC_{CBB_w \to i}^Q\right) \tag{3.53}$$
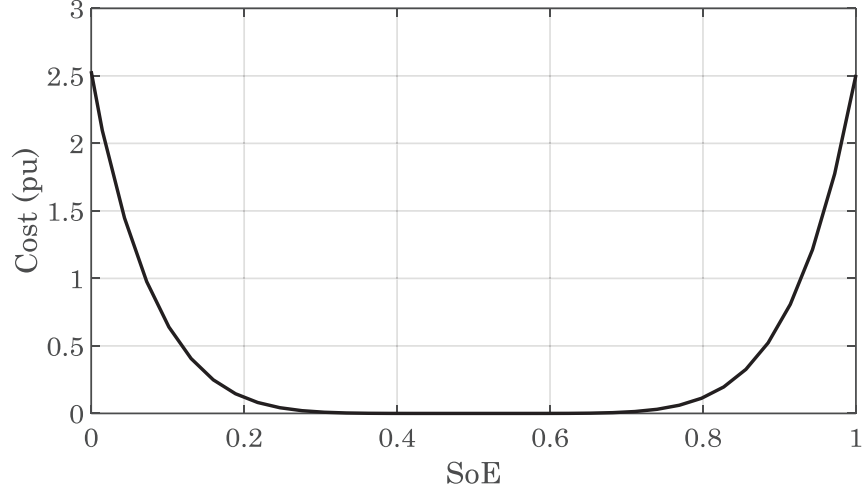
Figure 3-24 BESS cost function expressed by (3.50)

a.3) Imported/Exported (IE) energy costs $\left(\mathrm{H}(t) \right)$

The cost of the required active power from neighbors should be minimized in order to solve the problem locally. This objective function is computed by (3.54).

$$\mathrm{H}(t) = \sum_{w=1}^{CBBN} \lambda_w \cdot P_{CBB_w}^{ac}(t)^2 \tag{3.54}$$

a.4) Area line current flow regulation $\left(\Psi(t) \right)$

In order to keep the area line currents below the line ampacity, the norm of the area line current is minimized for all lines of the area at each time-step. It should be noted that the area line current is normalized at its ampacity.

$$\Psi(t) = \sum_{s,r \in N_{area},t} \left\| \left| \overline{I_{sr}}(t) \right| \right\|^2 \tag{3.55}$$

As for the voltage regulation, the sensitivities allow to obtain the linear relations between the line currents and the active/reactive power injections of BESSs pertaining to the current area and its neighbors. Current sensitivities $\left(\Pi^P, \Pi^Q \right)$ with respect both P/Q are computed online solving a linear system of equations as

presented in [133]. Thus, the line current between any two area nodes (s and r) could be expressed as its initial value ($\overline{I}_{sr}^{init}(t)$) plus a variation ($\Delta\left|\overline{I}_{sr}(t)\right|$).

$$\left|\overline{I}_{sr}(t)\right| = \left|\overline{I}_{sr}^{init}(t)\right| + \Delta\left|\overline{I}_{sr}(t)\right| \tag{3.56}$$

$\Delta\left|\overline{I}_{sr}(t)\right|$ is computed with the following (approximated) linear equation:

$$\Delta\left|\overline{I}_{sr}(t)\right| = \left(P_{BESS}^{ac}(t)\cdot\Pi_{BESS\to sr}^{P} + Q_{BESS}^{ac}(t)\cdot\Pi_{BESS\to sr}^{Q}\right) + \\ \sum_{w=1}^{CBBN}\left(P_{CBB_w}^{ac}(t)\cdot\Pi_{CBB_w\to sr}^{P} + Q_{CBB_w}^{ac}(t)\cdot\Pi_{CBB_w\to sr}^{Q}\right) \tag{3.57}$$

b) Constraints

In the control optimization problem formulated as (3.49), the constraints are related to the *SoE* limits, PQ capability curve of the power converter, BESS DC active power limits, CBBs active/reactive imported/exported power constraints and line current ampacity limits respectively demonstrated by (3.49)-(a-f).

c) Optimality

It should be pointed out that the proposed local area control problem is a convex optimization problem which always leads to a global optimal solution. In fact, the linear programming technique using voltage sensitivity coefficients are used for this purpose.

d) Implementation and Communication

All the interactions between agents take place via a form of message passing. The exchanged message functions or actions used in this part are the same as those used in Part II:

- INFORM: the sender informs the receivers that some actions are performed. It also sends its new updates;

- REQUEST: the sender requests from the receivers to perform some actions;

- ACCEPT: the action of accepting a request;

- REFUSE: the action of refusing a request;

- CONFIRM: the sender informs the receivers that a given proposition is true, where the receiver is known to be uncertain about the proposition.

The structure of message exchange is peer-to-peer (p2p) as any agent is able to initiate communication with its adjacent one or to be the subject of an incoming communication at any time from those adjacent agents. The general framework of the communication is shown in Figure 3-25. At each time step, *BA* sends the INFORM message to its direct adjacent *BAs* with the updated "PL&C" information. *BA* monitors the state of its area (i.e. node voltages, line currents) from sensors located in the system. Only in case an area node voltage is outside the limits or a line current violates the ampacity limit, the *BA* solves the local optimization problem formulated by (3.49) thanks to the updated PL&C information received from the neighbors. Consequently, active and reactive powers of related BESS and CBBs are computed. The required P/Q powers from corresponding neighbors are sent as a REQUEST message to the related *BAs*. The received REQUEST message by each neighbor is inserted into a request queue. Different strategy can be used to process the received requests. In this study the "First in- First serves" strategy is used for this purpose. Each *BA* who has received the REQUEST message, should make the decision in order to ACCEPT or REFUSE the request based on the feasibility of its expected internal state. Actually, the expected internal state (node voltage and current flow profiles) is assessed using voltage/current sensitivity coefficients. If a *BA* cannot meet the request demand powers, it sends the REFUSE message. In this case, the *BA* with voltage/current violations should solve the control optimization again considering the new updated PL&C profiles. After receiving the ACCEPT messages from all the neighbors, the *BA* of concern sends CONFIRM message to them in order to let them to change their P/Q set-points of their related BESSs providing therefore the requested powers at corresponding CBBs; obviously in the same time the P/Q set-points of the internal BESS are updated as well.
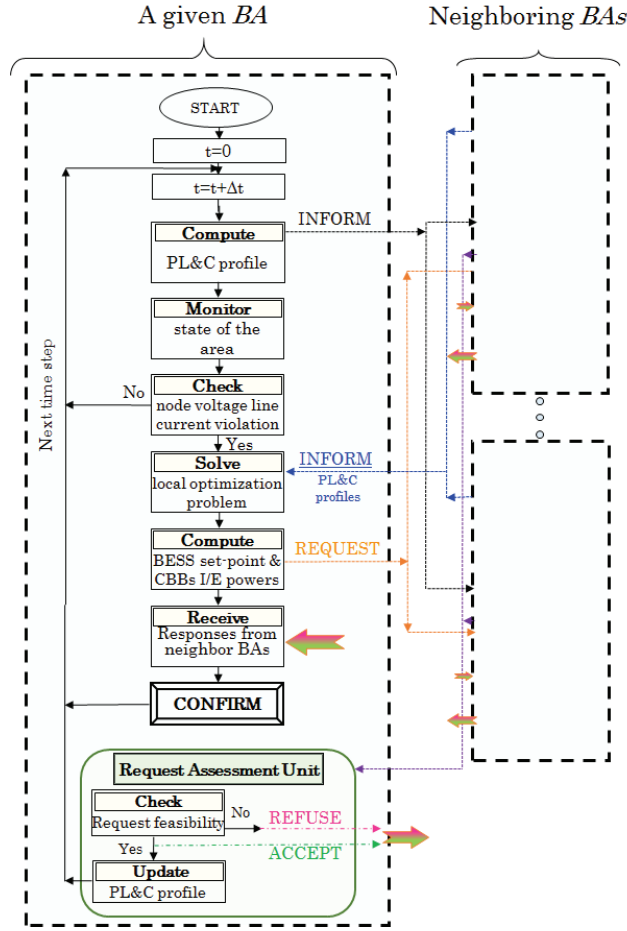
Figure 3-25 Communication structure among BAs

3.3.4 Performance Evaluation

The performance evaluation of the proposed control method is carried out making reference to the 13 nodes IEEE test grid [158]. The network loads and PV injections are inferred from a real feeder of the 20 kV ADN on EPFL campus [168]. Non-dispatchable DG units (PVs) are connected to the system at buses 4, 8 and 10. Their power injections are represented by voltage-independent active power injections with null reactive component. The schematic of the system is shown in Figure 3-26. The aggregation of loads apparent power absorptions and PVs active power injections for a given day is shown in Figure 3-27.

The proposed control methods are applied in the system considering three BESSs located at buses 4, 6 and 12. Consequently, 3 areas are obtained. Bus 2 and 7 are selected as CBBs between areas A_1 and A_2, A_3 respectively. In all the simulations, the optimization problem is solved using the Matlab® and YALMIP optimizer [159].

The simulations are run on a workstation equipped with a 2.7 GHz quad core INTEL i7 processor, 8 GB of RAM.
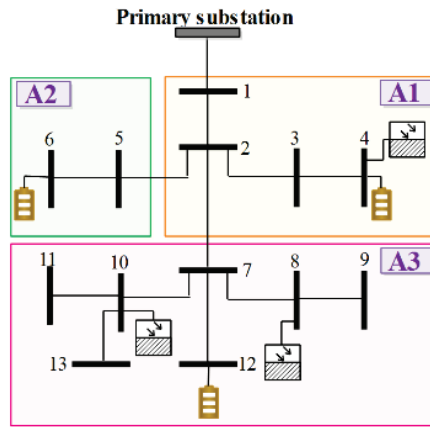
Figure 3-26 IEEE 13 node test system
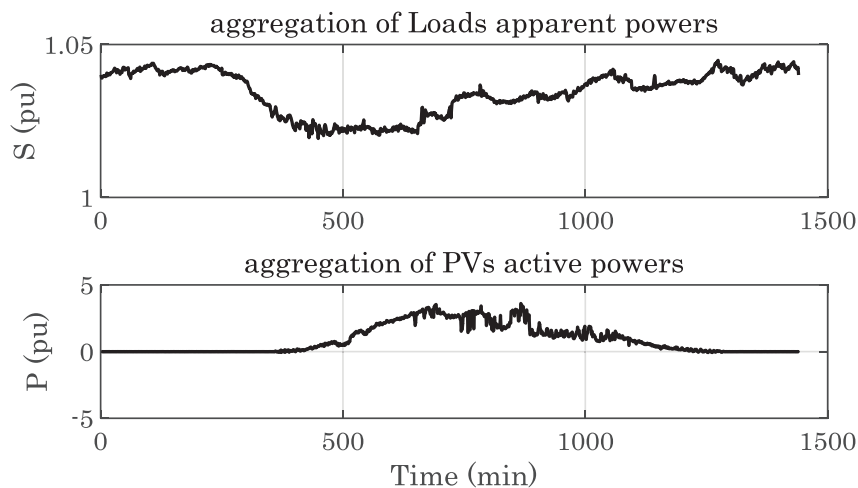
Figure 3-27 Aggregation of loads/PVs absorptions/injections (base power: 5MW)

In order to show the effectiveness of the proposed method, the centralized equivalent algorithm is chosen as benchmark. The control problem formulation for centralized method is presented in Appendix B. To this end, a comparison is made in case of I) no control in the network, II) centralized equivalent method III) proposed decentralized control method.

Error! Reference source not found. shows the maximum, minimum, average values of all the area node voltages for the three areas. As expected, the proposed decentralized method leads to slightly worst voltage profiles in comparison with the centralized one since it does not account for VSC associated to BESSS located in

areas other than the targeted one. However, they always allow limiting the voltage deviations and avoiding the need of sharing all the network data.

Error! Reference source not found. shows the absolute values of the current flow in lines 1-2 and 2-3 and the corresponding line ampacities in the three cases. It is clear that in the case of no control there are line current violations. This problem is solved using the proposed control methods. It should be noted that line current ampacity constraint is a hard constraint. As it is seen in **Error! Reference source not found.** , due to the large PV production, there are periods during the day when both the voltage and currents exceed the allowed limits. This is mostly seen in area A1. Due to the hard line current constraint, the proposed algorithm keeps the current below the limits. However, the control action is not sufficient to manage efficiently the voltage control that, on the contrary, is on the objective of the control function. The maximum variation of voltage in area A1 has yet improved with respect to the case with no control action.

SoE of the three BESSs are shown in Figure 3-30. It is seen that due to the large penetration of PVs (particularly at node 4), the BESSs are charged.

The two-presented models for BESS in part II are compared in order to see the influence of the accurate BESS model on the grid voltage control. Centralized control is only used for this purpose. Figure 3-31 shows the *SoE* of the three BESSs for both presented models. It is worth observing that, the set-point computed by the optimal controller are different for the two models. From Figure 3-31, it can be seen that a lower energy net flow is requested when BESSs are modeled using the TTC model. The DC powers of BESSs for both models are shown in Figure 3-32, Figure 3-33 and Figure 3-34. It can be seen that the action of the computed DC power limits in the TTC model is evident. As it is seen, using the CR model, the DC powers asked from the BESSs can violate operational DC limits of the BESS.

Figure 3-35 shows, the maximum, minimum and average values of all the network node voltages for the two cases (centralized control) as well as the case with no BESSs control. As it can be seen, the centralized control coupled with the TTC model leads to slightly worst voltage profiles due to the limiting action of the BESS DC constraints. However, the solution provided by this controller always satisfy the operational limits of the BESSs and, therefore, provide feasible solutions with respect to the constraints of these devices.
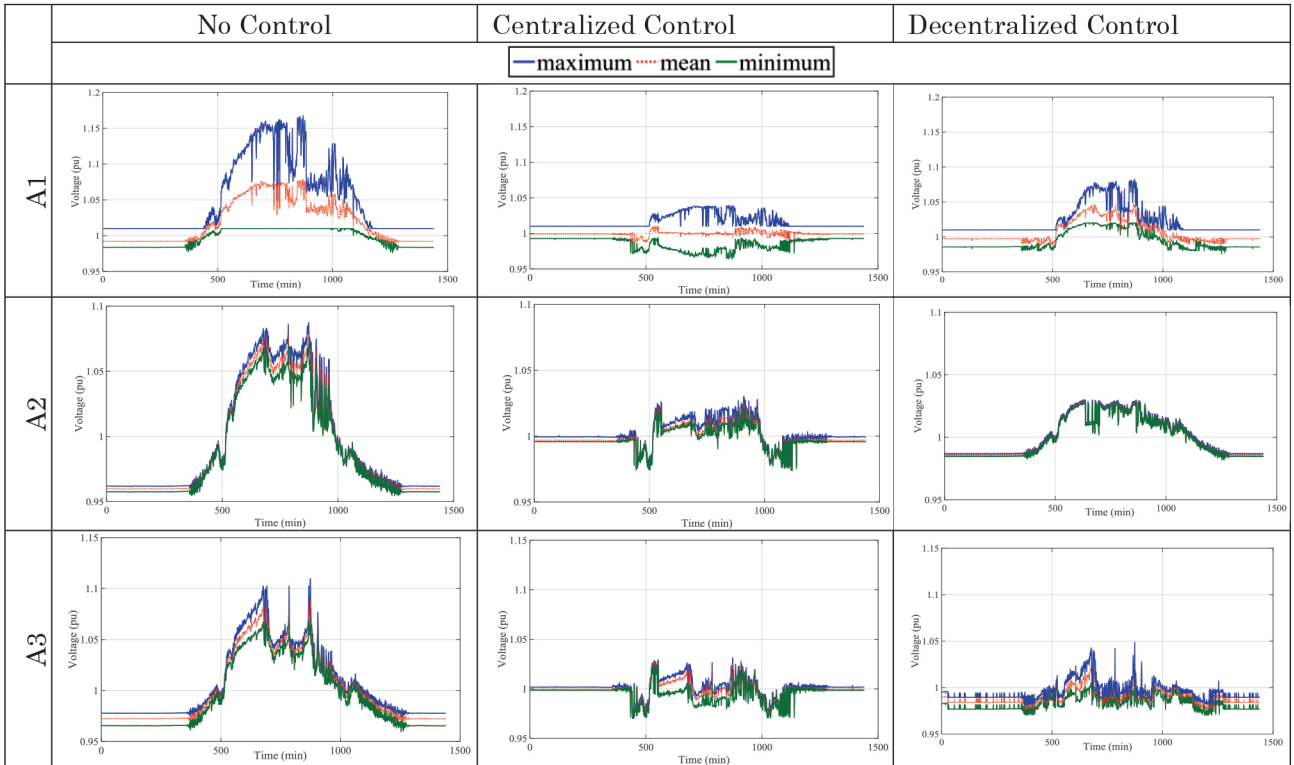
Figure 3-28 Minimum, maximum, mean values of the three area nodes voltages for three case I) no control II) decentralized control
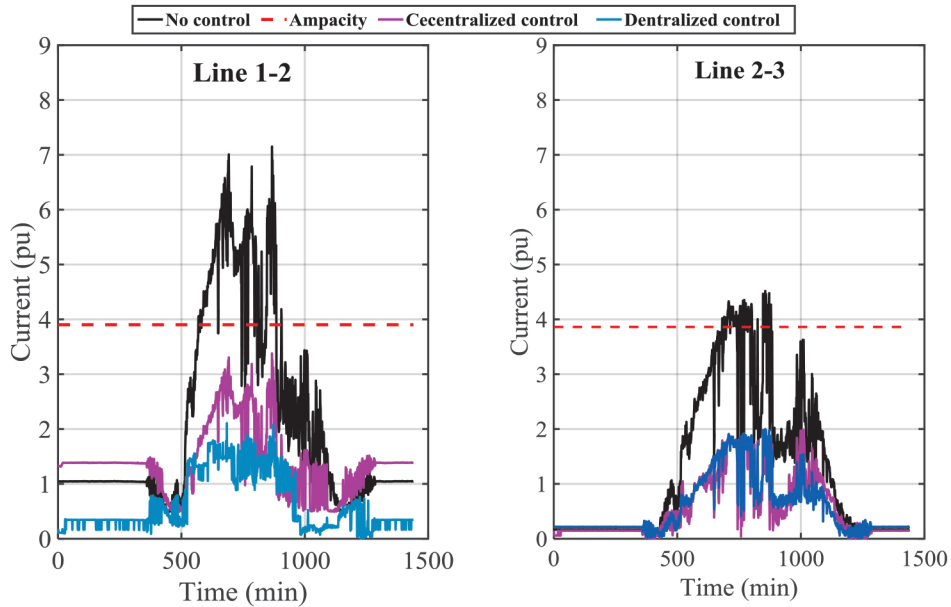
Figure 3-29 Line flows and ampacities in lines 1-2 and 2-3 for three case I) no control II) decentralized control
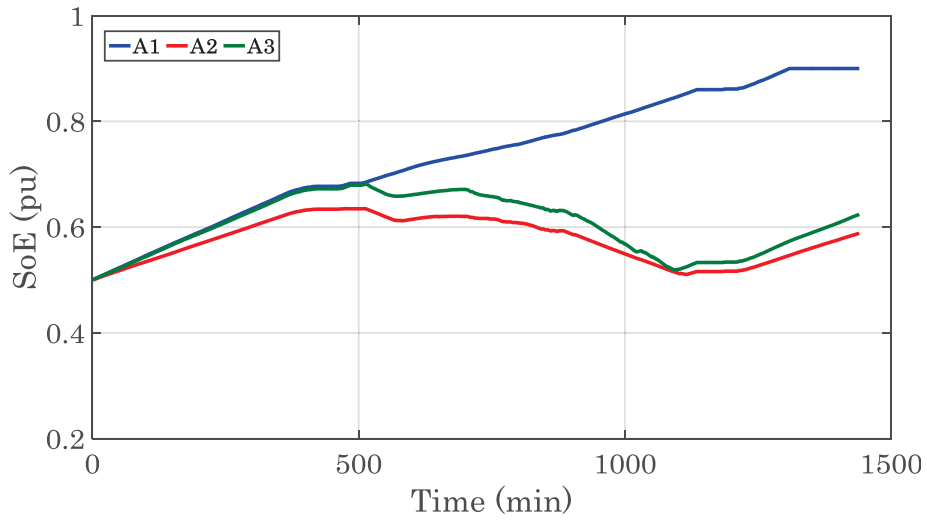
Figure 3-30 SoE of the BESSs in three areas
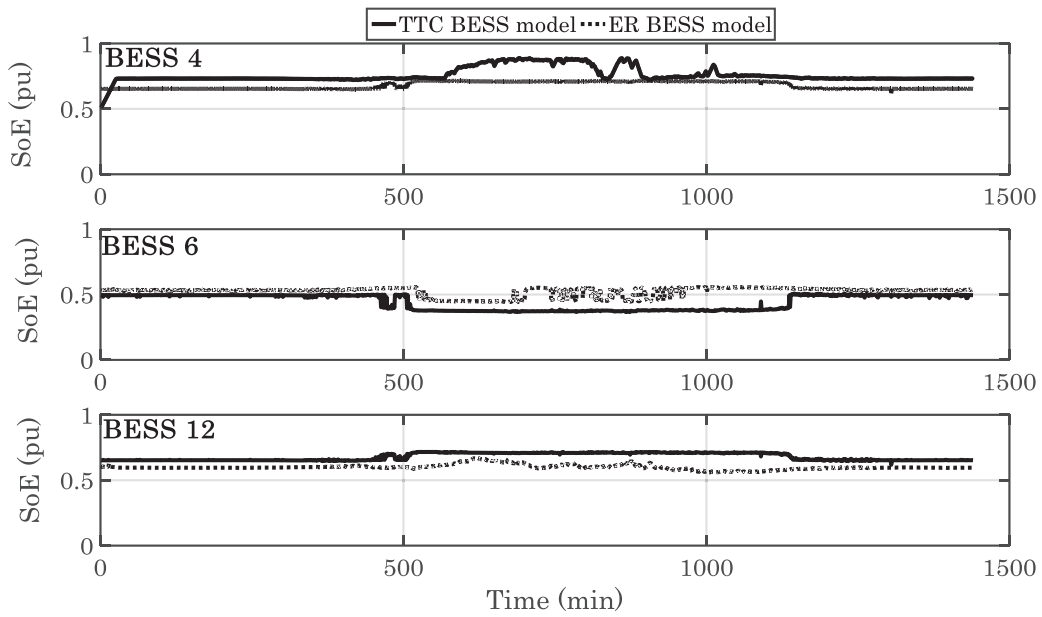
Figure 3-31 SoE for the two CR and TTC model of BESS
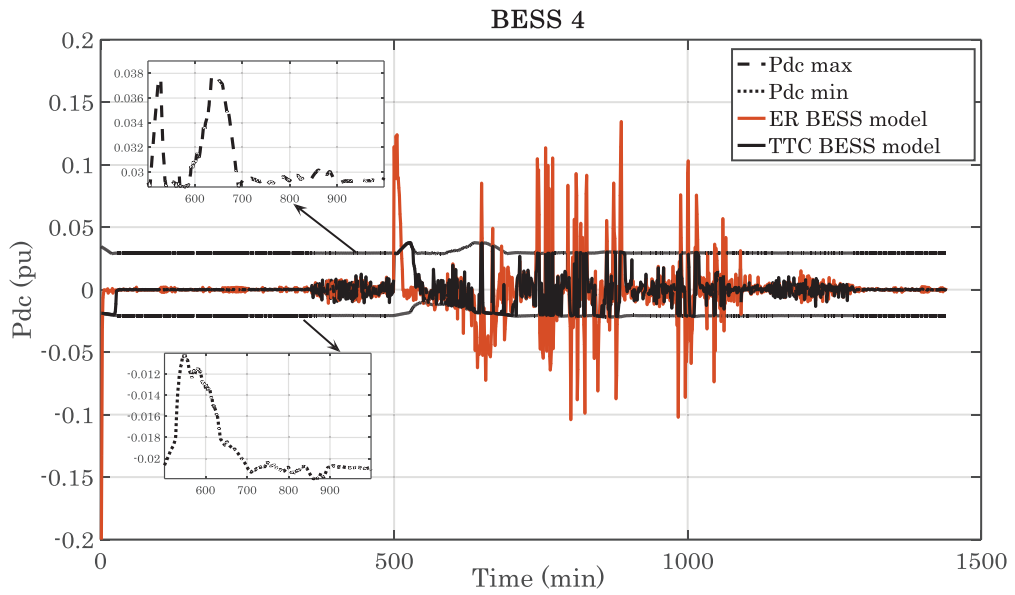
Figure 3-32 DC power of BESS 4 for the CR and TTC models
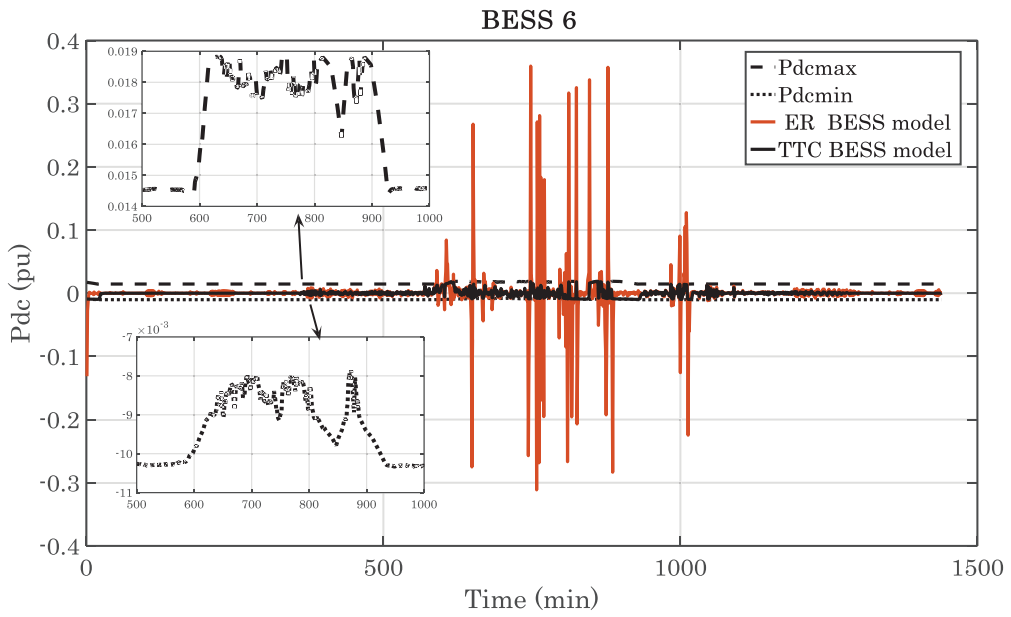
Figure 3-33 DC power of BESS 6 for the CR and TTC models
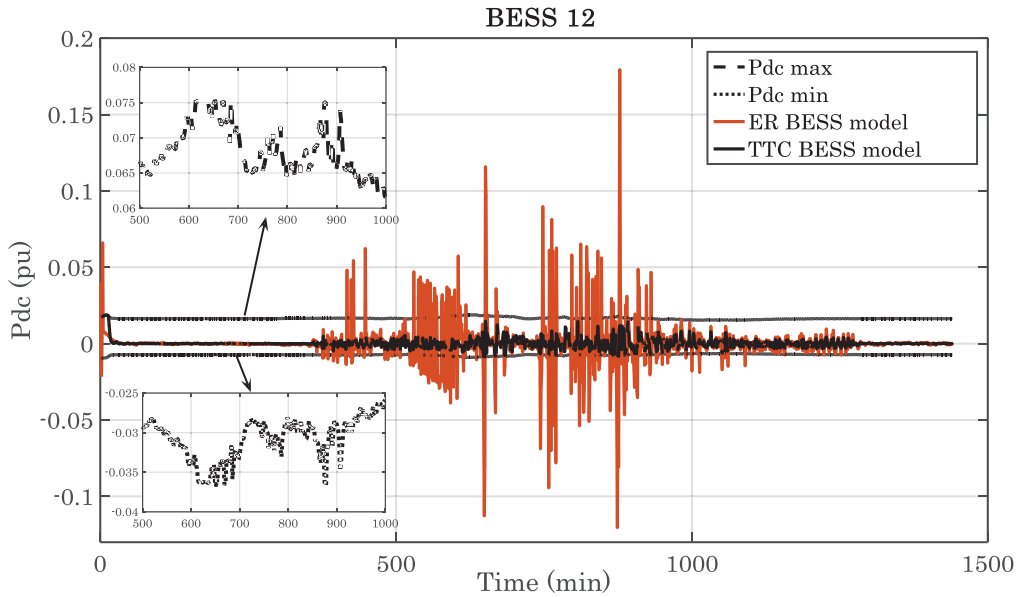
Figure 3-34 DC power of BESS 12 for the CR and TTC models
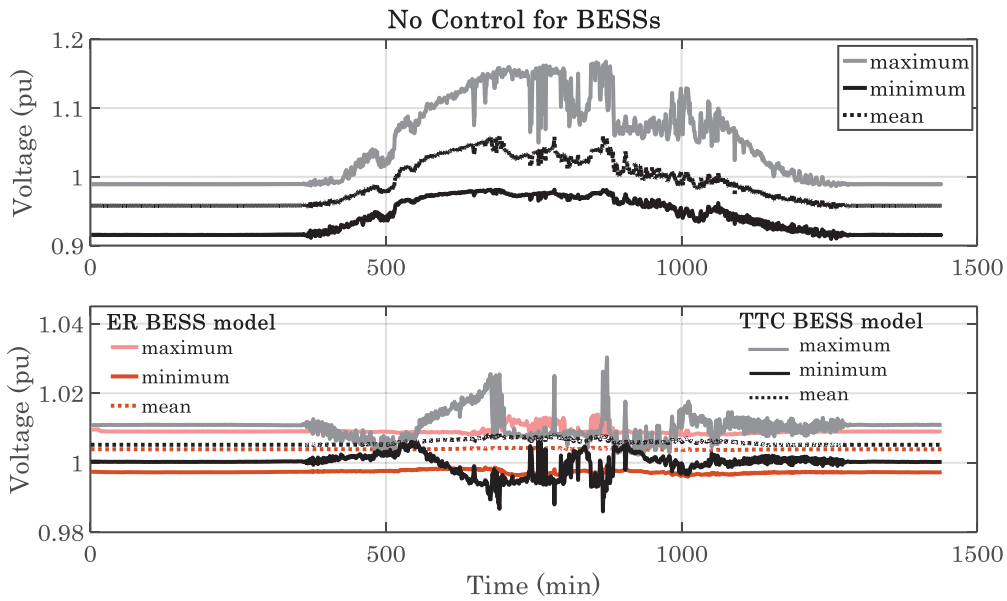
Figure 3-35 Distribution of all node voltages for the three cases: 1) no control for BESS, 2) CR model of BESS, 3) TTC model of BESS

Conclusion

This chapter has first discussed the partitioning of Active Distribution Network (ADN) in order to define distributed voltage control processes actuated by means of a limited number of distributed Energy Storage Systems (ESSs). In this respect, part I has illustrated the process to define the areas for which each ESS maximizes its

influence. This clustering relies on linear programming using the concept of voltage sensitivities. Performing a probabilistic load flow allows to infer the Voltage Influence Factor (VIF) of ESS injected/absorbed powers on the grid nodal voltages.

Based on this clustering, two decentralized scheduling strategies have been illustrated in part II. The first one relies on the concept of Thévenin equivalents of adjacent areas whilst the second one relies on the iterative adjustment of the power equilibrium of the areas. In both proposed methods, the mutual influences between the areas are sacrificed in order to avoid sharing the area internal states with the others. The Thévenin-based scheduling approach is an asynchronous algorithm in which each ESS can control its own area using the last information made available by the adjacent ones in order to infer the relevant network equivalents. Thus, the main feature of the proposed method is the independence of the voltage control for each area and the possibility for any area to join into or move back from the scheduling scheme. On the contrary, in the Top-down sweep scheduling approach the scheduling of each area depends on its neighbors.

Both algorithms are implemented in a MAS environment with different architectures of the message exchange. It has shown that both methods provide almost the same voltage improvements compared to the equivalent centralized problem. Due to the approximation considered for computing network equivalent model, the Thévenin-based scheduling method results in slightly worse voltage profiles than the Top-down sweep method. In addition, the number of exchanged messages among the areas in the Top-down sweep method is less than the ones in the Thévenin-based method resulting in less computation burden. With respect to a centralized algorithm, the aim of the network clustering is to reduce the computational burden among the clusters when one of the two proposed decentralized algorithms is adopted.

Part III has proposed a decentralized adaptive model-based real-time grid control (voltage control and congestion management) using Battery Energy Storage Systems (BESSs). The proposed method relies on an accurate dynamic model of the BESSs for the clustered Active Distribution Networks in presence of stochastic energy resources. An area control agent (BA) is assigned to the related BESS in the area which performs the proposed control optimization algorithm and makes decisions independently using the last updated information (PL&C) made available by the adjacent ones. Two different BESSs models presented in chapter 2, namely Charge Representative (CR) model and Two Time Constant (TTC) model, are used. These two models have been considered in a decentralized control algorithm and congestion management. The analytical computation of the battery DC power constraints using the TTC model is considered in the area optimization problem solved by each BA.

The communication among areas is implemented using Multi-Agent Systems in terms of message exchange pattern.

The performance of the proposed method is compared with those obtained for the case where BESSs are modeled as ideal energy reservoirs (CR model). Such an assessment is carried out using a numerical example referring to IEEE 13 buses distribution test feeder suitably adapted to include stochastic generation and BESSs. It is shown that, for the considered operation scenarios, the proposed grid control method provides feasible voltage and current profiles. The control coupled with the TTC model leads to slightly worst voltage profiles due to the limiting action of the BESS DC constraints. However, the solution provided by this controller always satisfy the operational limits of the BESSs and, therefore, provide feasible solutions with respect to the constraints of these devices. On the contrary, the adoption of the CR model might provide unfeasible solution since the DC voltage/current limits of BESSs may not be respected.

4 Conclusion

As known, Distributed Generations (DGs) emerge as an alternative power resource to Active Distribution Networks (ADNs). However, since most of high penetration of DGs are not utility owned and characterized by high degree of uncertainty, the control and operation of ADNs are different from traditionally expected behavior. In general, the main problem associated to the considerable connection of DGs is represented by the quality-of-service of ADNs usually associated to node voltage quality and line congestion mitigation. This thesis offers a promising near-term solution using distributed Energy Storage Systems (ESSs) which can guarantee a more flexible network. In this respect, advanced control/scheduling methods are proposed for ADNs actuated by means of a limited number of distributed ESSs. For this purpose, advanced models of ESSs are considered. Thus, in addition to the proposition of a generic charge representative model for any electrochemical ESSs, an improvement of the most common electric equivalent circuit models for the two ESS devices, namely double-layer supercapacitors and electrochemical lithium-based batteries are proposed for the deployment of specific control schemes. In order to develop the control/scheduling algorithms, ADNs are clustered using a novel network partitioning strategy with the aim of optimal voltage control. Then two decentralized operational scheduling algorithms and a real-time adaptive model-based decentralized control algorithm for the clustered ADNs are proposed.

4.1 Summary and Conclusion

In what follows, a summary of the studies that have been accomplished to develop the proposed decentralized control/scheduling algorithms of ADNs integrating ESSs is presented.

Control-Oriented Model of Energy Storage Systems

Since the main hypothesis of this thesis is to control the ADNs only by means of ESSs, the accurate estimation of ESS behavior is utmost important. In this respect, this manuscript first focuses on the generic Charge Representative (CR) modeling of any electrochemical ESSs.

Among the several approaches estimating the State-of-charge (SoC) of ESSs, coulomb counting method is more appropriate for online estimations. However, this method does not entirely account for the nonlinear capacity behavior. In this regard, an accurate algorithm for SoC estimations is proposed. Then, two ESS technologies (that fit the applications into ADNs), characterized by opposite characteristics, are selected intentionally; namely double layer supercapacitors with high power/low energy densities and electrochemical batteries with low power/high energy densities. In this respect, an improvement of the most common electric equivalent circuit models for the two devices is provided for the development of specific control schemes. It is based on the modeling of redistribution of charges that characterizes the dynamic behaviors of the two devices during long time charging/discharging and relaxation phases. The redistribution of charge consists three effects, namely rate capacity effect, hysteresis effect, and recovery effect. The first two effects are considered in the proposed SoC estimation algorithm and the recovery effect is taken into account considering virtual current generators.

It should be noted that, the virtual current generators do not violate the charge balance of the ESSs since they are not injecting an external current; but they model the movement of the charges already stored in the electrolyte.

Making reference to experimental tests carried out on a 325F supercapacitor and a 30Ah Lithium-Titanate battery in DESL-EPFL Smart Grid Laboratory, this study first discusses the optimal parameters assessment of the relevant models and, then, the improvement of the model behavior by accounting for the charge redistribution phenomenon is demonstrated. In this respect, it can be concluded that the proposed enhanced models represent an adequate extension of the classical ones with a minimal computational overhead. Also, it is shown that the proposed models are robust against the temperature variations.

Advanced Decentralized Control of Active Distribution Networks with the Integration of Dispersed Energy Storage Systems

Theoretically, operation and control of ADNs can be achieved centrally through the dispatch of active and reactive power of ESSs. Such an active management scheme would involve the centralization of all the information and consequent decisions in a single processing unit (or Central Controller). Although the centralized strategy is the most straightforward way to achieve the management of the network, it has several drawbacks related to the computation complexity; the possibility of losing the only central supervisor; facing difficulties when global information is not available, and high investment requirement in communication and data processing. Due to the above-mentioned downsides, the decentralized schemes are considered subdividing the network into quasi-autonomous areas. To this end, given a set of ESSs optimally located in a balanced and radial ADN, this thesis proposes a network partitioning strategy for the optimal voltage control of ADNs. Thus, the network is decomposed into several areas; each under the control of one ESS which has maximum influence on its corresponding area. The proposed partitioning relies on linear programming using the concept of voltage sensitivities. Performing a probabilistic load flow allows to infer the voltage influence factor of ESS injected/absorbed powers on the grid nodal voltages. In order to define a decentralized scheme and decrease the communication costs and computation burden, it is assumed that the operating information within each zone is not shared with the others and each zone is independently controlled merely relying on the dedicated single ESS unit whose control variables are its active and reactive power set points; thus, it does not contain any directly-controllable generator, or load.

Based on this clustering, two decentralized scheduling strategies and a real-time decentralized control algorithm for the clustered ADNs are proposed. The proposed zonal control capability focuses on voltage control and line congestion management. In both proposed decentralized scheduling and real-time control algorithms the communication among different areas is defined using the concept of multi-Agent Systems (MAS). However, the architectures of the message exchange are different.

First, two decentralized operational scheduling algorithms are proposed relying, respectively, on Thévenin equivalents and a recursive Top-down sweep approaches.

The Thévenin-based scheduling approach is an asynchronous algorithm in which each ESS can control its own area using the last information made available by the adjacent ones in order to infer the relevant network equivalents. Thus, the main feature of the proposed method is the independence of the voltage control for each area and the possibility for any area to join into or move back from the scheduling scheme. In this method a coordination agent is considered taking care about the

coordination between all the area agents. It is important to notice that the coordination agent is not a central controller.

Top-down sweep scheduling approach is based on a recursive approach and the scheduling of each area depends on its neighbors. The architectural model of the message exchange of this second approach is peer to peer (p2p). Thus, unlike the Thévenin-based scheduling approach, there is no need for central coordinator agent.

It is shown that both methods provide almost the same voltage improvements with reference to the equivalent centralized problem. Due to the approximation considered for computing network equivalent model, the Thévenin-based scheduling method results in slightly worse voltage profiles than the Top-down sweep method. In addition, the number of exchanged messages among the areas in the Top-down sweep method is less than the ones in the Thévenin-based method resulting in less computation burden.

A decentralized adaptive model-based real-time grid control using only distributed BESSs is presented afterwards. The proposed method relies on an accurate dynamic model of BESSs capable to account for their DC active power limits. This method is fully decentralized and performed independently by each area agent in case of any bus voltage fluctuations over the limits or line ampacity violation in the corresponding areas. Thus, each area agent performs the proposed control optimization algorithm and makes decisions independently using the last updated information made available by the adjacent ones. The analytical computation of the battery DC power constraints using the BESS model is considered in the area optimization problem solved by each area agent. The two different BESSs models presented in previous part namely (CR and electric equivalent circuit models, TTC model,), are used and compared. Such an assessment is carried out using a numerical example referring to IEEE 13 buses distribution test feeder suitably adapted to include stochastic generation and BESSs.

It is shown that, for the considered operation scenarios, the proposed grid control method provides feasible voltage and current profiles. The control coupled with the TTC model leads to slightly worst voltage profiles due to the limiting action of the BESS DC constraints. However, the solution provided by this controller always satisfy the operational limits of the BESSs and, therefore, provide feasible solutions with respect to the constraints of these devices. On the contrary, the adoption of the CR model might provide unfeasible solution since the DC voltage/current limits of BESSs may not be respected.

4.2 Contribution

The main contributions of the thesis are as summarized below:

- Proposing a generic charge representative model for any electrochemical ESSs. CR model accounts for a stable and accurate SoC estimation framework.

- Proposing an accurate modeling of the redistribution phenomenon of the supercapacitor residual charge during charging/discharging and relaxation phases. Experimentally observed results are used as inputs for the development of an improved version of one of the RC-equivalent circuit models.

- Proposing an improvement of the most common electric equivalent circuit used for Lithium-based batteries. The improvement is based on the modeling of the so-called charge redistribution phenomenon.

- Proposing a network partitioning strategy for the optimal voltage control of ADNs by means of ESSs with the aim of limiting the information exchange only at the interfacing nodes between adjacent areas.

- Proposing two decentralized optimal scheduling algorithms relying, respectively, on the Thévenin equivalents and a recursive approach.

- Proposing a real-time decentralized voltage control and line congestion management algorithm in multi-area active distribution network relying on an accurate dynamic model of BESSs capable to account for their DC active power limits.

4.3 Future Works

In the continuation of this work, the following topics are suggested for further possible research and potential industrial applications:

- The proposed models for supercapacitors and batteries could be enhanced accounting for temperature variations in parameter assessment procedure.

- Referring to the control/scheduling methods, this works used ESSs as the only controllable devices in ADNs. The use of ESSs could be combined with other control approaches such as demand response algorithms. Each of controllable loads and ESSs can be considered as agents.

- In this thesis, DGs and loads are modeled as voltage-independent active power injections with null reactive component. They could be improved accounting for their detailed models.

- Accounting for the cost of communication among areas in the proposed algorithms could be enhanced the performance of the algorithms.

- In the proposed zonal control problem, all nodes voltages and all line currents are controlled by the area agents. This procedure can be simplified by defining pilot buses in an area. The control of all nodes voltages and all line currents can be achieved only by controlling the pilot buses.

- In the optimization control problems, considering other objectives like line losses reduction or high voltage power reduction can make the problem more mature.

- A close scrutiny is required in case of communication failure among areas.

- Integration of hybrid Battery/Supercapacitor Energy Storage Systems can be considered as an alternative solution to take advantage of the high energy/power densities of both devices.

- Comprehensive systemic testing and evaluation through using real large scale power distribution networks and numerous distributed generators with different energy resources and supply capabilities can be an added value to the proposed methods.

5 Appendices

5.1 Appendix A.

In this thesis, it is claimed that VIF accounts for both active and reactive powers using(3.3). This can be numerically verified by using the simple 4 nodes test system shown in Figure 5-1 with PV injections at node 3 and DESS placed at node 2. The line parameters and also load data for a specific time step are given in Table 4 and

Table 5. The SoC of the DESS is 0.5. For a specific time step, $VIF_{2\rightarrow4}^{P}$ and $VIF_{2\rightarrow4}^{Q}$ are calculated. By computing the electric line distance ($\alpha_{2\rightarrow4}$ and $\beta_{2\rightarrow4}$), $VIF_{2\rightarrow4}$ is obtained. The $VIF_{2\rightarrow4}$ as a function of R/X ratio of line 2-4 is shown in Figure 5-2. It is seen that the when the R/X ratio increases (decreases), the $VIF_{2\rightarrow4}$ tends to $VIF_{2\rightarrow4}^{P}$ ($VIF_{2\rightarrow4}^{Q}$). From the figure, it is obvious that the $VIF_{2\rightarrow4}$ accounts for both $VIF_{2\rightarrow4}^{P}$ and $VIF_{2\rightarrow4}^{Q}$ considering the electric line distance using(3.3).

Table 4: 4 node test load data

Node	1	2	3	4
P (kW)	-	20	20	30
Q (kVar)	-	30	10	20

Appendices

Table 5: 4 node test line data

line	R	X	B
1-2	0.010014	0.023594	0.0000014
2-3	0.018183	0.018434	0.00000074
3-4	0.018546	0.014747	0.00000059

5.2 Appendix B.

Centralized control formulation:

$$\min_{\substack{P^{ac}_{BESS_i}(t),Q^{ac}_{BESS_i}(t) \\ P^{ac}_{Ex}(t)}} \beta_1\Gamma'(t)+\beta_2\Upsilon'(t)+\beta_3H'(t)+\beta_4\Psi'(t) \tag{5.1}$$

s.t
$$a) \quad SoE^{min}_i \le SoE_i(t) \le SoE^{max}_i$$
$$b) \quad P^{ac}_{BESS_i}(t)^2 + Q^{ac}_{BESS_i}(t)^2 \le S_{conv_i}{}^2$$
$$c) \quad P^{dc,min}_{BESS_i}(t) \le P^{dc}_{BESS_i}(t) \le P^{dc,max}_{BESS_i}(t)$$
$$d) \quad |I_{sr}(t)| \le I^{max}_{sr}$$

$\beta_1,\beta_2,\beta_3,\beta_4$ are weighting the terms of the objective function. i={1,...,B} where B is the number of DESSs in the system. In the control optimization problem formulated by (5.1), the constraints are related to the SoE limits, PQ capability curve of the power converters, BESSs DC active power limits, and line current ampacity limits respectively are modeled by (5.1. a-d)

The objective function includes:

a) BESS operation cost ($\Gamma'(t)$). It is defined by (5.2) for each BESS.

$$\Gamma'_i(t)= \sum_{i\in B,t} k_i\left(SoE_i(t)-SoE_{ref_i}\right)^4 \cdot \left(a_i \cdot SoE_i(t)^2 - b_i \cdot SoE_i(t)+c_i\right) \tag{5.2}$$

Where a_i,b_i,c_i are constant.

b) Nodes voltages regulations ($\Upsilon'(t)$) are obtained by (5.3)-(5.5).

118

$$\Upsilon'\left(t\right)=\sum_{j\in N,t}\left\|\ \left|\overline{V}_{j}\left(t\right)\right|-V_{ref}\ \right\|^{2} \tag{5.3}$$

$$\left|\overline{V}_{j}\left(t\right)\right|=\left|\overline{V}_{j}^{init}\left(t\right)\right|+\Delta\left|\overline{V}_{j}\left(t\right)\right| \tag{5.4}$$

$$\Delta\left|\overline{V}_{j}\left(t\right)\right|=\sum_{i=1}^{B}\left(P_{BESS,i}^{ac}\left(t\right)\cdot VSC_{i\to j}^{P}+Q_{BESS,i}^{ac}\left(t\right)\cdot VSC_{i\to j}^{Q}\right) \tag{5.5}$$

c) It should be noted that in the decentralized formulation each area accounts for the active/reactive power limits they can import/export to/from its neighbors. To this end, in order to have an accurate comparison with the centralized method, we have to consider the energy cost imported from the external grid considered to be the upper sub-transmission network. In this respect, the imported energy cost from the external grid $\left(\mathrm{H}'\left(t\right)\right)$ is computed using the following equation.

$$\mathrm{H}'\left(t\right)=\lambda'\cdot P_{Ex}^{ac}\left(t\right)^{2} \tag{5.6}$$

d) Lines current flow regulation $\left(\Psi'\left(t\right)\right)$ obtained by (5.7)-(5.9).

$$\Psi'\left(t\right)=\sum_{s,r\in N,t}\left\|\ \left|\overline{I_{sr}}\left(t\right)\right|\ \right\|^{2} \tag{5.7}$$

$$\left|\overline{I}_{sr}\left(t\right)\right|=\left|\overline{I}_{sr}^{init}\left(t\right)\right|+\Delta\left|\overline{I}_{sr}\left(t\right)\right| \tag{5.8}$$

$$\Delta\left|\overline{I}_{sr}\left(t\right)\right|=\sum_{i=1}^{B}\left(P_{BESS,i}^{ac}\left(t\right)\cdot\Pi_{i\to sr}^{P}+Q_{BESS,i}^{ac}\left(t\right)\cdot\Pi_{i\to sr}^{Q}\right) \tag{5.9}$$
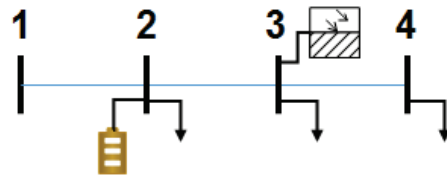
Figure 5-1 4 node test system adopted to numerically verify the correctness of equation (3.3)
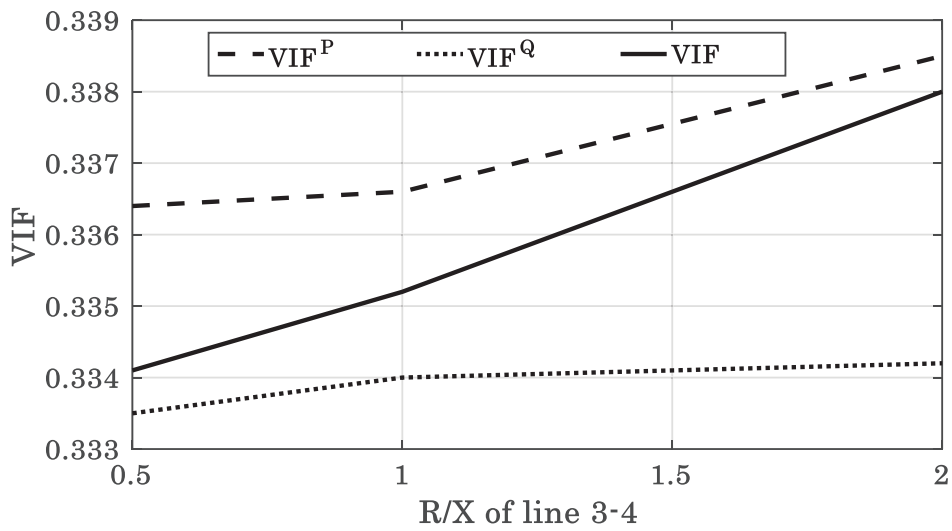

Figure 5-2 Numerical verification of the VIF computation with respect to the four node test system shown in Figure 5-1

Bibliography

[1]   P. Basak, S. Chowdhury, S. Halder nee Dey, and S. P. Chowdhury, "A literature review on integration of distributed energy resources in the perspective of control, protection and stability of microgrid," *Renew. Sustain. Energy Rev.*, vol. 16, no. 8, pp. 5545–5556, Oct. 2012.

[2]   C. L. Masters, "Voltage rise: the big issue when connecting embedded generation to long 11 kV overhead lines," *Power Eng. J.*, vol. 16, no. 1, pp. 5–12, Feb. 2002.

[3]   S. D. Ramchurn, P. Vytelingum, A. Rogers, and N. Jennings, "Agent-based control for decentralised demand side management in the smart grid," in *The 10th International Conference on Autonomous Agents and Multiagent Systems*, 2011, vol. 1, pp. 5–12.

[4]   N. Hatziargyriou, "Microgrids : Architectures and Control," no. Wiley-IEEE Press, p. 340 pages, 2014.

[5]   F. Ren, M. Zhang, and D. Sutanto, "A Multi-Agent Approach for Decentralized Voltage Regulation in Power Distribution Networks with Distributed Generators," in *Twelfth International Conference on Autonomous Agents and Multiagent Systems*, 2013, pp. 1111–1112.

[6]   E. S. 50160, "Voltage characteristics of electricity supplied by public distribution systems," 2010.

[7]   A. S. Bouhouras, C. Iraklis1, G. Evmiridis, and D. P. Labridis, "Mitigating Distribution Network Congestion due to High DG Penetration," in *9th Mediterranean Conference and Exhibition on Power Generation, Transmission, Distribution and Energy Conversion (Med Power 2014), Athens - Greece*, 2014, no. November.

[8]   H. E. Farag, E. F. El-Saadany, and R. Seethapathy, "A Two Ways Communication-Based Distributed Control for Voltage Regulation in Smart Distribution Feeders," *IEEE Trans. Smart Grid*, vol. 3, no. 1, pp. 271–281, Mar. 2012.

[9]   S. Deshmukh, B. Natarajan, and A. Pahwa, "Voltage/VAR Control in Distribution Networks via Reactive Power Injection Through Distributed Generators," *IEEE Trans. Smart Grid*, vol. 3, no. 3, pp. 1226–1234, Sep. 2012.

[10]   D. T. Rizy and J. D. Kueck, "Adaptive Voltage Control With Distributed Energy Resources: Algorithm, Theoretical Analysis, Simulation, and Field Test Verification," *IEEE Trans. Power Syst.*, vol. 25, no. 3, pp. 1638–1647, Aug. 2010.

[11]   M. E. Baran and I. M. El-Markabi, "A Multiagent-Based Dispatching Scheme for Distributed Generators for Voltage Support on Distribution Feeders," *IEEE Trans. Power Syst.*, vol. 22, no. 1, pp. 52–59, Feb. 2007.

[12]   P. N. Vovos, A. E. Kiprakis, A. R. Wallace, and G. P. Harrison, "Centralized and Distributed Voltage Control: Impact on Distributed Generation Penetration," *IEEE Trans. Power Syst.*, vol. 22, no. 1, pp. 476–483, Feb. 2007.

[13]   A. E. Kiprakis and A. R. Wallace, "Maximising energy capture from distributed generators

in weak networks," *IEE Proc. Gener. Transm. Distrib.*, vol. 151, no. 5, 2004.

[14] Q. Fu, L. F. Montoya, A. Solanki, A. Nasiri, V. Bhavaraju, T. Abdallah, and D. C. Yu, "Microgrid Generation Capacity Design With Renewables and Energy Storage Addressing Power Quality and Surety," *IEEE Trans. smart grid*, vol. 3, no. 4, pp. 2019–2027, 2012.

[15] M. H. Shariatkhah and M. R. Haghifam, "Using feeder reconfiguration for congestion management of smart distribution network with high DG penetration," in *CIRED 2012 Workshop: Integration of Renewables into the Distribution Grid*, 2012, pp. 316–316.

[16] S. K. Salman, F. Jiang, and W. J. S. Rogers, "The Effect Of Private Generators Ohf The Voltage Control Of 11 KV Network And On The Operation Of Certain Protective Relays," in *Proceedings. Joint International Power Conference Athens Power Tech,* 1993, vol. 2, pp. 591–595.

[17] K. Pandiaraj and B. Fox, "Novel voltage control for embedded generators in rural distribution networks and on the operation of certain protective relays," in *PowerCon 2000. 2000 International Conference on Power System Technology. Proceedings (Cat. No.00EX409)*, 2000, vol. 1, pp. 457–462.

[18] S. K. Salman and I. M. Rida, "ANN-based AVC relay for voltage control of distribution network with and without embedded generation," in *DRPT2000. International Conference on Electric Utility Deregulation and Restructuring and Power Technologies. Proceedings (Cat. No.00EX382)*, 2000, pp. 263–267.

[19] K. T. Tan, P. L. So, Y. C. Chu, and M. Z. Q. Chen, "Coordinated Control and Energy Management of Distributed Generation Inverters in a Microgrid," *IEEE Trans. Power Deliv.*, vol. 28, no. 2, pp. 704–713, Apr. 2013.

[20] J. F. Manwell and J. G. McGowan, "Lead acid battery storage model for hybrid energy systems," *Sol. Energy*, vol. 50, no. 5, pp. 399–405, May 1993.

[21] J. Zhang and J. Lee, "A review on prognostics and health monitoring of Li-ion battery," *J. Power Sources*, vol. 196, no. 15, pp. 6007–6014, Aug. 2011.

[22] L. Lu, X. Han, J. Li, J. Hua, and M. Ouyang, "A review on the key issues for lithium-ion battery management in electric vehicles," *J. Power Sources*, vol. 226, pp. 272–288, Mar. 2013.

[23] W. Waag, C. Fleischer, and D. U. Sauer, "Critical review of the methods for monitoring of lithium-ion batteries in electric and hybrid vehicles," *J. Power Sources*, vol. 258, pp. 321–339, Jul. 2014.

[24] V. Pop, H. J. Bergveld, P. H. L. Notten, and P. P. L. Regtien, "State-of-the-art of battery state-of-charge determination," *Meas. Sci. Technol.*, vol. 16, no. 12, pp. R93–R110, Dec. 2005.

[25] S. Piller, M. Perrin, and A. Jossen, "Methods for state-of-charge determination and their applications," *J. Power Sources*, vol. 96, pp. 113–120, 2001.

[26] J. Chiasson and B. Vairamohan, "Estimating the state of charge of a battery," *IEEE Trans. Control Syst. Technol.*, vol. 13, no. 3, pp. 465–470, May 2005.

[27] J. Alzieu and H. Smimite, "Improvement of intelligent battery controller : state-of-charge indicator and associated functions," *J. Power Sources*, vol. 67, pp. 157–161, 1997.

[28] V. H. Johnson, "Battery performance models in ADVISOR," *J. Power Sources*, vol. 110, pp. 321–329, 2002.

[29] B. Belvedere, M. Bianchi, A. Borghetti, C. A. Nucci, M. Paolone, and A. Peretto, "A Microcontroller-Based Power Management System for Standalone Microgrids With Hybrid Power Supply," *IEEE Trans. Sustain. ENERGY*, vol. 3, no. 3, pp. 422–431, 2012.

[30] J. Wang, B. Cao, Q. Chen, and F. Wang, "Combined state of charge estimator for electric vehicle battery pack," *Control Eng. Pract.*, vol. 15, no. 12, pp. 1569–1576, Dec. 2007.

[31]   Y. Xing, W. He, M. Pecht, and K. L. Tsui, "State of charge estimation of lithium-ion batteries using the open-circuit voltage at various ambient temperatures," *Appl. Energy*, vol. 113, pp. 106–115, Jan. 2014.

[32]   I. Snihir, W. Rey, E. Verbitskiy, A. Belfadhel-Ayeb, and P. H. L. Notten, "Battery open-circuit voltage estimation by a method of statistical analysis," *J. Power Sources*, vol. 159, no. 2, pp. 1484–1487, Sep. 2006.

[33]   F. Baronti and M. Chow, "Modeling and Online Parameter Identification of Li-Polymer Battery Cells for SOC estimation," pp. 1336–1341.

[34]   K. Kutluay, Y. Çadırcı, Y. S. Özkazanç, and I. Çadırcı, "A New Online State-of-Charge Estimation and Monitoring System for Sealed Lead – Acid Batteries in Telecommunication Power Supplies," vol. 52, no. 5, pp. 1315–1327, 2005.

[35]   V. Pop, H. J. Bergveld, J. H. G. Op het Veld, P. P. L. Regtien, D. Danilov, and P. H. L. Notten, "Modeling Battery Behavior for Accurate State-of-Charge Indication," *J. Electrochem. Soc.*, vol. 153, no. 11, p. A2013, 2006.

[36]   T. B. Reddy, "Linden's Handbook of Batteries," *Ed. New York: McGraw-Hill*, 2001. [Online]. Available: http://accessengineeringlibrary.com/browse/lindens-handbook-of-batteries-fourth-edition. [Accessed: 09-Feb-2016].

[37]   Z. Li and J. Chen, "An impedance-based approach to predict the state-of-charge for carbon-based supercapacitors," *Microelectron. Eng.*, vol. 85, no. 7, pp. 1549–1554, Jul. 2008.

[38]   B. E. Willihnganz, "A Bridge for Measuring Storage Battery Resistance," no. 1940, pp. 253–258, 1941.

[39]   S. Buller, M. Thele, and R. W. A. A. De Doncker, "Impedance-Based Simulation Models of Supercapacitors and Li-Ion Batteries for Power Electronic Applications," vol. 41, no. 3, pp. 742–747, 2005.

[40]   B. Le Gorrec, "Constant load vs constant current EIS study of electrochemical battery discharge," vol. 42, pp. 3417–3420, 1997.

[41]   F. Huet, "A review of impedance measurements for determination of the state-of-charge or state-of-health of secondary batteries," *J. Power Sources*, vol. 70, no. 1, pp. 59–69, Jan. 1998.

[42]   S. Rodrigues, N. Munichandraiah, and A. K. Shukla, "A review of state-of-charge indication of batteries by means of a.c. impedance measurements," *J. Power Sources*, vol. 87, no. 1–2, pp. 12–20, Apr. 2000.

[43]   A. Eddahech, O. Briat, and J. M. Vinassa, "Adaptive Voltage Estimation for EV Li-ion Cell Based on Artificial Neural Networks State-of- Charge Meter," pp. 1318–1324, 2012.

[44]   J. C. Alvarez, "Support Vector Machines Used to Estimate the Battery State of Charge," vol. 28, no. 12, pp. 5919–5926, 2013.

[45]   C. Chan, E. . Lo, and S. Weixiang, "The available capacity computation model based on artificial neural network for lead–acid batteries in electric vehicles," *J. Power Sources*, vol. 87, no. 1–2, pp. 201–204, Apr. 2000.

[46]   T. Hansen and C.-J. Wang, "Support vector based battery state of charge estimator," *J. Power Sources*, vol. 141, no. 2, pp. 351–358, Mar. 2005.

[47]   K. S. Ng, C.-S. Moo, Y.-P. Chen, and Y.-C. Hsieh, "Enhanced coulomb counting method for estimating state-of-charge and state-of-health of lithium-ion batteries," *Appl. Energy*, vol. 86, no. 9, pp. 1506–1511, Sep. 2009.

[48]   A. J. Salkind, C. Fennie, P. Singh, T. Atwater, and D. E. Reisner, "Determination of state-of-charge and state-of-health of batteries by fuzzy logic methodology," pp. 293–300, 1999.

[49]   K. M. Tsang, L. Sun, and W. L. Chan, "Identification and modelling of Lithium ion

battery," *Energy Convers. Manag.*, vol. 51, no. 12, pp. 2857–2862, Dec. 2010.

[50]   G. L. Plett, "Extended Kalman filtering for battery management systems of LiPB-based HEV battery packs: Part 1," *J. Power Sources*, vol. 134, no. 2, pp. 252–261, Aug. 2004.

[51]   G. L. Plett, "Extended Kalman filtering for battery management systems of LiPB-based HEV battery packs : Part 2," *J. Power Sources*, vol. 134, no. 2, pp. 262–276, Aug. 2004.

[52]   G. L. Plett, "Extended Kalman filtering for battery management systems of LiPB-based HEV battery packs: Part 3," *J. Power Sources*, vol. 134, no. 2, pp. 277–292, Aug. 2004.

[53]   G. L. Plett, "Sigma-point Kalman filtering for battery management systems of LiPB-based HEV battery packs Part1: Introduction and state estimation," *J. Power Sources*, vol. 161, no. 2, pp. 1356–1368, Oct. 2006.

[54]   G. L. Plett, "Sigma-point Kalman filtering for battery management systems of LiPB-based HEV battery packs: Part 2: Simultaneous state and parameter estimation," *J. Power Sources*, vol. 161, no. 2, pp. 1369–1384, Oct. 2006.

[55]   Z. He, M. Gao, C. Wang, L. Wang, and Y. Liu, "Adaptive State of Charge Estimation for Li-Ion Batteries Based on an Unscented Kalman Filter with an Enhanced Battery Model," *Energies*, vol. 6, no. 8, pp. 4134–4151, Aug. 2013.

[56]   J. Han, D. Kim, and M. Sunwoo, "State-of-charge estimation of lead-acid batteries using an adaptive extended Kalman filter," *J. Power Sources*, vol. 188, no. 2, pp. 606–612, Mar. 2009.

[57]   F. Sun, X. Hu, Y. Zou, and S. Li, "Adaptive unscented Kalman filtering for state of charge estimation of a lithium-ion battery for electric vehicles," *Energy*, vol. 36, no. 5, pp. 3531–3540, May 2011.

[58]   S. Schwunk, N. Armbruster, S. Straub, J. Kehl, and M. Vetter, "Particle filter for state of charge and state of health estimation for lithium–iron phosphate batteries," *J. Power Sources*, vol. 239, pp. 705–710, Oct. 2013.

[59]   B. Xia, C. Chen, Y. Tian, W. Sun, Z. Xu, and W. Zheng, "A novel method for state of charge estimation of lithium-ion batteries using a nonlinear observer," *J. Power Sources*, vol. 270, pp. 359–366, Dec. 2014.

[60]   I.-S. Kim, "The novel state of charge estimation method for lithium battery using sliding mode observer," *J. Power Sources*, vol. 163, no. 1, pp. 584–590, Dec. 2006.

[61]   Y. He, X. Liu, C. Zhang, and Z. Chen, "A new model for State-of-Charge (SOC) estimation for high-power Li-ion batteries," *Appl. Energy*, vol. 101, pp. 808–814, Jan. 2013.

[62]   G. L. Plett, "Dual and Joint EKF for Simultaneous SOC and SOH Estimation," *S. Haykin (Ed.), Kalman Filter. neural networks, Wiley/Inter-Science, New York*, pp. 123–164, 2001.

[63]   K. A. Smith, C. D. Rahn, and C. Wang, "Model-Based Electrochemical Estimation of Lithium Ion Batteries," in *IEEE International Conference on Control Applications*, 2008, no. 1, pp. 714–719.

[64]   R. Klein, N. a. Chaturvedi, J. Christensen, J. Ahmed, R. Findeisen, and A. Kojic, "Electrochemical Model Based Observer Design for a Lithium-Ion Battery," *IEEE Trans. Control Syst. Technol.*, vol. 21, no. 2, pp. 289–301, Mar. 2013.

[65]   J. Kalawoun, K. Biletska, F. Suard, and M. Montaru, "From a novel classification of the battery state of charge estimators toward a conception of an ideal one," *J. Power Sources*, vol. 279, pp. 694–706, Apr. 2015.

[66]   F. Zhang, G. Liu, and M. Ieee, "A battery State of Charge estimation method with extended Kalman filter," *IEEE/ASME Int. Conf. Adv. Intell. Mechatronics*, pp. 1008–1013, Jul. 2008.

[67]   M. Gholizadeh and F. R. Salmasi, "Estimation of state of charge, unknown nonlinearities, and state of health of a lithium-ion battery based on a comprehensive unobservable

model," *IEEE Trans. Ind. Electron.*, vol. 61, no. 3, pp. 1335–1344, 2014.

[68]   F. Adinolfi, F. Conte, S. Massucco, M. Saviozzi, F. Silvestro, and P. Milano, "Performance Evaluation of Algorithms for the State of Charge Estimation of Storage Devices in Microgrid Operation."

[69]   D. Di Domenico, G. Fiengo, and A. Stefanopoulou, "Lithium-ion battery state of charge estimation with a Kalman Filter based on a electrochemical model," in *2008 IEEE International Conference on Control Applications*, 2008, pp. 702–707.

[70]   "Nesscap Ultracapacitors." [Online]. Available: http://www.nesscap.com/. [Accessed: 08-Mar-2016].

[71]   M. Inagaki and F. Kang, *Materials Science and Engineering of Carbon: Fundamentals*. Elsevier Science, 2014.

[72]   R. de Levie, "On porous electrodes in electrolyte solutions," *Electrochim. Acta*, vol. 8, no. 10, pp. 751–780, Oct. 1963.

[73]   B. W. Ricketts and C. Ton-That, "Self-discharge of carbon-based supercapacitors with organic electrolytes," *J. Power Sources*, vol. 89, no. 1, pp. 64–69, Jul. 2000.

[74]   M. Kaus, J. Kowal, and D. U. Sauer, "Modelling the effects of charge redistribution during self-discharge of supercapacitors," *Electrochim. Acta*, vol. 55, no. 25, pp. 7516–7523, Oct. 2010.

[75]   B. E. Conway, "Electrochemical Supercapacitors - Scientific Fundamentals and | B. E. Conway | Springer," 1999. [Online]. Available: http://www.springer.com/cn/book/9780306457364. [Accessed: 24-Jan-2016].

[76]   S. Buller, E. Karden, D. Kok, and R. W. De Doncker, "Modeling the dynamic behavior of supercapacitors using impedance spectroscopy," *IEEE Trans. Ind. Appl.*, vol. 38, no. 6, pp. 1622–1626, Nov. 2002.

[77]   D. B. Robinson, "Optimization of power and energy densities in supercapacitors," *J. Power Sources*, vol. 195, no. 11, pp. 3748–3756, Jun. 2010.

[78]   J. Black and H. A. Andreas, "Prediction of the self-discharge profile of an electrochemical capacitor electrode in the presence of both activation-controlled discharge and charge redistribution," *J. Power Sources*, vol. 195, no. 3, pp. 929–935, Feb. 2010.

[79]   J. R. Miller, "Electrochemical Capacitor Power Performance: Stability as a Function of Temperature, Voltage, and Operating Time," in *International Seminar on Double-Layer Capacitors and Similar Energy Storage Devices*, 1993.

[80]   L. Zubieta and R. Bonert, "Characterization of double-layer capacitors for power electronics applications," *IEEE Trans. Ind. Appl.*, vol. 36, no. 1, pp. 199–205, 2000.

[81]   F. Belhachemi, S. Rael, and B. Davat, "A physical based model of power electric double-layer supercapacitors," in *Conference Record of the 2000 IEEE Industry Applications Conference. Thirty-Fifth IAS Annual Meeting and World Conference on Industrial Applications of Electrical Energy (Cat. No.00CH37129)*, 2000, vol. 5, pp. 3069–3076.

[82]   F. Rafik, H. Gualous, R. Gallay, A. Crausaz, and A. Berthon, "Frequency, thermal and voltage supercapacitor characterization and modeling," *J. Power Sources*, vol. 165, no. 2, pp. 928–934, Mar. 2007.

[83]   Sang-Hyun Kim, Woojin Choi, Kyo-Bum Lee, and Sewan Choi, "Advanced Dynamic Simulation of Supercapacitors Considering Parameter Variation and Self-Discharge," *IEEE Trans. Power Electron.*, vol. 26, no. 11, pp. 3377–3385, Nov. 2011.

[84]   A. S. Weddell, G. V. Merrett, T. J. Kazmierski, and B. M. Al-Hashimi, "Accurate Supercapacitor Modeling for Energy Harvesting Wireless Sensor Nodes," *IEEE Trans. Circuits Syst. II Express Briefs*, vol. 58, no. 12, pp. 911–915, Dec. 2011.

[85]   V. Musolino, L. Piegari, and E. Tironi, "New Full-Frequency-Range Supercapacitor Model With Easy Identification Procedure," *IEEE Trans. Ind. Electron.*, vol. 60, no. 1, pp.

112–120, Jan. 2013.

[86] B. Pillay, "The Influence of Side Reactions on the Performance of Electrochemical Double-Layer Capacitors," *J. Electrochem. Soc.*, vol. 143, no. 6, p. 1806, Jun. 1996.

[87] A. M. Johnson and J. Newman, "Desalting by Means of Porous Carbon Electrodes," *J. Electrochem. Soc.*, vol. 118, no. 3, p. 510, Mar. 1971.

[88] D. Dunn and J. Newman, "Predictions of Specific Energies and Specific Powers of Double-Layer Capacitors Using a Simplified Model," *J. Electrochem. Soc.*, vol. 147, no. 3, p. 820, Mar. 2000.

[89] S. Devan, V. R. Subramanian, and R. E. White, "Analytical Solution for the Impedance of a Porous Electrode," *J. Electrochem. Soc.*, vol. 151, no. 6, p. A905, Jun. 2004.

[90] H. Kim and B. N. Popov, "A Mathematical Model of Oxide/Carbon Composite Electrode for Supercapacitors," *J. Electrochem. Soc.*, vol. 150, no. 9, p. A1153, Sep. 2003.

[91] C. Lin, B. N. Popov, and H. J. Ploehn, "Modeling the Effects of Electrode Composition and Pore Structure on the Performance of Electrochemical Capacitors," *J. Electrochem. Soc.*, vol. 149, no. 2, p. A167, Feb. 2002.

[92] C. Lin, "A Mathematical Model of an Electrochemical Capacitor with Double-Layer and Faradaic Processes," *J. Electrochem. Soc.*, vol. 146, no. 9, p. 3168, Sep. 1999.

[93] V. Srinivasan, "Mathematical Modeling of Electrochemical Capacitors," *J. Electrochem. Soc.*, vol. 146, no. 5, p. 1650, May 1999.

[94] A. R. Sparacino, G. F. Reed, R. J. Kerestes, and Z. T. Smith, "Survey of Battery Energy Storage Systems and Modeling Techniques," in *IEEE Power and Energy Society General Meeting*, 2012, pp. 1–8.

[95] B. R. H. M.R. Jongerden, "Which battery model to use?," *UKPE 2008, Imp. Coll. London, DTR08-9*, pp. 76–88, 2008.

[96] T. F. Fuller, M. Doyle, and J. Newma, "Relaxation Phenomena in Lithium-Ion-Insertion Cells," *J. Electrochem. Soc.*, vol. 141, no. 4, p. 982, Apr. 1994.

[97] C. Speltino, D. Di Domenico, G. Fiengo, and A. Stefanopoulou, "Experimental identification and validation of an electrochemical model of a Lithium-Ion Battery," *Control Conference (ECC), 2009 European*. pp. 1053–1058, 2009.

[98] Tae-Kyung Lee, "Development and implementation of control-oriented electrochemical battery models in a battery management system," in *2015 American Control Conference (ACC)*, 2015, pp. 717–722.

[99] J. Newman and K. E. Thomas-Alyea, *Electrochemical Systems*, 3rd ed. .

[100] D. W. Dees, V. S. Battaglia, and A. Bélanger, "Electrochemical modeling of lithium polymer batteries," *J. Power Sources*, vol. 110, no. 2, pp. 310–320, Aug. 2002.

[101] T. F. Fuller, M. Doyle, and N. John, "Simulation and Optimization of the Dual Lithium Ion Insertion Cell," *J. Electrochem. Soc.*, vol. 141, no. 1, p. 1, Jan. 1994.

[102] M. Doyle, T. F. Fuller, and J. Newman, "Modeling of Galvanostatic Charge and Discharge of the Lithium/Polymer/Insertion Cell," *J. Electrochem. Soc.*, vol. 140, no. 6, p. 1526, Jun. 1993.

[103] J. F. Manwell and J. G. Mcgowan, "Extension of the Kinetic Battery Model for Wind/Hybrid Power Systems," Jan. 1994.

[104] H. Zimmerman and R. Peterson, "An electrochemical cell equivalent circuit for storage battery/power system calculations by digital computer," in *13th Intersociety Energy Conversion Engineering Conference*, 1978, pp. 33–38.

[105] J. Appelbaum and R. Weiss, "An Electrical Model of the Lead-Acid Battery," in *INTELEC '82 - International Telecommunications Energy Conference*, 1982, pp. 304–307.

[106] Z. M. Salameh, M. a. Casacca, and W. a. Lynch, "A mathematical model for lead-acid batteries," *IEEE Trans. Energy Convers.*, vol. 7, no. 1, pp. 93–98, Mar. 1992.

[107] S. C. Hageman, "Simple PSpice models let you simulate common battery types," *Electron. Des. News*, vol. 38, pp. 117–129, Oct. 1993.

[108] P. Baudry, M. Neri, M. Gueguen, and G. Lonchampt, "Electro-thermal modelling of polymer lithium batteries for starting period and pulse power," *J. Power Sources*, vol. 54, no. 2, pp. 393–396, Apr. 1995.

[109] M. C. Glass, "Battery Electrochemical Nonlinear/Dynamic Spice Model," in *31st Intersociety Energy Conversion Engineering Conference, IECEC 96.*, 1996, pp. 292–297.

[110] S. Gold, "A PSPICE macromodel for lithium-ion batteries," in *The Twelfth Annual Battery Conference on Applications and Advances*, 1997, pp. 215–222.

[111] M. Ceraolo, "New dynamical models of lead-acid batteries," *IEEE Trans. Power Syst.*, vol. 15, no. 4, pp. 1184–1190, 2000.

[112] S. Abu-Sharkh and D. Doerffel, "Rapid test and non-linear model characterisation of solid-state lithium-ion batteries," *J. Power Sources*, vol. 130, no. 1–2, pp. 266–274, May 2004.

[113] G. A. R.-M. Min Chen, "Accurate Electrical Battery Model Capable of Predicting Runtime and I–V Performance," *IEEE Trans. Energy Convers.*, vol. 21, no. 2, pp. 504–511, 2006.

[114] J. Zhang, S. Ci, H. Sharif, and M. Alahmad, "An enhanced circuit-based model for single-cell battery," in *2010 Twenty-Fifth Annual IEEE Applied Power Electronics Conference and Exposition (APEC)*, 2010, pp. 672–675.

[115] W. Q. Taesic Kim, "A Hybrid Battery Model Capable of Capturing Dynamic Circuit Characteristics and Nonlinear Capacity Effects," *IEEE Trans. ENERGY Convers.*, vol. 26, no. 4, pp. 1172–1180, 2011.

[116] T. Huria, M. Ceraolo, J. Gazzarri, and R. Jackey, "High Fidelity Electrical Model with Thermal Dependence for Characterization and Simula- tion of High Power Lithium Battery Cells," in *IEEE International Electric Vehicle Conference (IEVC)*, 2012, pp. 1–8.

[117] C.-J. Zhan, X. G. Wu, S. Kromlidis, V. K. Ramachandaramurthy, M. Barnes, N. Jenkins, and A. J. Ruddell, "Two electrical models of the lead–acid battery used in a dynamic voltage restorer," *IEE Proc. - Gener. Transm. Distrib.*, vol. 150, no. 2, p. 175, 2003.

[118] A. Rahmoun and H. Biechl, "Modelling of Li-ion batteries using equivalent circuit diagrams," *Prz. Elektrotechniczn*, vol. 2, no. 7, pp. 152–156, 2012.

[119] S. Barsali and M. Ceraolo, "Dynamical models of lead-acid batteries: implementation issues," *IEEE Trans. Energy Convers.*, vol. 17, no. 1, pp. 16–23, Mar. 2002.

[120] F. V. C. Markus Einhorn Christian Kral,Jurgen Fleig, "Comparison, Selection, and Parameterization of Electrical Battery Models for Automotive Applications," *IEEE Trans. POWER Electron.*, vol. 28, no. 3, pp. 1429–1437, 2013.

[121] T. Tsuji, K. Tomura, T. Oyama, T. Hashiguchi, T. Goda, S. Tange, and T. Nomura, "A study of centralized voltage profile control of distribution network considering dynamics of distributed generator," *Electr. Eng. Japan*, vol. 179, no. 1, pp. 29–39, Apr. 2012.

[122] T. Sansawatt, L. F. Ochoa, and G. P. Harrison, "Smart Decentralized Control of DG for Voltage and Thermal Constraint Management," *IEEE Trans. Power Syst.*, vol. 27, no. 3, pp. 1637–1645, 2012.

[123] A. Rogers, S. D. Ramchurn, and N. R. Jennings, "Delivering the Smart Grid : Challenges for Autonomous Agents and Multi-Agent Systems Research," in *26th AAAI Conf. on Artificial Intelligence*, 2003, pp. 2166–2172.

[124] M. Nick, R. Cherkaoui, and M. Paolone, "Optimal Allocation of Dispersed Energy Storage Systems in Active Distribution Networks for Energy Balance and Grid Support," *IEEE Trans. Power Syst.*, vol. 29, no. 5, pp. 2300–2310, 2014.

[125] S. D. J. McArthur, E. M. Davidson, V. M. Catterson, A. L. Dimeas, N. D. Hatziargyriou, F. Ponci, and T. Funabashi, "Multi-Agent Systems for Power Engineering Applications—Part I: Concepts, Approaches, and Technical Challenges," *IEEE Trans. Power Syst.*, vol.

22, no. 4, pp. 1743–1752, Nov. 2007.

[126] W. R. Wagner, A. Keyhani, S. Hao, and T. C. Wong, "A rule-based approach to decentralized voltage control," *IEEE Trans. Power Syst.*, vol. 5, no. 2, pp. 643–651, May 1990.

[127] P. F. Lyons, P. . Taylor, L. . Cipcigan, P. Trichakis, and A. Wilson, "Small Scale Energy Zones and the Impacts of High Concentrations of Small Scale Embedded Generators," in *41st International Universities Power Engineering Conference, .UPEC '06*, 2006, no. 2, pp. 128 – 132.

[128] S. Mei, X. Zhang, and M. Cao, *Power Grid Complexity*, Springer. Tsinghua university press, 2011.

[129] K. Christakou, D. Tomozei, M. Bahramipanah, J.-Y. Le Boudec, and M. Paolone, "Primary Voltage Control in Active Distribution Networks via Broadcast Signals : The Case of Distributed Storage," *IEEE Trans. Smart Grid*, vol. 5, no. 5, pp. 2314–2325, 2014.

[130] T. Wang, P. Zou, and H. Zhou, "A Novel Partitioning Algorithm for Power Grid Using Community Detection," *Adv. Mater. Res.*, vol. 710, pp. 563–566, Jun. 2013.

[131] B. Millar, D. Jiang, and M. E. Haque, "A novel partitioning strategy for distribution networks featuring many small scale generators," in *4rd IEEE PES Innovative Smart Grid Technologies Conference (ISGT)*, 2013, pp. 1–6.

[132] Elvira Kägi-Kolisnyc, "Distribution Management System Including Dispersed Generation and Storage in a Liberalized Market Environment," 2009.

[133] K. Christakou, J.-Y. Le Boudec, M. Paolone, and D.-C. Tomozei, "Efficient Computation of Sensitivity Coefficients of Node Voltages and Line Currents in Unbalanced Radial Electrical Distribution Networks," *IEEE Trans. Smart Grid*, vol. 4, no. 2, pp. 741 – 750, 2012.

[134] A. Borghetti, M. Bosetti, S. Grillo, S. Massucco, C. A. Nucci, M. Paolone, and F. Silvestro, "Short-Term Scheduling and Control of Active Distribution Systems With High Penetration of Renewable Resources," *IEEE Syst. J.*, vol. 4, no. 3, pp. 313–322, 2010.

[135] M. M. Begovic and A. G. Phadke, "Voltage Stability Using Sensitivity Analysis," *IEEE Trans. Power Syst.*, vol. 7, no. 1, pp. 114–123, 1992.

[136] Q. Zhou and J. W. Bialek, "Simplified calculation of voltage and loss sensitivity factors in distribution networks," in *16th Power System Computation Conference (PSCC2008)*, 2008, no. 1, pp. 14–19.

[137] J. Bandler and M. El-Kady, "A unified approach to power system sensitivity analysis and planning , Part I : Family of adjoint systems," in *IEEE Int. Symp. Circuits Syst.*, 1980, pp. 681–687.

[138] J. Tang, F. Ni, F. Ponci, and A. Monti, "Dimension-Adaptive Sparse Grid Interpolation for Uncertainty Quantification in Modern Power Systems : Probabilistic Power Flow," *IEEE Trans. POWER Syst.*, vol. 31, no. 2, pp. 1–13, 2015.

[139] G. Carpinelli, P. Caramia, and P. Varilone, "Multi-linear Monte Carlo simulation method for probabilistic load flow of distribution systems with wind and photovoltaic generation systems," *Renew. Energy*, vol. 76, pp. 283–295, Apr. 2015.

[140] G. Carpinelli, G. Celli, S. Mocci, F. Mottola, F. Pilo, and D. Proto, "Optimal Integration of Distributed Energy Storage Devices in Smart Grids," *IEEE Trans. Smart Grid*, vol. 4, no. 2, pp. 985–995, Jun. 2013.

[141] J. Soares, H. Morais, T. Sousa, Z. Vale, and P. Faria, "Day-ahead resource scheduling including demand response for electric vehicles," in *2014 IEEE PES General Meeting | Conference & Exposition*, 2014, pp. 1–1.

[142] M. C. Bozchalui and R. Sharma, "Operation strategies for energy storage systems in distribution networks," in *2014 IEEE PES General Meeting | Conference & Exposition*,

128

2014, pp. 1–5.

[143] G. Chen, Z. J. Bao, Q. Yang, and W. J. Yan, "Scheduling strategy of hybrid energy storage system for smoothing the output power of wind farm," in *2013 10th IEEE International Conference on Control and Automation (ICCA)*, 2013, pp. 1874–1878.

[144] K. A. Joshi and N. M. Pindoriya, "Day-ahead dispatch of Battery Energy Storage System for peak load shaving and load leveling in low voltage unbalance distribution networks," in *2015 IEEE Power & Energy Society General Meeting*, 2015, pp. 1–5.

[145] M. Nick, R. Cherkaoui, and M. Paolone, "Stochastic day-ahead optimal scheduling of Active Distribution Networks with dispersed energy storage and renewable resources," in *2014 IEEE Conference on Technologies for Sustainability (SusTech)*, 2014, pp. 91–96.

[146] M. Oshiro, T. Senjyu, A. Yona, N. Urasaki, T. Funabashi, and C.-H. Kim, "Optimal operation strategy by battery energy storage systems in distribution system," in *2010 Conference Proceedings IPEC*, 2010, pp. 1199–1204.

[147] G. Celli, S. Mocci, F. Pilo, and M. Loddo, "Optimal integration of energy storage in distribution networks," in *2009 IEEE Bucharest PowerTech*, 2009, pp. 1–7.

[148] A. Gabash and P. Li, "Active-Reactive Optimal Power Flow in Distribution Networks With Embedded Generation and Battery Storage," *IEEE Trans. Power Syst.*, vol. 27, no. 4, pp. 2026–2035, Nov. 2012.

[149] E. Galvan, P. Mandal, T.-L. Tseng, and M. Velez-Reyes, "Energy storage dispatch using adaptive control scheme considering wind-PV in smart distribution network," in *2015 North American Power Symposium (NAPS)*, 2015, pp. 1–6.

[150] S. Goncalves, H. Morais, T. Sousa, and Z. Vale, "Energy resource scheduling in a real distribution network managed by several virtual power players," in *PES T&D 2012*, 2012, pp. 1–8.

[151] T. Logenthiran, D. Srinivasan, A. M. Khambadkone, and H. N. Aung, "Multi-Agent System (MAS) for short-term generation scheduling of a microgrid," in *2010 IEEE International Conference on Sustainable Energy Technologies (ICSET)*, 2010, pp. 1–6.

[152] S. Moghadasi and S. Kamalasadan, "Real-time optimal scheduling of smart power distribution systems using integrated receding horizon control and convex conic programming," in *2014 IEEE Industry Application Society Annual Meeting*, 2014, pp. 1–7.

[153] M. Silva, H. Morais, Z. Vale, and P. Faria, "Short-term scheduling considering five-minute and hour-ahead energy resource management," in *2012 IEEE Power and Energy Society General Meeting*, 2012, pp. 1–8.

[154] T. Logenthiran and D. Srinivasan, "Short term generation scheduling of a Microgrid," in *TENCON 2009 - 2009 IEEE Region 10 Conference*, 2009, pp. 1–6.

[155] E. Kaegi, R. Cherkaoui, and A. Germond, "Decentralized Unit Commitment and Dispatch for the Distribution Systems Using Intelligent Agents Approach," in *PSCC 2008*, 2008, pp. 1–8.

[156] A. Vaccaro, V. Loia, G. Formato, P. Wall, and V. Terzija, "A Self-Organizing Architecture for Decentralized and Monitoring," *IEEE Trans. Ind. INFORMATICS*, vol. 11, no. 1, pp. 289–298, 2015.

[157] F. Perkonigg, D. Brujic, and M. Ristic, "Platform for Multiagent Application Development Incorporating Accurate Communications Modeling," *IEEE Trans. Ind. Informatics*, vol. 11, no. 3, pp. 728–736, 2015.

[158] "IEEE PES Distribution System Analysis Subcommittee's Distribution Test Feeder Working Group."

[159] J. Efberg, "YALMIP : A toolbox for modeling and optimization in MATLAB," in *IEEE International Symposium on Computer Aided Control Systems Design*, 2004, pp. 284–289.

[160] I. Gurobi Optimization, "Gurobi Optimizer Reference Manual," 2012. [Online]. Available: http://www.gurobi.com.

[161] J. Zhao, C. Wang, B. Zhao, F. Lin, Q. Zhou, and Y. Wang, "A Review of Active Management for Distribution Networks: Current Status and Future Development Trends," *Electr. Power Components Syst.*, vol. 42, no. 3–4, pp. 280–293, Feb. 2014.

[162] F. Berthold, M. Carpita, A. Monti, and F. Ponci, "A multi-agent approach to radial feeder voltage control of PEBB-based converter: A real time simulation test," in *2012 IEEE Energy Conversion Congress and Exposition (ECCE)*, 2012, pp. 1990–1997.

[163] Z. Jiang, "Agent-Based Control Framework for Distributed Energy Resources Microgrids," in *2006 IEEE/WIC/ACM International Conference on Intelligent Agent Technology*, 2006, pp. 646–652.

[164] T. Tsuji and T. Goda, "Autonomous Decentralized Voltage Profile Control of Distribution Network considering Time-Delay," in *International Conference on Intelligent Systems Applications to Power Systems, ISAP*, 2007, pp. 1–6.

[165] F. a. Viawan, A. Sannino, and J. Daalder, "Voltage control with on-load tap changers in medium voltage feeders in presence of distributed generation," *Electr. Power Syst. Res.*, vol. 77, no. 10, pp. 1314–1322, Aug. 2007.

[166] M. Bahramipanah, M. Nick, R. Cherkaoui, and M. Paolone, "Network Clustering for Voltage Control in Active Distribution Network Including Energy Storage Systems," in *Innovative Smart Grid Technology IEEE PES Conference ISGT*, 2015.

[167] L. E. Reyes Chamorro, M. Paolone, A. Bernstein, and J.-Y. Le Boudec, "A SuperCapacitor Agent for Providing Real-Time Power Services to the Grid," *IEEE PES Conf. Innov. SMART GRID Technol. ISGT-LA*, vol. -, no. -, pp. 1–6, 2015.

[168] M. Pignati, M. Popovic, S. Barreto Andrade, R. Cherkaoui, D. Flores, J.-Y. Le Boudec, M. M. Maaz, M. Paolone, P. Romano, S. Sarri, T. T. Tesfay, D.-C. Tomozei, and L. Zanni, "Real-Time State Estimation of the EPFL-Campus Medium-Voltage Grid by Using PMUs," in *Innovative Smart Grid Technologies Conference (ISGT)*, 2015, pp. 1–5.

[169] CIGRE WG C6.11 Electra n° 246, "Active Distribution Networks general features, present status of implementation and operation practices," 2009.

[170] A. Abur and A. G. Expósito, *Power System State Estimation : Theory and Implementation*. 2004.

[171] M. N. Kabir, Y. Mishra, G. Ledwich, Z. Y. Dong, and K. P. Wong, "Coordinated Control of Grid-Connected Photovoltaic Reactive Power and Battery Energy Storage Systems to Improve the Voltage Pro fi le of a Residential Distribution Feeder," *IEEE Trans. Ind. Informatics*, vol. 10, no. 2, pp. 967–977, 2014.

Curriculum Vitae

Maryam BAHRAMIPANAH

Born in 5th July, 1984, Tehran, Iran
Email: m.bahramipanah@gmail.com

Education

2012-2016	**Ph.D. in Electrical Engineering**, *Swiss Federal Institute of Technology (EPFL)*, Lausanne, Switzerland.
2008-2011	**Master of Science in Electrical Power Engineering,** *University of Tehran*, Tehran, Iran.
2003-2007	**Bachelor of Science in Electrical Engineering,** *K. N. Toosi University,* Tehran, Iran.

Professional Experience

2012-2016	**Research assistant**, Distributed Electrical Systems Laboratory (DESL)-EPFL, Lausanne, Switzerland.
2009-2010	**Senior researcher,** Niroo Research Institute, Tehran, Iran.
2008-2009	**Senior project engineer**, Peiman Khotoot Gostar ,Tehran, Iran.

Research Interests

- Integration of Renewable energy resources and energy storage systems into power grid
- Power systems modeling and simulation
- Distribution system optimization and control

Reviewer/supervisor

- Member of revision committee:

  IEEE Transaction on Smart Grid, on Industrial Informatics, on Sustainable Energy; Energy Power System Research (EPSR) Journal of Elsevier; Grids and Networks Journal (SEGAN) Journal of Elsevier; Energy Conversion System Conferences; Power System Computation (PSCC) Conferences.

- Master thesis supervision:

  "Control of distribution network with the integration of dispersed energy storage systems with Multi-Agent system approach", Gonzalo Egea de la Mata, Universidad Pontificia Comillas, 2014.

Publications

Journal Papers

1- M. Bahramipanah, R. Cherkaoui, M. Paolone. "A Decentralized Adaptive Model-Based Real-time Control for Active Distribution Networks Using Battery Energy Storage Systems". IEEE Transaction on Smart Grid.

2- M. Bahramipanah, D. Torregrossa, R. Cherkaoui, M. Paolone. "Enhanced Equivalent Electrical Circuit Model of Lithium-based Batteries Accounting for Charge Redistribution and Temperature Effects". IEEE Transaction on Transportation Electrification-Special Issue on Energy Storage Systems.

3- M. Bahramipanah, R. Cherkaoui, M. Paolone. "Decentralized Voltage Control of Clustered Active Distribution Network by means of Energy Storage Systems". Electric Power System Research (EPSR) journal, Elsevier, 2016.

4- K. Christakou, DC. Tomozei, M. Bahramipanah, JY. Le Boudec, M. Paolone. "Primary Voltage Control in Active Distribution Networks via Broadcast Signals: The Case of Distributed Storage". IEEE Transaction on Smart Grid, vol. 5, issue 5, p. 2314-2345, 2014.

5- D. Torregrossa, M. Bahramipanah, E. Namor, R. Cherkaoui, M. Paolone. "Improvement of Dynamic Modeling of Supercapacitor by Residual Charge Effect Estimation". IEEE Transaction on Industrial Electronics, vol. 61, issue 3, p. 1345-1354, 2014.

Conference Proceedings

1- M. Bahramipanah, D. Torregrossa, R. Cherkaoui, M. Paolone. "An Adaptive Model-Based Real-Time Voltage Control Process for Active Distribution Networks Using Battery Energy Storage Systems". Accepted in 19th Power System Computation Conference (PSCC), Genoa, 2016.

2- M. Bahramipanah, M. Nick, R. Cherkaoui and M. Paolone. "Network Clustering for Voltage Control in Active Distribution Network Including Energy Storage Systems". International Conference on Innovative Smart Grid Technologies Conference (ISGT), Washington DC, 2015.

3- M. Bahramipanah, D. Torregrossa, R. Cherkaoui, M. Paolone. "Enhanced Electrical Model of Lithium-Based Batteries Accounting the Charge Redistribution Effect". 18th Power System Computation Conference (PSCC), Wroclaw, 2014.

4- D. Torregrossa, M. Bahramipanah, R. Cherkaoui, M. Paolone. "Experimental Evidences of Redistribution Phenomenon in Supercapacitors and Consequent Improvement of Their Dynamic Model". IEEE PowerTech conference, 2013.